Modeling and Characterization of Protein Energy Landscape at Low Temperature using Spectral Hole Burning Spectroscopy

Seyed Mahdi Najafi Shooshtari

A Thesis

in

The Department of

Physics

Presented in Partial Fulfillment of the Requirements
For the Degree of
Doctor of Philosophy (Physics) at
Concordia University
Montreal, Quebec, Canada

August 2013

CONCORDIA UNIVERSITY
SCHOOL OF GRADUATE STUDIES

This is to certify that the thesis prepared

By: **Seyed Mahdi Najafi Shooshtari**

Entitled: **Modeling and Characterization of Protein Energy Landscape at Low Temperature using Spectral Hole Burning Spectroscopy**

and submitted in partial fulfillment of the requirements for the degree of

DOCTOR OF PHILOSOPHY (Physics)

complies with the regulations of the University and meets the accepted standards with respect to originality and quality.

Signed by the final examining committee:

______________________________ Chair
Dr. P. Forgione

______________________________ External Examiner
Dr. A. Szuchmacher Blum

______________________________ External to Program
Dr. J.A. Kornblatt

______________________________ Examiner
Dr. L. Kalman

______________________________ Examiner
Dr. A. Champagne

______________________________ Thesis Supervisor
Dr. V. Zazubovits

Approved by ______________________________
Chair of Department or Graduate Program Director
Dr. L. Kalman, Graduate Program Director

August 26, 2013 ______________________________
Professor J. Locke, Interim Dean, Faculty of Arts and Science

Abstract

Modeling and Characterization of Protein Energy Landscape at Low Temperature using Spectral Hole Burning Spectroscopy

Seyed Mahdi Najafi Shooshtari, PhD.

Concordia University, 2013.

Proteins play various important roles in living organisms. Understanding the way they can perform different tasks is a demanding goal for scientists. Since their structures are changing to certain extent in the process, and some flexibility is essential for proper functioning, knowledge about their static structures is not enough to understand the way they work. One of the tools for studying proteins is optical spectroscopy. However, proteins are almost incapable of light absorption in the visible range which makes them non reachable for direct measurements; therefore, indirect methods must be applied. Pigment embedded into (amorphous) solid can serve as a local reporter on static and dynamic properties of its environment. Using proteins with pigments embedded into them by Nature offers a good alternative to introducing local reporters by chemical or genetic manipulations. In our study we focus on pigment-protein complexes involved in photosynthesis, Thus, the results of this thesis can be used not only for understanding proteins in general (e.g. folding processes), but also have implications in the renewable energy field, ultimately helping us to produce more efficient solar cells.

In the course of this thesis spectral hole burning is applied for studying the properties of protein energy landscapes at cryogenic temperatures. This technique is very useful for (partially) removing the ensemble averaging by exciting specified systems selectively. We demonstrate that tunneling and not barrier hopping is most likely responsible for spectral diffusion-related phenomena (including hole burning) observed at low temperatures, that barrier heights most likely obey Gaussian and not $1/\sqrt{V}$ distribution proposed for other amorphous solids, and discuss which structural elements might participate in small conformational changes. In addition to our experimental studies, we are developing a model that more adequately reflects the multi-well protein energy landscapes than two-level system-based approaches used so far. The results are in reasonable agreement with experiment. Importantly, we demonstrate that protein systems in typical optical low-temperature experiments (hole burning or single molecule / complex spectroscopy) are far from thermodynamic equilibrium. This has to be kept in mind when interpreting the results of any optical experiments.

Acknowledgments

I would like to express my deepest appreciation to my family and especially my devoted parents who have always been encouraging me to pursue my study. Their supports in all stages of my life result in this accomplishment.

I would like to gratefully acknowledge my beloved wife, Zahra, who has provided me a calm and energetic environment to focus only on my study. I am also very grateful to have our first child, Elena, during writing my thesis.

I am more than thankful to Mr. Ali Shakeri and his wife Mrs. Shari Noviri, Mr. Zelko Bulut, and Mr. Wentworth Brooks for all kinds of helps and supports that they have done for me. I would also like to thank my friend, Nicoleta Herascu, who was helpful during my study in our lab.

Last but foremost, I would like to gratefully acknowledge my supervisor, Dr. Valter Zazubovich, not only because he has always been available and knowledgeably guided me through my research but also because he has been so supportive, nice and helpful to me that I never can compensate for his kindnesses. I do not know any words which can express my truly thankfulness feeling to him.

Table of Contents

List of Figures

List of Abbreviations

Chl a/b	Chlorophyll a/b
HB	Hole Burning
HGK	Hole Growth Kinetics
HR	Hole Recovery
LIHF	Light Induced Hole Filling
MLS	Multilevel system
NPHB	Non-Photochemical Hole Burning
PHB	Photochemical Hole Burning
PSI	Photosystem I
PSII	Photosystem II
PSB	Phonon Side Band
PSBH	Phonon Side Band Hole
RC	Reaction Center
SD	Spectral Diffusion
SDF	Site Distribution Function
SHB	Spectral Hole Burning
SMS	Single Molecule Spectroscopy
SPCS	Single Photosynthetic Complex Spectroscopy
SSA	Single Site Absorption
TLS	Two Level System
ZPH	Zero Phonon Hole
ZPL	Zero Phonon Line

Chapter 1

1. Introduction

Proteins play crucial roles in living organisms. They have a variety of functions such as carrying molecules (e.g. oxygen is carried by hemoglobin), enzymatic catalysts, molecule storage (e.g., iron can be stored in protein ferritin), acting as charge carriers, optimizing light harvesting, energy and charge transfer in photosynthesis process, etc [1]. Primary structure-wise they are simply polypeptide chains consisting of amino acids. However, they cannot be useful in their simplest form. This chain must be folded into the well-defined 3D structure, so-called tertiary structure, to be functional. This functional structure is determined by the electrostatic interactions between different parts of the protein and between the protein and its surrounding (water, lipid membrane, etc.). It may seem that knowing the static tertiary structure (which is usually found by X-ray diffraction or nuclear magnetic resonance (NMR) spectroscopy [2]) one can fully explain protein functionality. This is only partially true. Proteins change their structure in different ways to perform specific action. For instance, conformational changes are required for entering and exiting of small ligand in myoglobin [3]. Even if major conformational changes (such as in myoglobin) are not required for successful functioning, proteins still retain certain degree of flexibility or, in other words, of disorder. Thus, proteins are not static and consequently their dynamics often is important to understand their function [4]. For that reason, we are interested in studying the dynamics of the proteins.

A related issue is the shape of the protein energy landscape. The term refers to the set of local energy minima (conformational sub-states) and the barriers between them. The detailed knowledge of the protein energy landscapes is important for understanding the folding process. It is well-known (see Levinthal paradox) that if proteins were optimizing their energy just by randomly sampling all available conformational sub-states, folding of even very simple proteins, with only 100 aminoacids, would take longer than the age of the Universe. The fact that in reality proteins are properly folding within reasonable time indicates that there must be some hierarchy of processes during folding, and that, correspondingly, there must be some hierarchy of barriers on the protein energy landscape. This, however, is just a qualitative statement, and fully understanding protein energy landscapes and folding requires more quantitative knowledge.

Protein dynamics and energy landscapes can be studied by multiple methods, including various methods of optical spectroscopy. As proteins in their natural form are amorphous (glass-like), many theoretical models and experimental approaches developed for glasses are applied to proteins as well [5]. Although the existence of several conformational sub-states due to protein complexity and flexibility makes them similar to glasses, their well-ordered overall structure makes them distinct from glasses as well. Two of the most striking similarities between glasses and proteins concern relaxation mechanisms and chemical reactions which evolve non-exponentially with time (non-Arrhenius temperature dependencies[1]). It means that the energy landscapes in both

---

[1] In case of a simple system the relaxation time is an exponential function of time, so called Arrhenius relation [6].

systems are qualitatively similar to each other in that they exhibit broad distributions of barrier parameters. The term “energy landscape” refers to the potential energy of proteins or glasses with respect to the relative coordinates of their atoms. Finding the correct energy landscape is a demanding goal, but it can explain all conformational dynamics of proteins from folding to local fluctuations on atomic scale [5].

The fact that proteins do not absorb or emit in the visible range makes them challenging to study directly by optical spectroscopy methods. Therefore, an optically active material (pigment or “guest”) can be embedded in the protein, and then the changes in spectral features of that pigment would reflect the changes in the environment (protein, or “host”). In other words, the pigment serves as a local reporter of its environment. The pigment can be embedded into protein through different complicated artificial methods (e.g. biochemical or genetic engineering procedures). However, it remains questionable to what extent these procedures alter the native structure of the protein, and if subsequent experiments report on native, non-modified structure. Another choice would be using pigment-protein complexes existing in nature. In this sense, the photosynthetic complexes are the best candidates for studying the intact proteins by optical methods. The guest molecules (pigments) are already built into the host (protein) by nature in photosynthetic complexes. In addition, these pigments are embedded into a large diversity of local protein environments which can be selected spectrally [7].

The pigment-protein complexes used in this study are extracted from Photosystem II (PSII) either from pea or spinach. Photosystem II is one of the two main protein complexes (the other one is Photosystem I, PSI) employed by plants, algae and cyanobacteria for primary charge separation, producing oxygen as a by-product. The first steps of the photosynthesis process which is vital for life on Earth are performed by these two complexes. Understanding photosynthesis promises a solution to the renewable energy problem. Current knowledge about the primary processes of photosynthesis (light-harvesting, energy transfer and charge separation) also indicates the importance of the effects of protein structure and dynamics. Thus, this research is motivated by our desire to not only better understand protein energy landscapes in general, but to better understand photosynthesis as well.

Studying a protein by means of optical spectroscopic methods requires removing the inhomogeneous broadening which buries the detailed information on the dynamics of the system. There are two types of spectroscopic techniques for this purpose: frequency domain ones (e.g. fluorescence line narrowing, luminescence excitation with spectrally selective recording, spectral hole burning and single molecule or single complex spectroscopy, SPCS.) and time domain ones (e.g. photon echoes, four wave mixing, and so on) [8]. Spectral Hole Burning (SHB) is a frequency domain technique applicable to both fluorescent and non-fluorescent molecules (in the latter case one just has to work in transmission). The resolution of optical techniques is enhanced at low temperature. While it is true that at cryogenic temperature there is no biological activity, one still can extract lots of information which is masked at higher temperatures. It is also believed that it is possible to properly extrapolate the information obtained for proteins at low temperature to physiological temperature [6].

Hole burning spectroscopy is based on exposing the sample to a very narrow, well defined frequency using a stabilized laser (in terms of output power and wavelength) mostly at cryogenic temperatures. The molecules which can absorb at the burn wavelength experience a change in either their structures (photochemical HB) or the structure of the immediate environment (photophysical, or non-photochemical HB, NPHB). This means that those molecules cannot absorb at the burn wavelength anymore. The subtraction of the spectrum before burning (pre-burn spectrum) from the one after burning (post-burn spectrum) results in a hole spectrum. The hole width, depth, shape, area and evolution upon burning and recovery contain valuable information about the environment of the pigment (which in our case is protein). This information may include fluorescence life time, excitation energy transfer times, electron-phonon coupling, etc.

One goal of this thesis is to further develop the methods of spectral hole burning and to introduce new features into both experiments and data analysis for pigment-protein complexes at low temperatures. These refinements of the methodology allow us to verify or reject certain widespread assumptions currently used in our field and derive new information.

Proteins involved in the photosynthesis process will be reviewed in Chapter 2. The interaction of light and chromophores embedded in solids is briefly explained in Chapter 3, followed by the theory of SHB applicable for protein dynamics study. In Chapter 4, we present experimental results obtained for several photosynthetic antenna complexes, CP29, CP43 and LHCII, with CP43 being the focus of the most detailed study, involving not only hole burning, but also hole recovery at fixed temperature and thermocycling. Implications of these results will be discussed.

Chapter 5 is devoted to introducing a novel approach to modeling optical manifestations of protein dynamics, including both SHB and single molecule spectroscopy. The key feature that distinguishes our approach from those of other groups is that we recognize that most of the phenomena observed in optical experiments on amorphous solids are light-induced, while others interpret their data as if they were just observing phenomena occurring anyway, i.e., being thermally induced. The details of our program for simulation of SHB are explained and the ability of this program to model single molecule spectroscopy observations is discussed. The results of our model are compared with our experimental results for different modes of SHB. The questions about spectral memory and equilibrium are addressed, followed by discussion about discrepancies between simulation and experiment. This thesis will be concluded by reviewing outstanding points and some suggestions for further research on protein dynamics in Chapter 6.

Chapter 2

2. Photosynthetic Protein Complexes

The photosynthesis process is vital for the life on Earth. There are several steps involved in converting the energy of light to chemical energy and oxidizing the water molecule to produce oxygen during this process. Proteins are necessary for photosynthesis, although many details of their roles have not been fully revealed yet. A short review of this process is given in this chapter, followed by an overview of a particular photosynthesis protein complexes.

2.1. Photosynthesis

Oxygenic photosynthesis[1] is a process in which carbon dioxide and water are combined to produce carbohydrates and oxygen (which are essential for life) by using sunlight energy. Carbohydrate synthesis can be summarized by the following equation:

$$\begin{array}{ccccccccc} 6H_2O & + & 6CO_2 & + & Photons & \rightarrow & C_6H_{12}O_6 & + & 6O_2 \quad \text{or} \\ Water & + & Carbon\,Dioxide & + & Photons & \rightarrow & Glucose & + & Oxygen \end{array} \tag{2.1}$$

There are two main stages, namely, light reactions and dark reactions, in the carbon dioxide reduction. In the former step, a photon is absorbed by a pigment (e.g. a chlorophyll or a carotenoid in a light-harvesting complex) and its energy is transferred to the photochemical reaction center (RC). Light harvesting is performed mostly by Chlorophyll *a* and *b* in green plants, algae and cyanobacteria, and mostly by Bacteriochlorophylls in organisms involved in non-oxygenic photosynthesis. There are

---

[1] Anoxygenic photosynthesis occurring in purple bacteria is out of the scope of this study.

two main photosynthetic protein complexes in plants, algae and cyanobacteria, namely Photosystem II (PSII) and Photosystem I (PSI). The so-called Z-scheme involving these complexes is shown in Fig. 2.1.

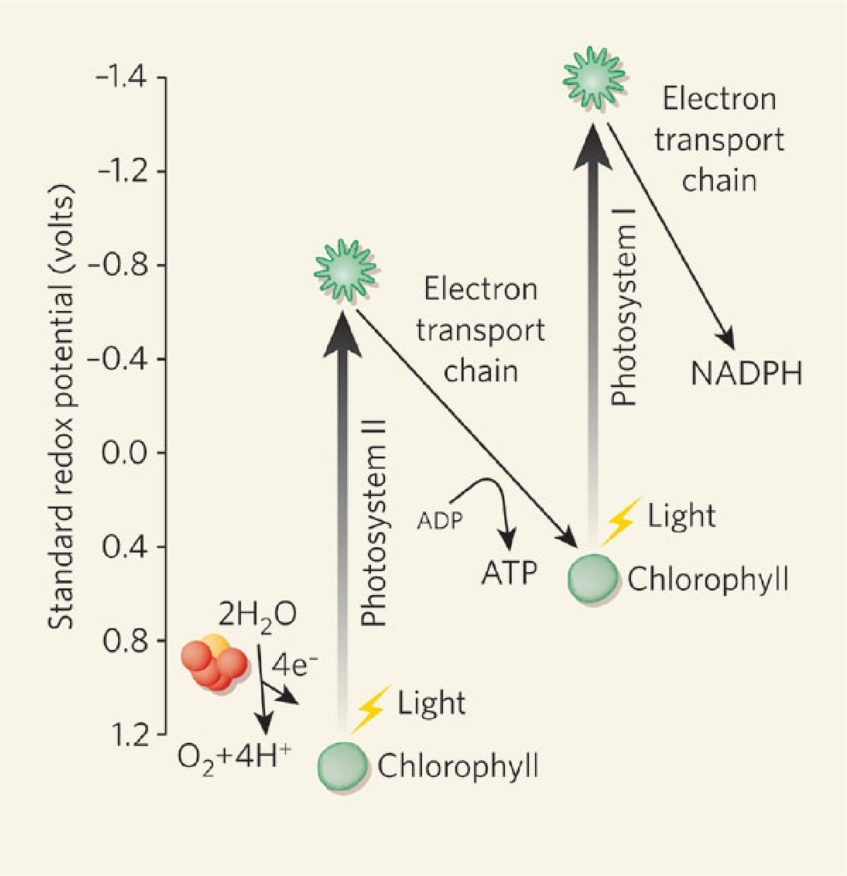

Figure 2.1. A schematic of the photosynthesis process leading to storing light energy as chemical energy, with oxygen as a by-product. This chain-like process starts by light absorption (via mostly chlorophylls) in PSII, and leads to splitting water molecules (four red and one orange spheres indicate manganese Oxygen-Evolving Cluster) and making oxygen molecule. The electrons are transported to PSI which ultimately converts $NADP^+$ to NADPH, the necessary material for producing sugars. Adapted with permission from [9]. Copyright © 2007, Rights Managed by Nature Publishing Group

Besides PSI and PSII other elements of the photosynthesis process are shown in Fig. 2.1. This apparatus works as an electrochemical solar cell. PSII uses light energy to produce an electrochemical potential of +1.1 volts (the first step in this process), enough to split water. Two electrons are taken from each of two water molecules, which results in a molecule of O_2 (following absorbing of four photons) necessary for breathing, as well as protons. The four electrons will be transported by charge carriers (quinones) to cytochrome b6f to PSI where they are used to reduce $2NADP^+$ to 2NADPH with the help of another four photons. During the electron transportation between PSII and PSI a proton gradient across the thylakoid membrane is further enhanced, which is then used in synthesis of the energy-storage molecule adenosine triphosphate (ATP). The end product of photosynthesis is carbon-based sugar from carbon dioxide [9].

2.2. Photosynthesis Efficiency and Proteins

The internal quantum yield of excitation energy conversion in photosynthesis apparatus is close to one. This means that one photon being absorbed anywhere in the antenna almost always results in charge separation in the RC (Fig. 2.2. (a)). There is no man-made perfect photochemical machine and they all have quantum efficiencies much lower than one (Fig. 2.2. (b)) [10]. Proteins apparently organize the processes of energy and charge transfer for maximal effectiveness. Hence, one of the results of understanding the roles that proteins play in facilitating the photosynthesis could be the improvement of solar cells.

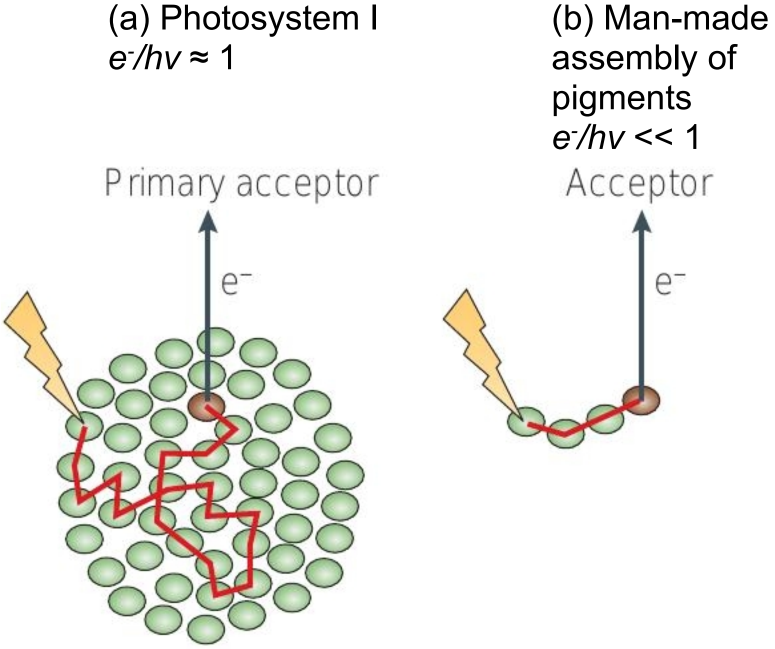

Figure 2.2. Energy transfer and quantum efficiency in (a) photosynthetic antenna where the excitation energy may be transferred between the pigments and into the reaction center, with quantum efficiency close to one; (b) man-made devices which so far have quantum efficiency significantly less than one. Adapted with permission from [10]. Copyright © 2004, Rights Managed by Nature Publishing Group

In the following, the roles of each protein in the photosynthesis process are briefly discussed after a short introduction into the most abundant pigments (Chlorophyll *a* and *b*).

2.3. Chlorophylls *a* and *b*

Chlorophyll *a* (Chl *a*) is the most common pigment involved in harvesting light energy that is present in all oxygenic photosynthesis systems. The structure of Chl *a* is shown in Fig. 2.3. It consists of a porphyrin ring (with a magnesium at its center) attached to a long hydrophobic tail. It is capable of light absorption in a wide wavelength range with two main bands peaking at 430 nm and 662 nm (in solution at room temperature). It should be mentioned that there is another widespread type of chlorophyll - so-called chlorophyll *b* (Chl *b*) which complements the absorption spectrum of chlorophyll *a* by having two maxima in absorption spectrum at 453 nm and 642 nm. The structure of Chl *b*, which is slightly different from Chl *a* (the H_3C, highlighted in blue, is substituted by CHO, highlighted in green) is given in Fig. 2.3.

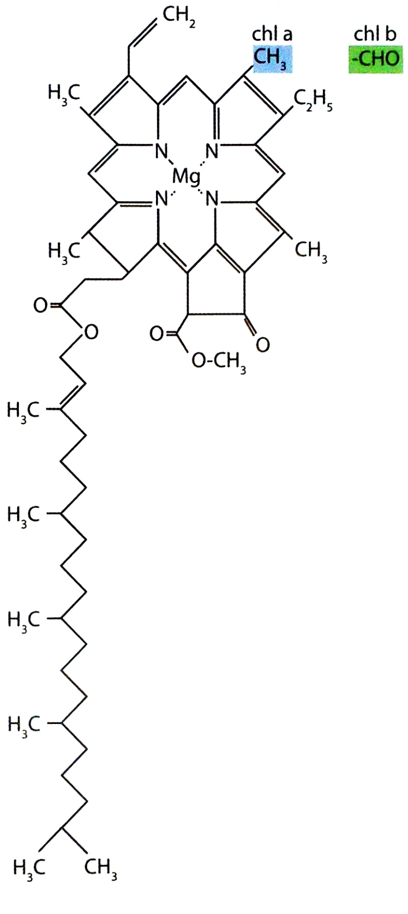

Chlorophyll

Figure 2.3. The molecular structure of Chl *a* and Chl *b*. The structural difference between these two chlorophylls is highlighted. Adapted with permission from [11], Copyright © 2009, This material is reproduced with permission of John Wiley & Sons, Inc.

The absorption spectra of these two chlorophylls are shown in Fig. 2.4. It should be noted that depending on the solvent their spectra are somewhat different. For the sake of brevity, this solvent dependence is shown only for Chl *a*.

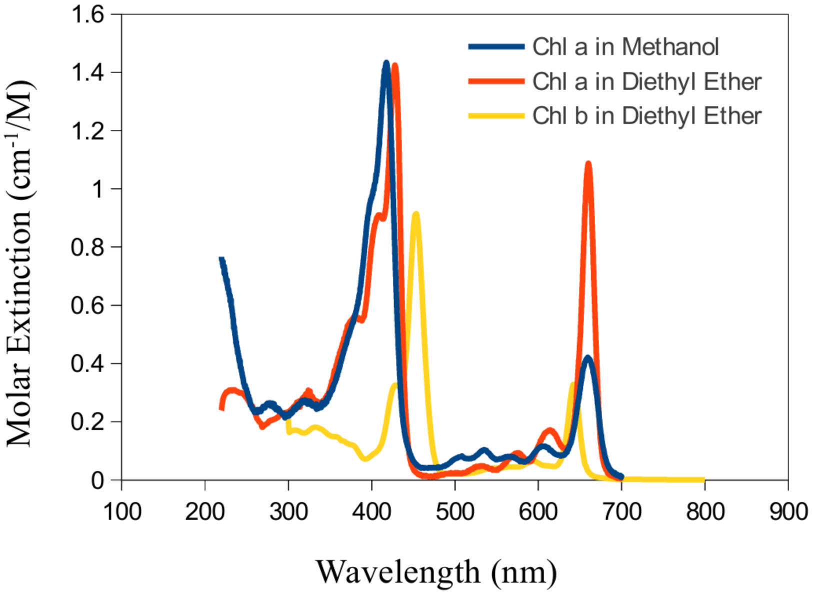

Figure 2.4. The absorption spectra of chlorophyll *a* and *b*. The results for Chl *a* are shown in methanol and diethyl ether, the spectrum of Chl *b* is drawn only for diethyl ether [12].

2.4. Photosystem II (PSII)

PSII[1] is the first protein complex engaged in oxygenic photosynthesis process by producing the electrons that are further fed to PSI. PSII is also responsible for water splitting and oxygen production. This large protein complex can be found in organisms from cyanobacteria to higher plants, in the latter case – inside the thylakoid membranes.

---

[1] Since it is, historically, found after PSI, it is called PS II; otherwise, this name does not reflect the order in which charge transfer occurs.

Its core is dimeric, with C_2 symmetry, and each monomer includes CP43 and CP47 antenna proteins, and the reaction center subunits (D1 and D2) [13], [14]. The core is surrounded by peripheral antenna complexes CP24, CP26, CP29, and LHCII[1]. The overall structure of PSII is depicted in Fig. 2.5 [15].

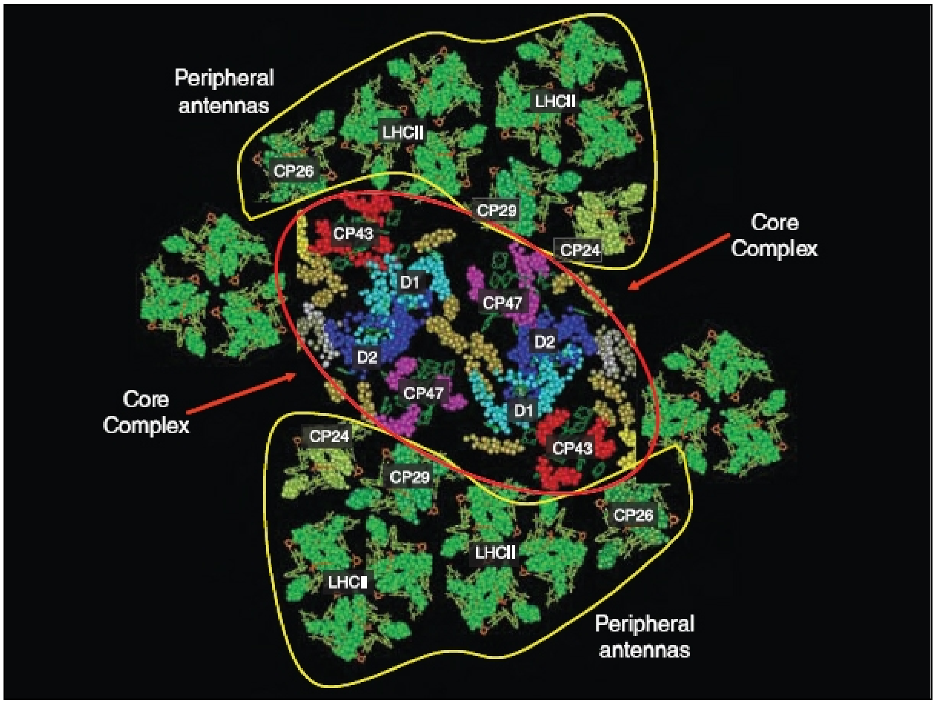

Figure 2.5. The top view of PSII and different embedded proteins in it like CP43, CP47, CP24, CP26, CP29, LHCII [15]. Its C2 symmetry is obvious in this picture.

The structures of peripheral and core complexes are discussed in the following section.

---

[1] CP and LHC stand for Chlorophyll Protein and Light-Harvesting Complex, respectively. The number after CP refers to the corresponding protein molecular mass in kDa which is usually measured by electrophoresis.

2.4.1. Core Protein Complexes

There are four major protein subunits in the core monomer of PSII which are D1, D2, CP43, CP47. The positions of CP43 and CP47 and their Chls with respect to RC are depicted in Fig. 2.6 [15]. The D1 and D2 proteins comprise the reaction center of PSII. They are responsible for binding all of the electron transfer chain components occurring in PSII, namely four chlorophylls, two pheophytines, a non-heme iron, quinones, as well as the oxygen-evolving cluster. Two additional Chl *a* molecules, Chl_Z, are located at the periphery of the RC and do not participate in charge separation. The other two proteins act as proximal antenna of PSII. The location of CP43 is at the D1 side of PSII whereas CP47 is located at the D2 side as shown in Fig. 2.6. CP43 contains 13 Chl *a* and 2-3 β-carotene molecules while CP47 binds 16 Chl *a* and 5 β-carotene molecules [16]. It is well accepted that due to the arrangement of these pigments enclosing the RC, they facilitate transferring of the excitation energy to the RC of PSII, containing the primary electron donor P680 [8]. For that reason they are named intrinsic light-harvesting proteins which make them distinct from other light-harvesting complexes such as LHCII [14].

2.4.2. Peripheral Protein Complexes

There are four protein complexes in PSII located farther from the RC than core protein complexes, namely CP24, CP26, CP29, and LHCII. LHCII, which is believed to be trimeric in nature, is the most widespread light-harvesting complex. The other proteins are minor Chl *a/b* binding complexes (CP24, CP26, and CP29).

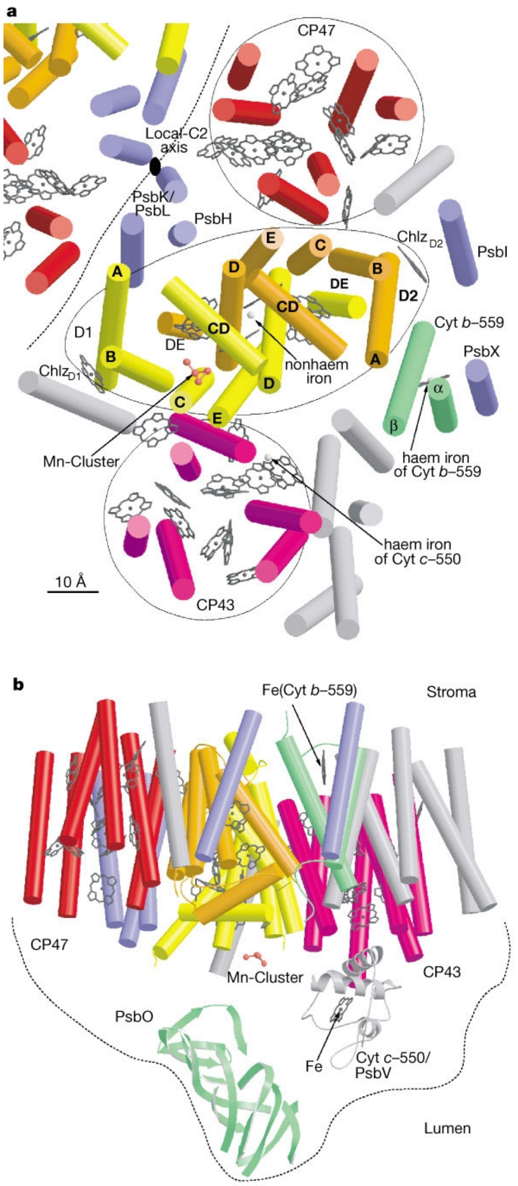

Figure 2.6. a) The structure of PSII and the arrangement of its different elements including CP43 and CP47 and their Chls with respect to RC of PSII (only one monomer of the dimer is shown clearly from the luminal side view which is perpendicular to the membrane plane). Black wires indicates Chl *a* head groups and hemes. D1 and D2 are shown in an ellipse. There are seven unassigned alpha-helices which are drawn in grey. Arrows are pointing four prominent landmarks (the Mn cluster and three irons). b) Side view of PSII monomer where PsbO (33K protein) is indicated as a beta-sheet structure (green), and Cyt c-550 as a helical model (grey). Adapted with permission from [17]. Copyright © 2008, American Chemical Society.

These three relatively light protein complexes bind around 15% of the Chl in PSII (~5% each). They are located between the LHCII trimers and the PSII core [18], [19] with CP24 slightly closer to the LHCII than CP26 and CP29 [20], [21]. CP24 binds 10 Chl a and 2 carotenoids [22]. 6-7 Chl a and 2 Chl b are bound together by CP26 [23]. It has been recently revealed that CP29 hold 8 Chl *a,* 4 Chl *b,* 1 supposedly mixed site occupied by both Chls *a* and *b* and two–three carotenoid molecule [24]. The functions of these proteins are not fully understood, although it is believed that they have two general roles a) holding the network of chlorophylls together in a manner that facilitates energy transfer towards the RC and b) quenching excessive excitation energy to protect the RC via dissipating energy as heat (so called non-photochemical quenching) [25], [26].

LHCII is the major complex binding Chl *a* and *b* in the thylakoid membrane, containing half of the all Chls in PSI and PSII[1] [27]. LHCII is naturally a trimer, although monomeric LHCII can be prepared, and its properties have been compared to the LHCII trimer to better understand its function. There are 8 Chl *a* and 6 Chl *b* within each monomer (with the molecular mass of ~25 kDa) of this protein. Besides its important role in solar light harvesting, it also regulates the energy distribution between PSI and PSII, as some fraction of these complexes can migrate between PSII and PSI.

---

[1] It should be noted that there are two types of LHCII as shown in Fig. 2.5 which are identical in terms of structure but different in function. One is closer to RC considered bound (known as inner LHCII or non-mobile) and the other one which is more peripheral called outer (or mobile) complex. The latter one can migrate between PSII and PSI regulating the excitation energy distribution between them.

2.5. Photosystem I (PSI)

The further stages of converting the solar energy to chemical energy occur in PSI. The reaction center of this pigment-protein complex is structurally similar to the reaction center of PSII. However, the wavelengths of the primary electron donors are different. PSI is capable of absorbing light with the wavelengths longer than 690 nm and its primary donor P700 has the maximum absorption at 700 nm, whereas PSII's primary donor absorbs near 680 nm. The electrons released by the RC of the PSII due to photoexcitation can be carried to PSI where they are used again to convert $NADP^+$ to NADPH. This can then participate in production of glucose in the Calvin cycle.

In this work, we investigated CP43 and CP29 complexes of PSII from spinach and monomeric and trimeric LHCII complexes (transiently associated with PSI) from pea.

Chapter 3

3. Theory of Spectral Hole Burning

In this chapter all theory regarding spectral hole burning which is used in this thesis is discussed, including different types of this method and the process of determining the protein energy landscape parameters in both the ground and excited states of pigment-protein systems. Before concentrating on spectral hole burning, there will be a short review of the interaction of light with chromophores in solids, followed by its application in our hole burning technique.

3.1. Light and Solid Interaction

The theories of spectral hole burning rely on the theories describing so-called impurity centers in solids [27]. This is a special and distinct case with respect to situations where the bulk (host) material itself has absorption bands in the visible region, such as semiconductors [28]. The interaction between light and matter is the basis of every spectroscopic technique. As the mass of the proton is almost 1800 times larger than the electron mass, it is reasonable to claim that electronic and nuclei states can be considered separately (so-called Born-Oppenheimer approximation). Then, there are electronic and vibrational quantum states; if the vibrational states are delocalized, the quanta of these states are called *phonons*. The total wavefunction of a system is a product of the electronic wavefunction $\psi(r,R)$ and the vibrational wavefunction $\chi(R)$ depending on all possible vibrational and rotational movements of nuclei.

$$\Psi(r,R)=\psi(r,R)\chi(R) \tag{3.1}$$

Here r and R are the positions of the electrons and the nuclei respectively [29]. The combination of electronic and vibrational states is usually called a *vibronic* state.

In the simplest case of a diatomic molecule, the nuclear Hamiltonian is described by the harmonic oscillator. The eigenvalues of such a Hamiltonian are $E_n = (n+1/2)\ h\upsilon$. Here $h\upsilon$ is the vibrational energy and $n = 0, 1, 2, \ldots$. It can be assumed for simplicity that the molecule has only a ground $\Psi_{a,n} = \psi_a(r, R)\chi_n(R)$ and an excited $\Psi_{b,m} = \psi_b(r, R)\chi_m(R)$ electronic state. Both vibrational and electronic wavefunctions can be changed during the electronic transition. The probability of a transition between these two states can be calculated by finding the matrix element, which requires writing the dipole operator (P) for the electrons (P_e) and nuclei (P_{nuc}) separately:

$$\boldsymbol{P} = \boldsymbol{P}_{el} + \boldsymbol{P}_{nuc} = \sum_i e\,\boldsymbol{r}_i + \sum_j z_j \boldsymbol{R}_j \tag{3.2}$$

Here $\boldsymbol{r}_i$, $\boldsymbol{R}_j$, e, z_j are the position of electron i, location of nucleus j, electron charge, and charge of nucleus, respectively. In the simplest case of one electron and one nucleus, the transition dipole is [29]:

$$\begin{aligned}
\boldsymbol{\mu}_{ba,mn} \quad = \quad & \langle \psi_b(\boldsymbol{r},\boldsymbol{R})\chi_m(\boldsymbol{R}) | \boldsymbol{P}_{el} | \psi_a(\boldsymbol{r},\boldsymbol{R})\chi_n(\boldsymbol{R}) \rangle \\
& + \langle \psi_b(\boldsymbol{r},\boldsymbol{R})\chi_m(\boldsymbol{R}) | \boldsymbol{P}_{nuc} | \psi_a(\boldsymbol{r},\boldsymbol{R})\chi_n(\boldsymbol{R}) \rangle \\
= \quad & e\int \chi_m^*(\boldsymbol{R})\chi_n(\boldsymbol{R})\ d\boldsymbol{R}\ \int \psi_b^*(\boldsymbol{r},\boldsymbol{R})\psi_a(\boldsymbol{r},\boldsymbol{R})\boldsymbol{r}\ d\boldsymbol{r} \\
& + z\int \chi_m^*(\boldsymbol{R})\chi_n(\boldsymbol{R})\ \boldsymbol{R}\ d\boldsymbol{R}\ \int \psi_b^*(\boldsymbol{r},\boldsymbol{R})\psi_a(\boldsymbol{r},\boldsymbol{R})\ d\boldsymbol{r}
\end{aligned} \tag{3.3}$$

It should be noted that $\int \psi_b^*(\boldsymbol{r},\boldsymbol{R})\psi_a(\boldsymbol{r},\boldsymbol{R})\ d\boldsymbol{r}$ is simply $\langle \psi_b | \psi_a \rangle$ for a specific $\boldsymbol{R}$, which is zero if $a \neq b$. Hence,

$$\begin{aligned}\boldsymbol{\mu}_{ba,mn} &= \langle \psi_b(\boldsymbol{r},\boldsymbol{R})\chi_m(\boldsymbol{R})|\boldsymbol{P}_{el}|\psi_a(\boldsymbol{r},\boldsymbol{R})\chi_n(\boldsymbol{R})\rangle \\ &= e\int \chi_m^*(\boldsymbol{R})\chi_n(\boldsymbol{R})\ d\boldsymbol{R}\ \int \psi_b^*(\boldsymbol{r},\boldsymbol{R})\psi_a(\boldsymbol{r},\boldsymbol{R})\boldsymbol{r}\ d\boldsymbol{r}\end{aligned} \tag{3.4}$$

Since the electronic wavefunctions are functions of nuclear coordinates, the double integral in eq. 3.4 cannot be written as a product of the form $e\langle\chi_m(\boldsymbol{R})|\chi_n(\boldsymbol{R})\rangle\langle\psi_b(\boldsymbol{r},\boldsymbol{R})|\psi_a(\boldsymbol{r},\boldsymbol{R})\rangle$. However it can be written as $\langle\chi_m(\boldsymbol{R})|\chi_n(\boldsymbol{R})\boldsymbol{U}_{ba}(\boldsymbol{R})\rangle$ where $\boldsymbol{U}_{ba}(R)=\langle\psi_b(\boldsymbol{r},\boldsymbol{R})|\boldsymbol{P}_{el}|\psi_a(\boldsymbol{r},\boldsymbol{R})\rangle$ is an electronic transition dipole. In most of the cases $\boldsymbol{U}_{ba}$ ***(R)*** does not change over the range of R where the amplitudes of both vibrational wavefunctions (χ_m and χ_n) is considerably high. Thus, the transition dipole can be expressed as

$$\boldsymbol{\mu}_{ba,mn}=\langle\chi_m(\boldsymbol{R})|\chi_n(\boldsymbol{R})\overline{\boldsymbol{U}_{ba}}(\boldsymbol{R})\rangle \tag{3.5}$$

where $\overline{\boldsymbol{U}_{ba}}(\boldsymbol{R})$ emphasizes that the averaged value of the nuclear coordinates is considered during the course of the transition for calculating the electronic transition dipole. Therefore, in a good approximation, the transition dipole $\boldsymbol{\mu}_{ba,mn}$ depends only on a nuclear overlap integral and the average of an electronic transition dipole over the nuclear coordinates. This is known as the *Franck-Condon approximation*.

According to the Franck-Condon approximation, only those transitions are allowed whose nuclear overlap integral ($\langle\chi_n(R)|\chi_m(R)\rangle$)[1] is not zero (Fig. 3.1). There are two

---

[1] This condition imposed by the Franck-Condon approximation which states that among interaction between light and material both electronic and vibrational wavefunctions are changed but the transitions with the same vibrational wavefunction (or maximum overlap) are more likely. The square of overlap function (the Franck-Condon factor) is related to the dipole moment and the transition probability.

possible scenarios for transition between the ground and excited electronic states. In the first case, the potential minima for both the excited and the ground states correspond to approximately the same value of generalized coordinate q (q_g = q_e,; in a diatomic molecule these are just the bond lengths in the ground and the excited states respectively). According to the orthogonality condition for different wavefunctions of vibrational levels ($m \neq n$) , $|\langle\chi_n(R)|\chi_m(R)\rangle|^2$ is 1 for $m = n$ and 0 for $m \neq n$. Hence, as long as vibrational frequencies are the same in the excited and ground electronic states, all allowed transitions ($\Psi_{a,n} \rightarrow \Psi_{b,m}$) have the same energy, and consequently, the absorption (or fluorescence) consists of only one line at the energy (or frequency) corresponding to $|E_a - E_b|$ Fig. 3.1. (a). However, this is not the most probable case, because electron distributions are usually not completely similar in the ground and excited states. Therefore, equilibrium positions of the atoms are different in the ground and excited electronic states. This leads to a nonzero value for the overlap integral for $m \neq n$, and less than unit overlap for $m = n$. In other words, there will be absorption at frequencies different from that of the 0-0 transition. This is shown in Fig. 3.1. (b) by shifting the position of minimum energy in the excited state with respect to the ground state. This shift is related to the interaction between electrons and either molecule's vibrations or delocalized lattice vibrations, phonons. This interaction is called electron-phonon coupling [30]–[32].

It should be mentioned that besides changing the position of the minimum of the excited state, its curvature may be changed as well (resulting in different frequencies,

$\hbar\Omega$ in the ground state and $\hbar\Omega'$ in the excited state). The latter effect causes more broadening with respect to the ideal case (Fig. 3.1. (a)).

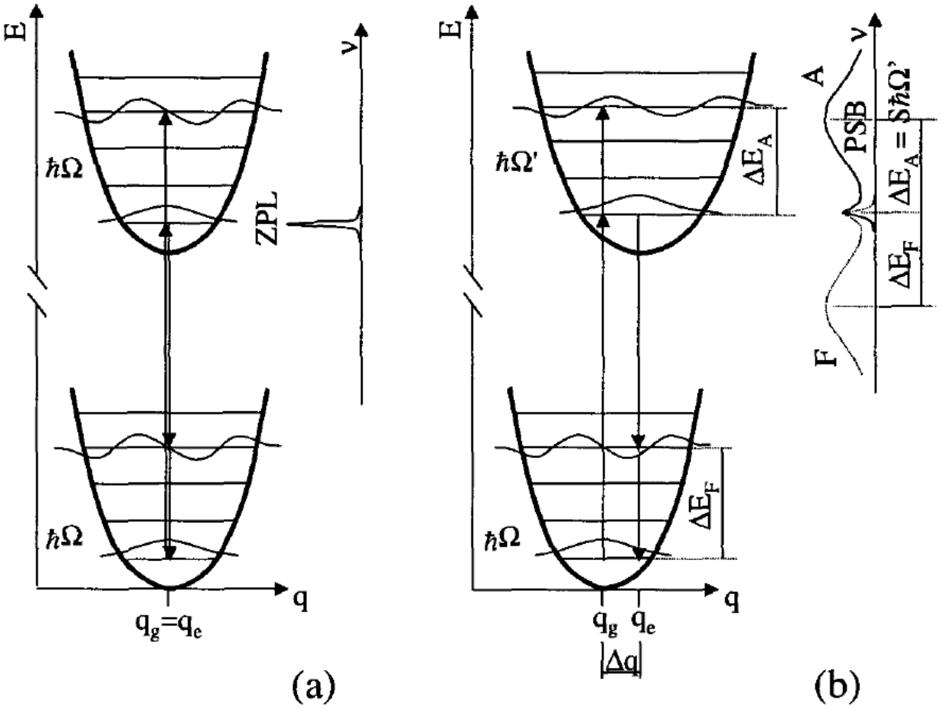

Figure 3.1. The vibrational potential energy in the ground and the excited states with the (a) same bond length and (b) different length. Possible transitions in each case are shown by arrows. The schematic of absorption (shown as A) and fluorescence (shown as F) spectra are depicted in the right hand sides of each of the figure. Adapted with permission from [8], Copyright © 2004 by World Scientific Publishing Co. Pte. Ltd.

The most populated level at low temperatures is the lowest vibrational state; therefore, the transition from this state has maximal intensity. The transition to the lowest vibrational level in the excited state corresponds to the zero-phonon line (ZPL, 0-0 transition) with a shape of a Lorentzian function [33]. However, a shoulder, the so-called phonon side band (PSB), accompanies the ZPL since an electronic transition involves the change of equilibrium value of generalized coordinates. As it is readily seen from Fig.

3.1, the PSB is at higher energy with respect to the ZPL in absorption spectrum but the situation is reversed in the fluorescence spectrum. Both the ZPL and the PSB are temperature dependent (due to the population dependency of each level on the temperature), and their dependency is shown in the Fig. 3.2. By increasing the temperature, one allows 1-1, 2-2, etc. transitions contributing to the ZPL, but also increases the probabilities of transitions contributing to the phonon sideband (PSB). At temperatures larger than approximately 50 K, the PSB would be the most dominant feature of absorption spectrum. Ω_m is the energy difference between the maxima of the PSB and the ZPL, which is around 15-20 cm^{-1} in proteins at low temperatures [8]. The shape of the PSB reflects the phonon distribution. Continuing with the analogy between the generalized coordinate and the bond length in simple diatomic molecules, it is convenient to introduce a coupling factor which is called the Huang-Rhys factor [29]:

$$S=\frac{1}{2}\Delta^2 \tag{3.6}$$

here Δ is a dimensionless factor proportional to the bond length as

$$\Delta=2\pi\sqrt{\left(m_r\frac{\nu}{h}\right)}\left(b_e-b_g\right) \tag{3.7}$$

where $(b_e - b_g)$ is the bond length difference between the ground and excited states, m_r is the reduced mass of vibrating atoms and v is the frequency of bond vibration (its change is usually negligible through transition between two states) and h is Plank's constant [29]. S can be interpreted as average number of phonons excited per electronic transition. The ZPL transition probability is related to this factor through the equation below[1]:

$$|\langle \chi_0 | \chi_0 \rangle|^2 = \exp(-S) \tag{3.8}$$

Coupling factors of the order of 0.1 to 0.5 correspond to weak coupling, while those greater than 1 are considered strong coupling. Thus for strong electron-phonon coupling, the PSB is dominant, while for weak coupling, the ZPL is more important. It is convenient to use a more directly measurable parameter depending on the intensities of the ZPL and the PSB which is known as the Debye-Waller factor α_{DW} :

$$\alpha_{DW} = \frac{I_{ZPL}}{I_{ZPL} + I_{PSB}} \tag{3.9}$$

here I_{ZPL} and I_{PSB} are the integrated intensities of the ZPL and the PSB respectively. Thus, small α_{DW} refers to huge I_{PSB} or strong electron-phonon coupling (large S), and large α_{DW} correspond to weak coupling (small S). The temperature dependence of α_{DW} can be written as [34]:

$$\alpha_{DW} = \exp\left[-S \times \coth\left(\frac{\Omega_m}{2k_B T}\right)\right] \tag{3.10}$$

here T is the absolute temperature, k_B is the Boltzmann constant, and Ω_m is the energy difference between the peaks of the ZPL and the PSB. It is clear that when T goes to zero, $\alpha_{DW} = \exp(-S)$ which is simply the square of 0-0 overlap integral.

---

[1] General expression for transition between level *m* and *0* is $|\langle \chi_m | \chi_0 \rangle|^2 = \frac{S^m \exp(-S)}{m!}$.[29]

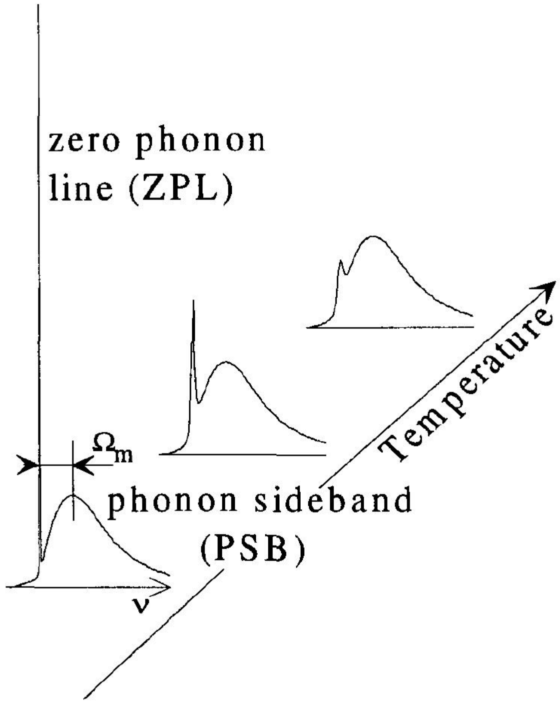

Figure 3.2. The intensities of the PSB and the ZPL are highly temperature-dependent and at higher temperature the predominant feature of the spectrum is PSB as opposed to the cryogenic temperature. Adapted with permission from [8], Copyright © 2004 by World Scientific Publishing Co. Pte. Ltd.

3.2. Homogeneous and Inhomogeneous Broadening

The minimal possible linewidth in single-molecule absorption spectrum is determined by energy-time uncertainty ($\Delta E . \Delta t \geqslant \hbar$) where Δt is excited state lifetime. This is called *homogeneous broadening*. To show the relationship between the linewidth for the ensemble of molecules, and the reasons for its broadening, consider N identical molecules, with each of them having two levels (the ground, $|1\rangle$, and the excited state, $|2\rangle$) in vacuum. As shown in Fig. 3.3. (a) in vacuum all identical molecules have the same line width as well as frequency. Therefore, in the absence of any interactions between molecules, the absorption line shape at low T is a very narrow Lorentzian line. The so-called natural line width (γ_{nat}) is determined by the excited state lifetime, τ_1

$$\gamma_{nat}(cm^{-1}) = \frac{1}{2c\pi\tau_1} \tag{3.11}$$

here c (cm/s) is the speed of light, and the width is defined as full width at half maximum, FWHM. In gaseous phase that line may still be broadened by Doppler effect or collision broadening.

However, if these molecules are embedded in some environment, a) the transitions would be shifted to another frequency (υ_1), Fig. 3.3 (b), as a consequence of interactions with their surroundings[1] and b) identical molecules in an identical environment exhibit the same transition frequencies but the line widths would be broader than in the vacuum (again, under assumption that the number of pigments is so small that they are not interacting with each other). The *homogeneous linewidth* (Γ_{hom}) is determined by:

$$\Gamma_{hom} = \frac{1}{\pi\tau_2} \tag{3.12}$$

where τ_2 is the coherence lifetime in the excited state, so-called total dephasing time.

Two contributions are affecting τ_2: the time that it takes population of molecules in the excited state to relax down to the ground state, τ_1 (excited state lifetime), and τ_2^*, pure dephasing time. τ_1 is equal to the observed fluorescence lifetime, including both radiative and non-radiative relaxations for the fluorescent molecules.

---

[1] This shift, solvent shift, can be understood by considering that the transition between two levels is related to the dipole moment which is changing when molecule is in a different medium.

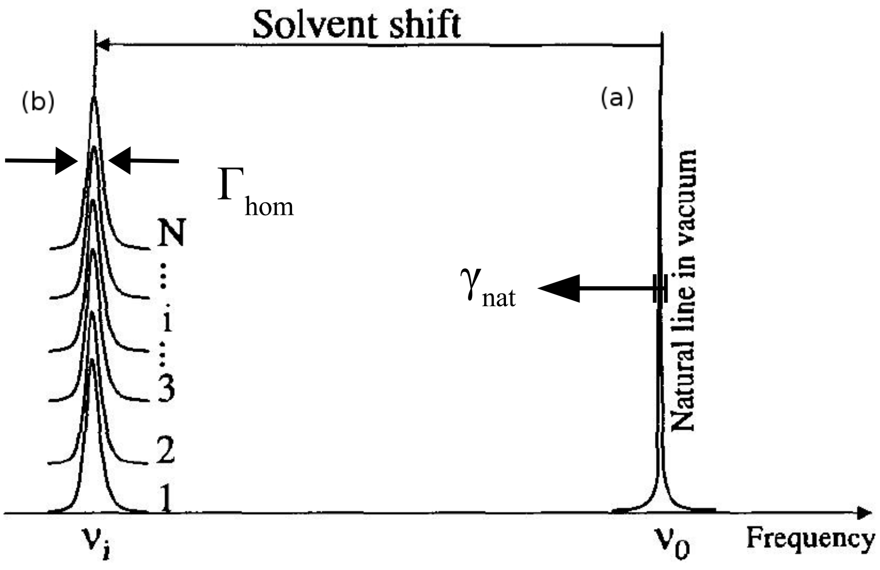

Figure 3.3. The intense narrow absorption line of the N identical hypothetical molecules in (a) an otherwise empty space and (b) an identical environment (solvent) which causes an evenly shift in the position of absorption spectra form υ_0 to υ_1. Adapted with permission from [8], Copyright © 2004 by World Scientific Publishing Co. Pte. Ltd.

On the other hand, interaction with vibrations of the environment destroys the phase coherence [33] without removing the molecule from the electronically excited state. Therefore, τ_2 depends both on the decay processes of the excited state and on all thermal interactions with the surroundings (pure dephasing). In other words, random interactions between individual molecules and their surroundings lead to fluctuations in the interaction energy, which appear as time dependent parts of the wavefunctions of the molecules. These fluctuations result in getting them out of phase faster. Hence, pure dephasing originates from the thermal motions of the host and consequently would be infinitely slow when the temperature tends to absolute zero. In this case τ_2 is twice τ_1 . These relaxation times are related to homogeneous line width through the following equation[1],

$$\Gamma_{hom}=\frac{1}{\pi\tau_2}=\frac{1}{2\pi\tau_1}+\frac{1}{\pi\tau_2^*(T)} \qquad (3.13)$$

The reason for the temperature dependence of the homogeneous line width is clear from eq. 3.13: since $1/\tau_2^*$ is not exactly zero except for at absolute zero, Γ_{hom} is greater than γ_{nat}, which is related only to τ_1.

Thus far, absorption (or fluorescence) spectra of molecules in vacuum and in a homogeneous solvent have been discussed. Inhomogeneous broadening is a common phenomenon in spectroscopy. It basically means that the absorption band of an ensemble consisting of identical molecules (chromophores, dye molecules, or inorganic ions) is actually several orders of magnitude broader than the line width of one of them in isolated form. In the case of dopant molecules (guests) in solid materials, there are two possibilities. First, the host is a perfect crystal; therefore, all guest molecules experience the same environment and absorption spectra have features similar to Fig. 3.3. Essentially, the case of a perfect crystal resembles the case of a hypothetical uniform environment discussed above. Fig. 3.4 reflects this situation, and in addition to narrow linewidth, it shows also the accompanying PSB. The ZPL width would still be the same homogeneous width[2].

---

[1] $\tau_2^*(T)$ emphasizes that the pure dephasing is a temperature dependent process.

[2] It should be noted that in practice even if the molecule is isolated, there will be some PSB-like features due to molecule's own vibrations. And if the molecule is complicated enough, there will be many of them. The difference with the PSB is that (delocalized) phonons give continuous low-frequency distribution, while molecule's own (local) vibrations give a set of discreet frequencies, extending to couple thousand wavenumbers in the case of chlorophylls.

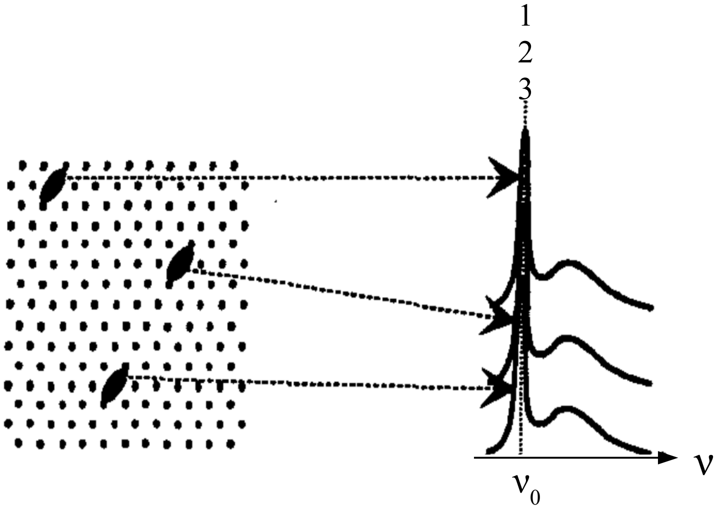

Figure 3.4. The spectra of three identical isolated pigments in a perfect crystal which are the same. Adapted with permission from [8]. Copyright © 2004 by World Scientific Publishing Co. Pte. Ltd.

In the second case, the host medium is amorphous, and each guest molecule experiences a different environment, which causes dispersion in the absorption spectrum or *inhomogeneous broadening* (Γ_{inhom}) depicted in Fig. 3.5.

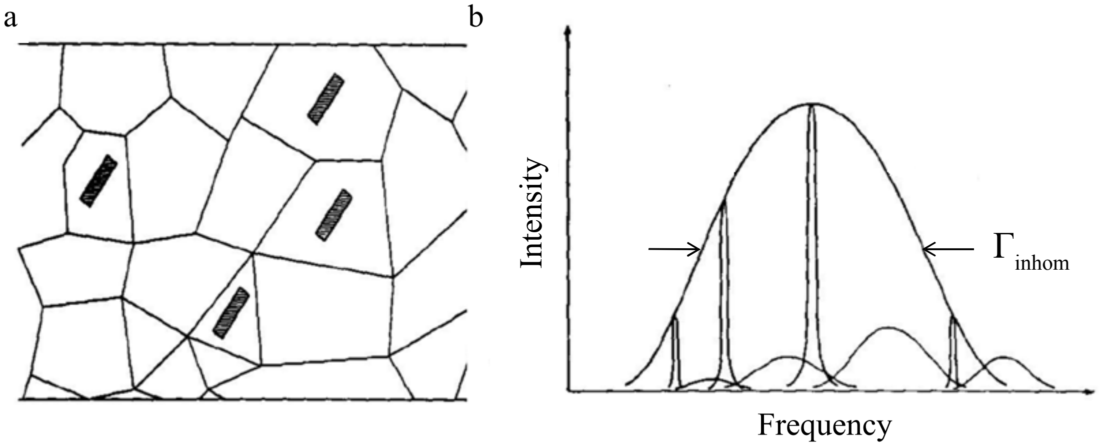

Figure 3.5. (a). Three molecules in an amorphous environment. (b). The corresponding absorption spectrum. Adapted with permission from [33]. Copyright © 2001, American Chemical Society.

It should be pointed out that an inhomogeneously broadened absorption spectrum consists of different peaks of those chemically identical molecules in non-identical local environment. The function which describes the distribution of probability of encountering a 0-0 transition (ZPL) at a specific wavelength is the *site distribution function* (SDF). Thus, the ensemble absorption spectrum is the result of convolution of the SDF with a single molecule absorption spectrum (Fig. 3.6), or *single site absorption* (SSA).

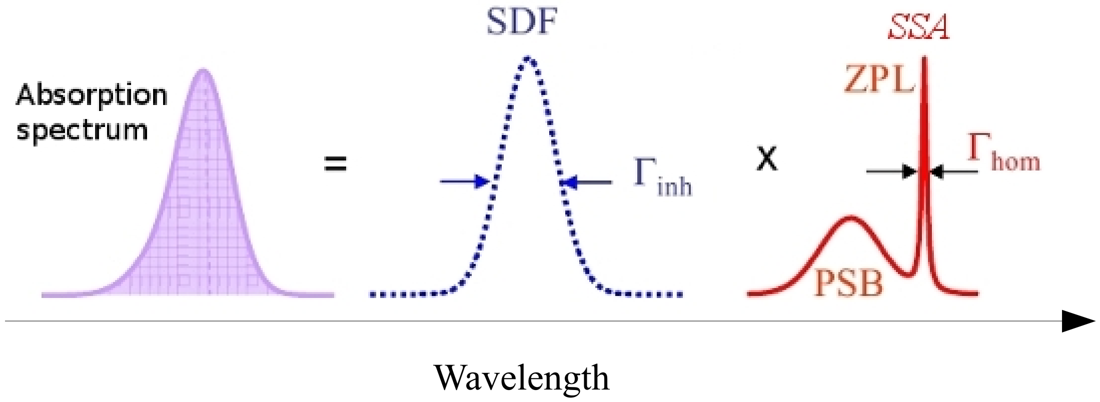

Figure. 3.6. The absorption spectrum (x-axis is wavelength) of an ensemble is a convolution of SDF with the absorption of a single molecule [35].

Inhomogeneous broadening for proteins is of the order of 100 cm^{-1}; in the case of crystals this value may decrease to around 1 cm^{-1}. Not to zero, since in reality there are no perfect crystals and the situation is in between the perfect ideal crystal and an amorphous solid [33]. Importantly, 100 cm^{-1} is several orders of magnitude more than the typical low-temperature homogeneous line widths (~1 GHz in the absence of energy transfer, determined mostly by pure dephasing) observed in proteins, and it is clear that for studying proteins (or generally, amorphous solids) inhomogeneous broadening should be removed by proper methods.

3.3. Spectral Hole Burning (SHB)

Invention of narrow-line lasers made it possible to excite selectively only a fraction of all molecules, those with the ZPL resonant with the laser. Upon excitation these molecules may stop absorbing the light at the laser frequency (burn frequency) for two reasons: a) their chemical structures have been affected by the laser light so that they are not capable of light absorption at the burn wavelength anymore (molecules experienced a photochemical reaction) or b) the excitation by laser triggers some conformational change in the molecules' immediate environment. As a result, molecules' transition frequencies change (solvent shifts change), and the molecules do not absorb at their original wavelength any more. When the reason for HB is a consequence of chemical change in the structure of the guest molecule, it is called photochemical hole burning (PHB) and it is usually a non-reversible process (it can be compared with photo-bleaching). A notable exception is the reversible tautomerization of free-base chlorin. In the case of PHB, the burnt molecules (photoproduct, or, shortly, product) structure changes completely to a different structure with respect to the non-burnt molecule (educt). This kind of burning is out of the scope of this thesis.

However, the burning mechanism in the second case, so-called non-photochemical hole burning (NPHB), is a result of physical change in the surrounding host, and burnt molecules' absorption can be found close to the burn frequency (Ω_B). The absorption spectrum usually can be recovered to the pre-burn condition by either waiting long enough at the burn temperature (the spontaneous recovery) or by elevating the temperature enough to cross the barriers. The full spontaneous recovery takes a lot of time, many days, at low temperatures.

In either case, the *hole burning spectrum* (HBS) can be obtained by subtracting pre-burn (*A(Ω,0)*, initial absorption) from the post-burn (*A(Ω,t))* absorption spectrum, where *t* is the burning time:

$$HBS = A(\Omega, t) - A(\Omega, 0) \tag{3.14}$$

The *fractional hole depth* (FHD), an important parameter in hole spectra analysis, is determined by,

$$FHD = 1 - \frac{A(\Omega, t)}{A(\Omega, 0)} \tag{3.15}$$

Sketches of pre-burn and post-burn spectra are shown in Fig. 3.7. (The mode of SHB of interest to us is NPHB. Keeping in mind that the term “photoproduct” or “product” often implies some chemical reaction occurring in the guest molecule, the term “product” might not be used and the proper word would be “anti-hole”.) From this figure it is clear that the main feature of the hole is an image of the ZPL in the absorption spectrum.

To find the relationship between the hole width and the homogeneous line width one has to notice that (as mentioned earlier) the absorption spectrum is a result of the convolution of the SDF with the SSA, and the SDF (Fig. 3.6) is modified following the burning. Then, the post-burn absorption spectrum after burning at ω_B, with photon flux *P* for time *t* is given by the SHB master equation [36] (assuming that the laser linewidth is much narrower than homogeneous width):

$$A(\Omega,t)=1.5\int d\omega\, L(\Omega-\omega)G(\omega)\int d\lambda\, f(\lambda)\int d\alpha \sin\alpha\cos^2\alpha\, e^{-Pt\sigma\phi(\lambda)L(\omega-\omega_B)\cos^2\alpha} \quad (3.16)$$

where $G(\omega)$ is the pre-burn SDF which is usually Gaussian, $L(\Omega\text{-}\omega)$ is the SSA that consists of the ZPL and the PSB and its area is normalized to one on the frequency ω scale. $f(\lambda)$ is the distribution of the tunneling parameter in the excited state. In Shb analysis it is assumed to be a Gaussian with a standard deviation of σ_λ and a mean value of λ_0. α is the angle between the pigment's transition dipole vector and the laser polarization, σ in the exponential is the integrated absorption cross-section of the chromophore, and $\varphi(\lambda)$ is the NPHB quantum yield given by:

$$\phi(\lambda)=\frac{\Omega_0\exp(-2\lambda)}{\Omega_0\exp(-2\lambda)+\tau_1^{-1}} \quad (3.17)$$

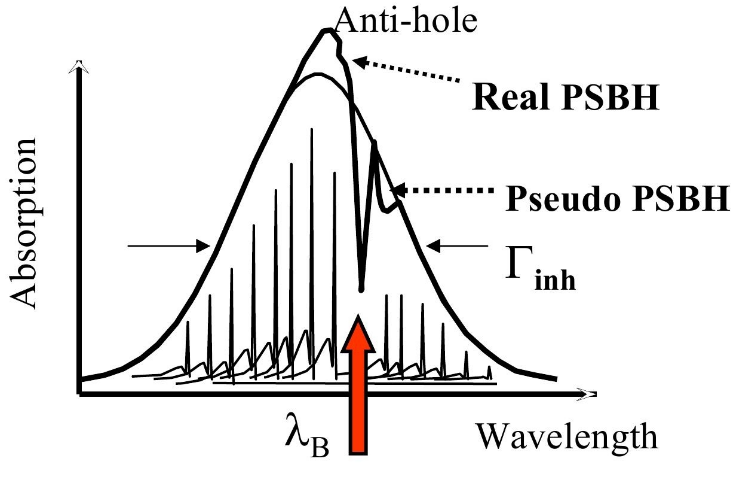

Figure 3.7. The different features of NPHB including ZPH, real PSBH, and pseudo PSBH [35]. Using the term photoproduct is not the best choice for NPHB. The more sophisticated term is anti-hole (see the text).

The experimentally observed hole is the result of the convolution of the ZPL-shaped hole in the (modified) SDF with the SSA spectrum (also containing the ZPL). As both are Lorentzian, based on Lorentzian function properties, the hole width is

$$\Gamma_H = 2\Gamma_{hom} \tag{3.18}$$

At $T = 0$ the contribution of pure dephasing to line broadening is absent, and eqs. 3.12 and 3.18 give the relation between hole width and fluorescence lifetime as shown below:

$$\Gamma_H = 2\Gamma_{hom} = \frac{1}{\pi\tau_1} \tag{3.19}$$

Thus, finding the fluorescence lifetime from the SHB is very straightforward in theory. However, in practice, even at $T = 4\ K$ pure dephasing is dominant, and one has to determine the fluorescence lifetime using other techniques. Then, the pure dephasing contribution, which is related to the dynamics of the host molecules can be found through eq. 3.12.

There are several additional features in the NPHB spectrum which are shown in detail in Fig. 3.7. A molecule which is in resonance with the laser has a ZPL and a PSB. When such a molecule gets burnt, both its ZPL and PSB will disappear from the post-burn spectrum. The lack of the ZPL and the PSB in the post-burn spectrum corresponds to the zero phonon hole (ZPH) and the “real” phonon side band hole (PSBH) respectively. Additionally, some molecules having the PSB at the burn wavelength may burn non-resonantly while excited via their PSB, which gives rise to “pseudo PSBH”. In other words, the latter is a sum of the ZPL burnt via their PSB.

One of the biggest advantages of SHB in comparison with the other high resolution techniques for removing inhomogeneous broadening is the possibility of applying it in both absorption and fluorescence mode. Therefore, it is useful for studying both fluorescent and non-fluorescent molecules.

3.4. Protein Energy Landscape

A functional protein like myoglobin has several conformations or states as opposed to a crystal which always has a well determined periodic structure in all situations. In addition, the hydrogen bonds can have somewhat variying positions and the side chain locations of the amino acids in different individual protein molecules are not perfectly identical. Consequently, each single protein molecule has to some extent a different structure which is called the conformational substate [3]. The biological function of different but nearly identical conformational substates of a specific protein is similar, however since their structural details are different, the performance (or rate) of some process of interest might be different in each conformational substate. The minima corresponding to individual substates and the respective barriers separating them collectively form the protein energy landscape.

There are different types of degrees of freedom in protein systems such as bond length, the angle between bonds, the positions of free molecules, moving a ligand, each of them associated with a generalized coordinate. Although at low temperatures most of those degrees of freedom are frozen out, proteins still are not completely static, and the polypeptide backbone and side chains of proteins are moving constantly due to interaction with their environment (e.g. due to thermal fluctuations, exciton-phonon interactions, etc.). The fictitious example of the potential energy in an amorphous host with respect to a generalized coordinate is shown in Fig. 3.8 [8].

The potential energy in amorphous materials (i.e. proteins or glasses) has several different local minima. In Fig. 3.8 each of them represents a specific molecular configuration [8]. In the case of proteins, the picture with just one generalized coordinate is extremely oversimplified, as the energy landscape is in fact multidimensional. Consequentially, there are multiple routes to be navigated by proteins between any two different states, for instance between unfolded (non-functional) and folded (functional) states [37].

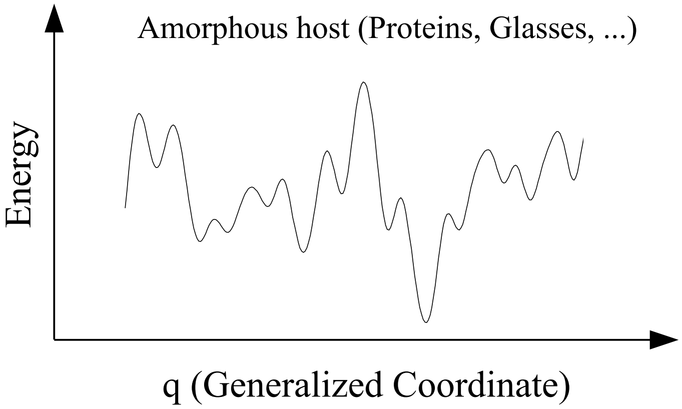

Figure 3.8. The potential energy landscape for amorphous hosts (e.g. proteins, glasses) with several local minima (figure based on Fig. 13 on p. 108 of [8]).

However, we will temporarily take a step back from complicated multi-dimensional landscapes and consider what we can learn from much simpler related systems. The behavior of a disordered solid can be explained using just double-well potentials as one shown in Fig. 3.9. Briefly, the idea is that in an amorphous material, some molecules or groups of molecules can have only two equilibrium positions with almost identical energies. Thus, instead of using energy landscapes (like shown in Fig. 3.8), one can use an ensemble of systems with only two wells separated by a barrier, where the parameters of these two wells (barrier heights, asymmetries, and distance between the minima) are subject to distribution (Fig. 3.9). This model is called the two level system (TLS).

Historically, this model was devised to explain various anomalous properties of amorphous solids at low temperatures such as heat capacity, heat conductivity, etc. [38]. It should be noted that it is still unknown which particular groups of atoms are involved in the TLS in most amorphous solids. The two local energy minima with potential barrier (*V*), asymmetry parameter (*Δ*, the difference between the zero level of the phonon/vibrational mode in each of the minima), and the distance between the two minima (*d*) are shown in Fig. 3.9 [39].

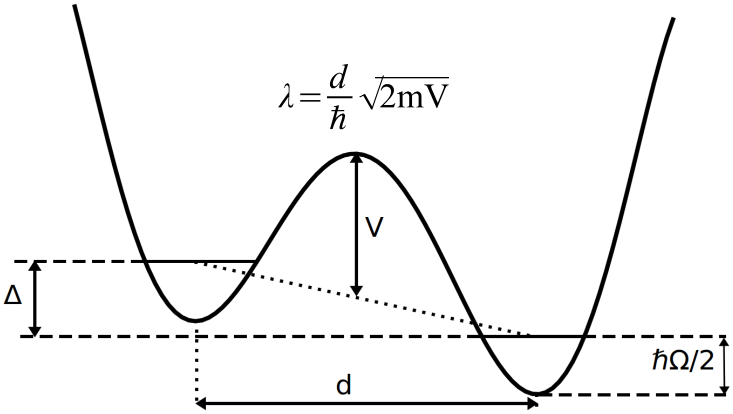

Figure 3.9. TLS model for glasses with various parameters [39].

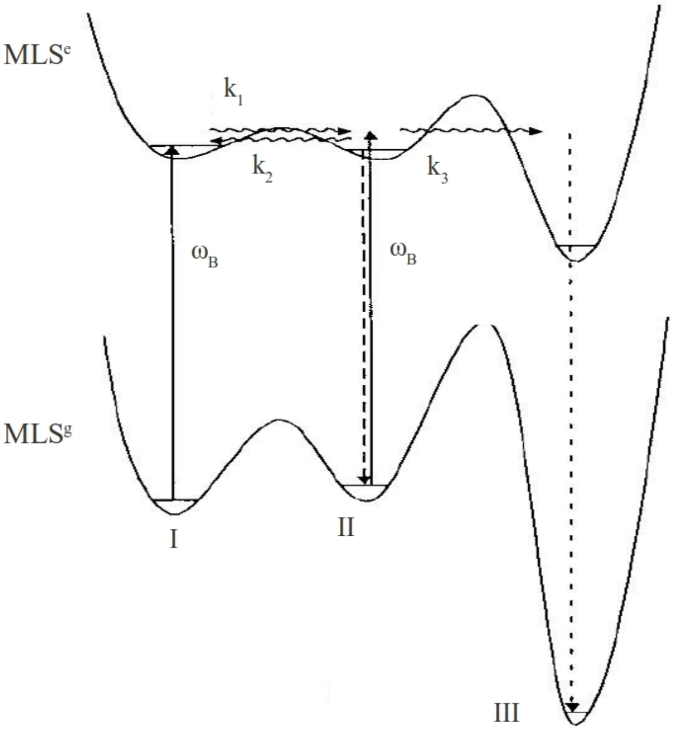

Figure 3.10. The schematic of multilevel system (MLS) model which explains NPHB in proteins more precisely than TLS. I, II, and III denote the pre-burn structure and two possible post-burn structures respectively. k_1, k_2, and k_3 are three different tunneling rates in the excited state between shown structures, and ω_B is burning frequency. Adapted with permission from [40]. Copyright © 2001, American Chemical Society

Also $\hbar\Omega/2$ is the lowest vibrational energy in each state. The horizontal axis in this schematic is a generalized configuration coordinate. The predominant process for transition between these configurations at low temperature is tunneling through the barrier (barrier hopping at low temperature has negligible contributions). The tunneling parameter λ can be expressed via barrier parameters [8] as:

$$\lambda = \frac{d}{\hbar}\sqrt{2\mathrm{mV}} \tag{3.20}$$

here *m* is the effective mass of the tunneling entity rearranging during conformational change.

In proteins, one can imagine TLSs connected to each other which results in the formation of multilevel systems as shown in Fig. 3.10. The idea can be further expanded into energy landscapes which we already introduced.

The existence of a large number of factors affecting the exact protein structure leads one to accept that the conformational energy space for proteins is rugged with lots of small barriers which are separated by higher barriers as shown in Fig. 3.11 (there are some approximately degenerate minima instead of only a single lowest energy).

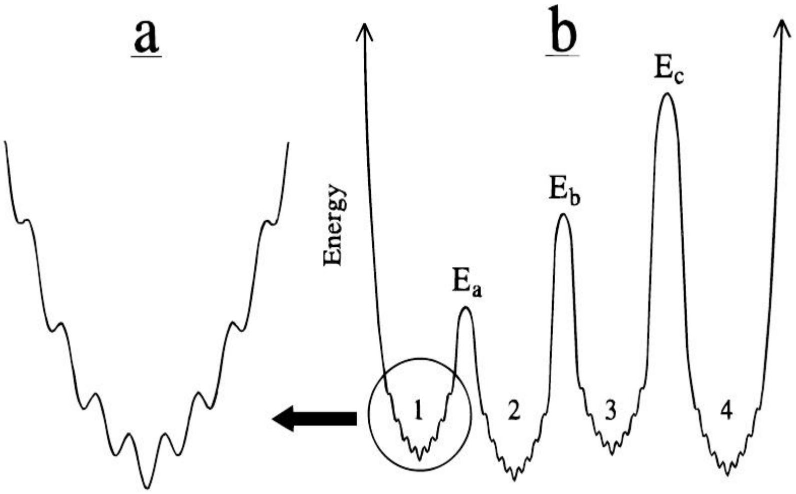

Figure 3.11. Different conformational substates and three tiers of the energy landscape of myoglobin. Adapted with permission from [3]. Copyright © 1997, American Chemical Society

The barriers between the conformational substates can be categorized based on the average barrier heights in a hierarchical fashion, i.e. into so-called tiers. This means that in the lower tier, the average barrier heights and distances between neighboring wells are smaller in comparison with the higher tiers. The three tiers of the protein energy landscape shown in Fig. 3.11 would be: I) the barriers of part (a); II) the tier containing wells 1, 2, 3 and 4; and III) the structure containing global minima similar to the whole part (b). In practice, three tiers of the protein energy landscape have indeed been observed by single molecule spectroscopy in case of LH2 light-harvesting protein [41].

It is widely believed that all kind of dynamics of proteins can be addressed by determining various parameters of the energy landscape [16]–[18]. Thus the main goal of all investigations in this thesis is finding the relevant information about these landscapes by optical spectroscopy techniques. The changes in chromophores, or pigments, spectral properties are due to changes in their protein environment.

3.5. The Mechanism of NPHB

The most common explanation for NPHB in amorphous solids is based on a TLS model expanded to include both the ground and excited electronic states of the guest molecule as shown in Fig. 3.12. Only two minima of the higher tier of the energy landscape are depicted for the sake of simplicity; the actual number of minima on the protein energy landscape is certainly larger. If the barriers in the excited state are significantly lower than in the ground state, the system may, starting from well 1 with

ΔE_1 corresponding to the laser frequency, experience a transition from one well to another within the lifetime of the excited state, return to the ground state, and remain trapped in state 2 for a relatively long time, determined by the ground state barrier parameters. Hence, the wavelength of the final product (anti-hole) is almost the same as the initial one before burning, meaning that the shift of absorption as a result of burning would be small [42]. (In the PHB, as noted before, the shift is usually considerably larger.) This shift of a guest molecule line can be detected directly in SMS experiments as stochastic line jumps upon each laser scan [43]. The barrier parameters are introduced in Fig. 3.12.B which may represent either the ground or excited state. The transitions between the two wells may involve either tunneling or barrier hopping, with NPHB, according to [44] and [45], being due to tunneling in the excited state.

So far, the model is no different from the TLS model employed to explain SHB in glasses, but we further expand it to include the second, lower hierarchical tiers of the protein-energy landscape (Fig. 3.12.C). For the sake of simplicity, the landscape is shown as one-dimensional, while in fact the number of relevant dimensions (independent generalized coordinates) may be much larger.

The (downhill) tunneling rate is [46]–[48],

$$R=\left(\frac{3f^2W^2E}{16\pi\rho c^5\hbar^5}\right)\left(n(E)+1\right) \tag{3.21}$$

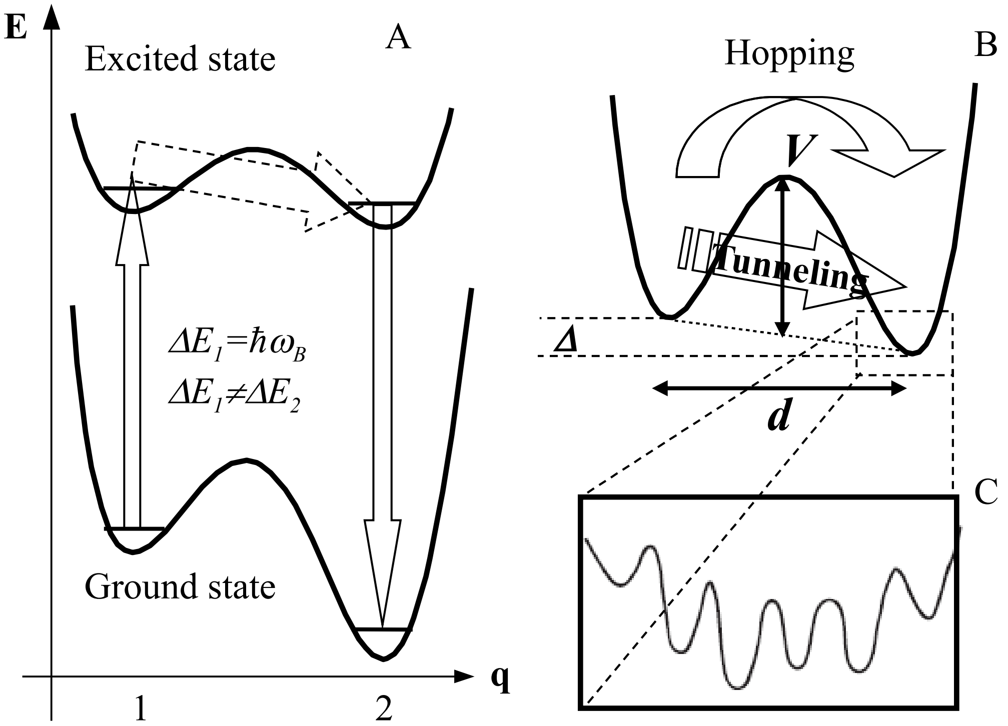

Figure 3.12. The simplified mechanism of NPHB in terminology of the TLS[1]. (A) Both excited and ground states of the pigment in interaction with protein are shown. ω_B is the burn frequency; the pigment/TLS in well 1 is initially in resonance with the laser. After (the initially unspecified) transition between the TLS wells, occurring while the pigment is in the excited state, the system may get trapped in well 2. (B) Detailed representation of the TLS (a fraction of the protein energy landscape) with the pigment in either the excited or ground states, introducing relevant parameters and possible transition processes. (C) Second, lower-barrier hierarchical tier of the protein energy landscape. The larger-barrier tier is responsible for NPHB, while the smaller barrier tier is responsible for hole broadening. Adapted with permission from [42]. Copyright © 2012, American Chemical Society.

---

[1] In glass theory, there are two types of TLS, intrinsic and extrinsic. The former exist in glass regardless of if there is chromophore / impurity (“guest”) or not, and the latter include interacting pigment and amorphous host. However, in photosynthetic protein complexes this distinction gets blurred since the guest (chlorophyll) is not introduced artificially.

where f is the TLS deformation potential, W is the tunneling frequency ($W = \omega_0 \exp(-\lambda)$, and λ is the tunneling parameter, eq. 3.20), E is the tunneling splitting given by $E^2 = \Delta^2 + W^2$ (Δ is the asymmetry parameter, which is usually much larger than W), ρ is the local sample density, $n(E, T)$ is the phonon thermal occupation number, $n = (\exp(E/kT) - 1)^{-1}$, c is an average speed of sound in amorphous solid media, and $\hbar$ is Planck constant over 2π. It should be mentioned that tunneling is phonon-assisted, and its rate depends on the availability of phonons satisfying conservation of energy (phonon energy change is equal to the TLS asymmetry). Therefore for downhill tunneling, the phonon gains energy, so it can have as low energy as one likes to begin with. However for uphill tunneling, the phonon has to have enough energy to give to enable tunneling. This results in the modification of eq. 3.21 for uphill tunneling as follows:

$$R_{uphill} = \left(\frac{3 f^2 W^2 E}{16 \pi \rho c^5 \hbar^5} \right) n(E, T) \tag{3.22}$$

Thus, the detailed balance condition for the uphill and downhill tunneling rates is satisfied.

These equations could be written in a simpler way [49]:

$$R_{downhill} = \Omega_0 \exp(-2\lambda)(n(E, T) + 1) \tag{3.23}$$

$$R_{uphill} = \Omega_0 \exp(-2\lambda) n(E, T) \tag{3.24}$$

where $\Omega_0 \approx \omega_0$ is the tunneling prefactor, the so-called attempt frequency, of the order of 10^{12} Hz [50]. The concept of attempt frequency is introduced in quantum mechanics for the crossing rate over a barrier between two wells. It represents how many times a particle attempts to pass the barrier per unit time. In solids, it is the vibration frequency of the relevant atoms [51]. In the context of this thesis, it means that there are many attempts to change from one conformation to another one. This is true that there is not enough energy to cope with this change but due to the nature of the subatomic world some of those non favorable changes (in terms of energy) can happen occasionally (modeled as tunneling through barriers).

As was shown above, theoretically, the shape of a spectral hole is Lorentzian and its width is twice the homogeneous linewidth, but in practice it has an additional contribution which can make it broader as shown in below equation

$$\Gamma_H = 2\,\Gamma_{hom} + \Gamma_{SD} \tag{3.25}$$

where Γ_{SD} is width due to *spectral diffusion* (SD), which is both temperature and time dependent. In terms of Fig. 3.12, spectral diffusion is due to conformational changes on the smallest-barrier tier of the protein energy landscape. Exploring SD (i.e., the hole width dependence on time) is a powerful tool to investigate host-matrix dynamic behavior. In fact, the distinction between factors affecting Γ_{hom} and those affecting Γ_{SD} is largely quantitative and not qualitative. Dynamic interactions between host and guest which are faster than the minimum timescale of the experiment are responsible for observed homogeneous broadening [52]. SD reflects interactions on a slower time scale. Since the hole width will become broader because of spectral diffusion (spontaneous or light induced), measuring the hole width for the purpose of determination of the excited state lifetime should be done as quickly as possible, so that spectral diffusion cannot significantly affect homogeneous width.

3.6. Hole Growth Kinetics (HGK)

One of the techniques in SHB, useful for the determination of TLS or the energy landscape barrier parameters, is investigating the growing of a hole (decrease of absorption or fluorescence excitation signal) with increasing irradiation dose, which is called hole growth kinetics (HGK). The irradiation dose is defined as the product of power density (which is constant during the measurement) and time. Therefore, in HGK the fractional hole depth (FHD) is measured versus the irradiation dose. This is done by burning a hole at a certain wavelength and collecting the fluorescence signal by a photomultiplier tube at the same time till there is (almost) no more decrease seen in the fluorescence signal. As the burnt molecules are not excited and therefore do not fluoresce any more, the fluorescence signal should decrease in an exponential fashion. However, in practice, HGK cannot be fitted by a single-exponential curve due to dispersion of the hole burning rates, eq. 3.16. As will be discussed below, this dispersion of burn rates originates from the dispersion of the barrier parameters (in TLS or on the protein energy landscape). After the hole growth kinetics measurement, the hole spectrum is scanned to compare its fractional depth with the one resulting from the HGK measurement. (To ensure that the HGK curve is not affected by the presence of any transient features.) Hole spectrum is measured by scanning the region around the hole (e.g. about 40-45 GHz around the burn frequency, for our particular equipments) with weaker intensity (read intensity ~1000 times smaller than burn intensity). The most critical parameters which can be found from HGK measurements are the electron-phonon coupling (*S*), the tunneling parameter distribution mean (λ_0) and its standard deviation (σ_λ) in the excited state (since burning is happening in the excited state, HGK studies excited state parameters). Other parameters are either determined by experimental conditions (e.g. photon flux) or are measured independently (SDF and SSA spectrum parameters). S can be found directly from the saturation depth of HGK since the maximal ZPH depth is approximately equal to e^{-S}. (Once all the resonant ZPLs are burnt, only the PSB are left, and the burning becomes much slower.) λ_0 and σ_λ are found by fixing all the other parameters in eq. 3.16 to the values obtained independently from other experiments (e.g. PSB shape, PSB/ZPL ratio, fluorescence lifetime, etc.), and then trying to find the best λ_0 and σ_λ for the HGK curve. Qualitatively, changing λ_0 leads to shifting HGK curve towards higher or lower dose without changing its shape (on a logarithmic dose scale), and different values for σ_λ give different curvature (large σ_λ results in a flattened line and smaller σ_λ give more sigmoidal curves on a logarithmic scale). The effect of changing of σ_λ is shown in Fig. 3.13 for a hypothetical measurement [53]. It should be emphasized that the whole distribution of λ in the excited state can be found from the fit to a sufficiently saturated hole (burning all the ZPL and PSB). The shape of the HGK is determined by the interplay between what is already burnt and what is not yet burnt. On the other hand, only some part of the excited state barrier distribution is encoded into the spectral hole and can be probed by subsequent hole recovery or hole broadening experiments [42]. Saturation of the hole, usually meaning saturation of the ZPL, is required for a wider dynamic range and more reliable distribution parameters.

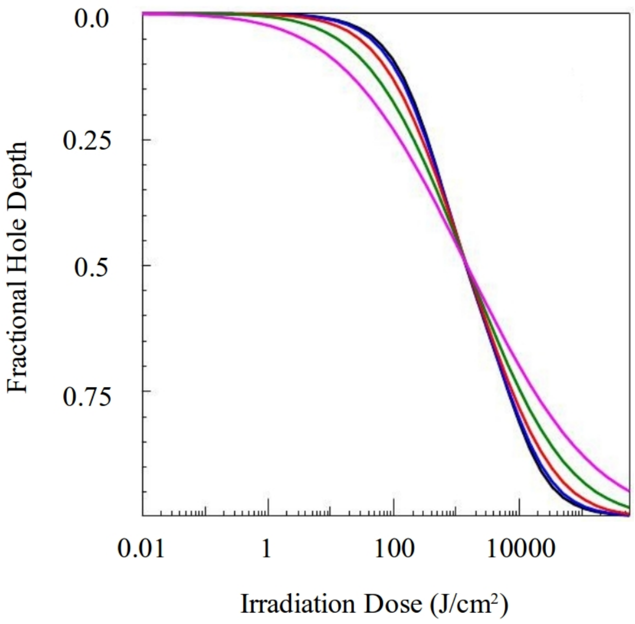

Figure. 3.13. HGK curves for different parameters. Changing σ_λ leads to different curvature in HGK curve. $\lambda_0 = 10$ *and* σ_λ = 0.0 (no dispersion; black), 0.3, 0.6, 1.0 and 1.5 (magenta). Note that high irradiation doses are in practice obtained as a combination of relatively low intensities and long (hours) burn times. Adapted with permission from [53]. Copyright © 2011, American Chemical Society.

3.7. Hole Recovery (HR)

As it was mentioned above, hole growth kinetics contains information about parameters of EL in the electronic excited state of the pigment-protein system while the recovery of a hole can give those parameters for the ground state. The HR can occur either spontaneously (at burn temperature) or upon thermocycling. Hole recovery is a result of sample's tendency to return to its pre-burn state (or, more precisely, to equilibrium situation, see Chapter 5). There is always some recovery via tunneling even at the lowest temperatures, although it may be very slow (e.g. a hole with original fractional depth of 37% in CP43 can recover about 35% of its area in about 3 hours at 5 K, as shown in Chapter 4). On the other hand, in the case of thermocycling increasing the temperature allows the systems to quickly cross some barriers by barrier-hopping, speeding up the relaxation of sample to pre-burn state or equilibrium. In the case of thermocycling the sample temperature after burning (and some spontaneous HR, see below) is raised to certain level and then lowered back. While heated, the host molecules have enough energy to rearrange, sometimes returning to the pre-burn conformational state. This may be the result of tunneling or barrier hopping in the ground state.

For calculating the hole area upon burning as a function of time and temperature (to explain both spontaneous and thermocycling recovery), we assume that the number of centers in the burned and unburned states are N_0 and N respectively. Assuming that λ distribution in the ground state is $g(\lambda)$[1] ($f(\lambda)$ in the excited state in eq. 3.16) and the rate which describes relaxation from the burned to unburned state at any specific temperature T is $R(\lambda)$ then the number of recovered centers having relaxation rate between $R(\lambda)$ to $R(\lambda+d\lambda)$ is $N_0 g(\lambda)\, d\lambda$[2] [56]. Therefore the number of remaining centers in the burned state with this relaxation rate is

$$dN(t,T)=N_0\, g(\lambda)\, d\lambda \exp(-R(\lambda)t) \tag{3.26}$$

where t is time . Hence the total number of non-recovered centers after time t can be

---

[1] This is really important that to fit the data of HR one has to consider plenty of configurational changes (corresponding to a continuous distribution of λ, $g(\lambda)$) which proves that burning is not the result of only one configurational change (or even a few of them) [54]–[56].

[2] By normalizing the λ distribution ($\int_{-\infty}^{\infty} g(\lambda)\, d\lambda=1$), N_0 will be considered 1.

calculated by taking integral over all possible *λ* as follows

$$N(t,T)=N_0\int_0^{\infty} g(\lambda)d\lambda\exp(-R(\lambda,T)t) \tag{3.27}$$

It should be noted that *R* the relaxation rate, depends on both *λ* and *T*. For 5 K hole filling, there are some evidences that the dominant process is tunneling and not barrier hopping. The results will be shown in Chapter 4. Briefly, it is concluded from the independence of the burning and recovery rates on temperature up to ~10K. Therefore *R* in eq. 3.27 is most likely defined by eq. 3.23 that describes downhill tunneling. Uphill tunneling will obey eq. 3.24. It should be mentioned that uphill tunneling is less likely. However if this is the case, *n(E)* is much smaller than 1 for realistic barrier parameters (and more strongly temperature-dependent, contrary to experimental results). Hence we use eq. 3.23 to find *R* for 5 K hole filling and eq. 3.27 becomes:

$$N(t,T)=N_0\int_0^{\infty} g(\lambda)d\lambda\exp(-\Omega_0\exp(-2\lambda)(n(E,T)+1)t) \tag{3.28}$$

T in this equation is the same as the burn temperature (e.g. 5 K) and *t* is the relaxation time (discussed below). In case of thermocycling, however, barrier hopping should be taken into consideration. The hopping rate is determined by

$$R_{hopping}=\Omega_0\exp\left(\frac{-V}{k_B T}\right) \tag{3.29}$$

where *V* is the barrier height between two wells (see Fig. 3.9) and *Ω₀* is the attempt frequency for crossing the barrier which is assumed to be the same attempt frequency as introduced for the tunneling process. Thus, including both tunneling and hopping rates modifies eq. 3.27 for the thermocycling experiment as

$$N(t,T)=N_0\int_0^{\infty} g(\lambda)\,d\lambda \exp(-\Omega_0 t[\exp(-2\lambda)(n(E,T)+1)+\exp(\frac{\lambda^2\hbar^2}{2\mathrm{md}^2 k_B T})]) \qquad (3.30)$$

Here V is expressed via λ using eq. 3.20 ($V=\frac{\lambda^2\hbar^2}{2\mathrm{m}d^2}$). A new function is introduced to make eq. 3.30 shorter

$$q(\lambda,t,T)=\exp(-\Omega_0 t[\exp(-2\lambda)(n(E,T)+1)+\exp(\frac{\lambda^2\hbar^2}{2\mathrm{md}^2 k_B T})]) \qquad (3.31)$$

This function can have values from zero to one and describes how large fractions of systems with a given lambda are not recovered after time t at temperature T.

So eq. 3.30 can be written as

$$N(t,T)=N_0\int_0^{\infty} g(\lambda)\,d\lambda\, q(\lambda,t,T) \qquad (3.32)$$

Since *q(λ, t, T)* is a step-like function, eq. 3.32 can be interpreted as follows: by multiplying *q(λ, t, T)* by the ground-state *λ* distribution (*g(λ);* or, more precisely, the partial distribution encoded into the hole, see below), the smaller-lambda part of this (partial) distribution is chopped off, and the area remaining under the (partial) lambda-distribution curve, which is proportional to the hole area, is reduced (meaning the hole is partially recovered). In order to find the true g*(λ)* the hole should be recovered completely. The ground-state *λ* distribution (*g(λ)*) can be found by measuring the hole area evolution with time, calculating *q(λ, t, T)* and then modeling data with eq. 3.32.

Chapter 4

4. SHB Applications to the Dynamics of Photosynthetic Protein Complexes

In this chapter various parameters of energy landscape of some photosynthetic protein complexes are measured and the choice of the best subject for more detailed protein dynamics study is made based on these measurements. The data in this chapter is mostly based on following published papers with permission © 2012, American Chemical Society:

M. Najafi, N. Herascu, M. Seibert, R. Picorel, R. Jankowiak, and V. Zazubovich, "Spectral Hole Burning, Recovery, and Thermocycling in Chlorophyll–Protein Complexes: Distributions of Barriers on the Protein Energy Landscape," *J. Phys. Chem. B*, vol. 116, no. 38, pp. 11780–11790, Sep. 2012.

N. Herascu, M. Najafi, A. Amunts, J. Pieper, K.-D. Irrgang, R. Picorel, M. Seibert, and V. Zazubovich, "Parameters of the Protein Energy Landscapes of Several Light-Harvesting Complexes Probed via Spectral Hole Growth Kinetics Measurements," *J. Phys. Chem. B*, vol. 115, no. 12, pp. 2737–2747, Mar. 2011.

4.1. Introduction

SHB has been widely applied to determine the details of spectral diffusion and energy landscapes in glasses [44], [57]–[63] and proteins [5], [64], [65] at low temperatures. Chlorophyll−protein complexes in particular are ideal model systems for protein energy landscape research (thus the results of SHB applied to the dynamics of proteins are not limited to the photosynthetic complexes): here the pigments/“probes” are built into the protein by Nature (in a large variety of local environments) without extraneous chemical manipulations or genetic engineering. These are the pigment−protein interactions, which determine the transition energies of the pigments inside the pigment−protein complexes [66]–[69]. The site-energies, along with the inter-pigment interaction energies, determine the shapes of various optical spectra of the complexes [68]–[72], as well as the details of the energy transfer processes, which are part of photosynthetic light-harvesting. The energy transfer processes are affected not only by the static structure of the complex but also by the protein dynamics, including the slow processes. For example, anticorrelated behavior of the emission bands in single Photosystem I (PS I) complexes [73] indicates that energy transfer pathways can fluctuate following conformational changes in the protein. The light-induced shifts of the chlorophyll site energies (essentially, NPHB), which are determined by the properties of the protein energy landscapes, affect the positions and oscillator strengths of excitonic states [69]–[71]. These influence various optical spectra, including those of non-resonant NPHB [38], [45] and δ-CD [72] (circular dichroism).

Several classes of SHB experiments probe different aspects of the protein energy landscapes. Experiments on hole evolution during the burning process, in particular hole growth kinetics (HGK) [36], [49], [74]–[78] measurements, probe the distribution of barriers in the excited electronic state of a pigment−protein system. It has been demonstrated that HGK results for a variety of glassy [36], [49], [74]–[76] and protein [77], [78] systems are in good agreement with this model, employing Gaussian distributions of the tunneling parameter, λ [54], [57]. The latter is related to barrier heights and other system parameters via eq. 3.20 (see Fig. 3.9).

On the other hand, the distribution of barriers in the ground state has been explored by observing the recovery of previously burned holes, either at a fixed, low temperature (the same as the temperature at which the burning took place) or as a result of thermocycling [59], [63], [79]. The derivative of the dependence of the hole area on the cycling temperature yields the distribution of barrier heights [59], [63] (see Section 3.7.). It has been noticed long ago that in the case of glasses the resulting ground-state barrier distribution apparently is proportional to $1/\sqrt{V}$ [59], [60], [62] (corresponding to a uniform distribution of λ) [38], [80]. A notable exception is the work of Love et al., who observed a Gaussian barrier distribution in the ground state of the Tb^{3+}/ $Ba_{1-x-y}La_xTb_yF_{2+x+y}$ system [63].

In the case of proteins, a superposition of $1/\sqrt{V}$ and Gaussian components has been reported [5], [79]. Distributions of d and m are usually assumed to be very narrow and are neglected [59]. A decrease in the area of a hole is usually accompanied by an increase in the hole width, described by a spectral diffusion kernel [5], [61], [81]. This broadening was also reported to conform to an ~ $1/\sqrt{V}$ barrier distribution, although Jankowiak et al. [54], [82] demonstrated that a Gaussian λ-distribution may yield similar hole-broadening results for certain parameters.

One could argue that hole broadening is due to conformational changes on the fastest, smallest-barrier tier of the protein energy landscape [6], [41] (Fig. 3.9), while a hole area decrease is due to relaxation on the next, higher-barrier tier. NPHB (and hole recovery, HR) with a higher-barrier tier supposedly involves relatively large shifts of the pigment absorption frequency (large compared to the width of the hole and to the width of the high-resolution laser scan, ~1.5 cm^{-1} in this study). (NPHB on the lower-barrier tier can occur as well, but it contributes to the width of the initial hole.) Spectral shifts of different magnitudes, corresponding to different tiers of the protein energy landscape, have been directly observed in single photosynthetic complex spectroscopy (SPCS) experiments [41], [81], [83]. A Gaussian spectral diffusion kernel has been observed in SPCS experiments on LH2[1] for the smallest line shift tier of the protein landscape (characteristic shift magnitude ~1 cm^{-1}) [81]. The shapes of the barrier and shift magnitude distributions on the tier of the energy landscape corresponding to ~10 cm^{-1} spectral line shifts, however, remains undetermined by SPCS so far, most likely due to insufficient statistics.

SPCS is currently considered the technique of choice for spectral diffusion research, as it is free from the (sub)ensemble averaging inherent in SHB. However, there are several areas where SHB, despite its seeming shortcomings, can provide information

---

[1] This is the light-harvesting antenna in photosynthetic bacteria playing the same role (harvesting light and transferring the electronic excitation to the RC) as LHCII (in higher plants) even though their structures are not similar at all. Pigment molecules in LH2 (bacteriochlorophyll a, BChl a) are in two highly symmetric rings (one ring contains 9 well separated BChl a and the other ring includes 18 closely interacting BChl a with absorption peaks at 800 nm and 850 nm, so-called B800 and B850 bands, respectively) whereas chlorophylls arrangement are irregular in LHCII [84], [85].

relevant for interpretation of SPCS experiments and beyond. For instance, one question is whether the phenomena observed in SPCS experiments are predominantly thermally induced (i.e., are occurring anyway, whether one observes them in an optical experiment or not) or are measurement / light-induced (i.e., represent NPHB on a single molecule level; light-induced single molecule line jumps are well-known in glassy systems [86]–[90]. The results of SPCS could also be sensitive to the nature of local environment, for instance buffer to glycerol ratio and presence of polymers used in spin-coating SPCS samples [91]. Finally, it is not clear if large light intensities used in SPCS may result in significant local heating of the immediate environment of the chromophore.

In [77] it was suggested that joint analysis of the excited state barrier distribution data (and the resulting distributions of HB yields) obtained from SHB experiments and of photon budgets of SPCS experiments allows one to distinguish between these possibilities (with the conclusion being that low-temperature SPCS line shift observations are mostly light-induced). A related question is whether the observed line shifts are due to tunneling or barrier hopping [92]. The latter question will be addressed here.

The SHB experiments also naturally deliver ensemble averages, which can be compared with the averages of the SPCS data in order to tell if particular SPCS experiments probe relevant dynamics of the intact sample, not perturbed by preparation.

In summary, there is the need for improved qualitative and quantitative understanding of energy landscape barrier distributions. There is also a contradiction between the shapes of the barrier distributions for the tier of the protein energy landscape responsible for light-induced line shifts of around 10 cm^{-1}, with the HGK results being in agreement with a Gaussian barrier distribution in the excited state and thermocycling results suggesting a $1/\sqrt{V}$ barrier distribution in the ground state. The shape of this distribution is important in various theories concerning the low-temperature properties, not only of proteins but also of other amorphous solids (see refs [38], [54], [80], [82] and references therein).

We demonstrate that SHB and hole recovery studies of the same system (and within the framework of one unified model) can resolve this contradiction. We test the ability of Gaussian and uniform λ-distributions to explain both the hole-burning and hole-recovery (including thermocycling) results in a unified way, and show that only Gaussian distributions properly describe all data discussed below. We also present arguments showing that tunneling is the key mechanism responsible for NPHB in pigment−protein complexes (as well as for the line shifts in SPCS experiments).

4.2. Experimental Setup[1]

Various spectra and HGK for CP29, CP43 and LHCII were measured at liquid helium temperature in a model A240 helium bath/flow cryostat (Ukrainian Academy of Sciences). The biochemical details of sample preparation are described in [70] and [25]. The proteins were isolated not within our group. They have been provided by reputable collaborators, namely Rafael Picorel / Michael Seibert (CP43), Klaus-Dieter Irrgang

---

[1] This section is mostly taken from [78] with permission © 2012, American Chemical Society.

(CP29) and Alexey Amunts / Nathan Nelson (LHCII). The prepared samples were stored in a refrigerator at -80 °C. They were diluted with glycerol (cryoprotectant) 40:60 several minutes before the start of the experiment (to avoid damage by glycerol, noticed in some complexes after long storage times) and then placed in a Eppendorf Uvette featuring orthogonal optical paths of 10 and 2 mm. The use of the eppendorf Uvette allowed absorbance (10 mm path; moderate OD) and fluorescence excitation (2 mm path, reflection geometry; small OD to avoid reabsorption effects) measurements with the same sample (see Fig. 4.1).

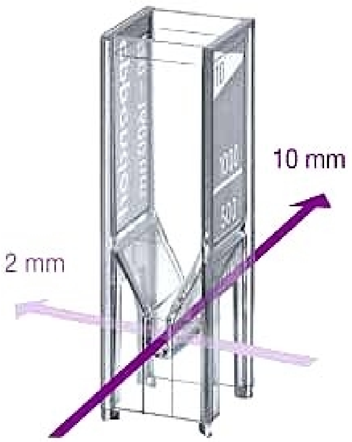

Figure 4.1. An eppendorf Uvette (http://www.fronine.com.au/epdorf_uvette.asp). Arrow indicates the light path in the case of transmission / absorption experiment.

The samples were occasionally recycled. In this case, absorption spectra have been compared to those measured in previous rounds of experiments, and if the spectra were not identical the samples were discarded. We also note that the shapes of the absorption spectra did not exhibit any abrupt changes at any particular temperature, and evolved in agreement with increase of homogeneous line width and electron-phonon coupling with temperature. This indicates that cooling did not introduce significant changes to overall protein structure.

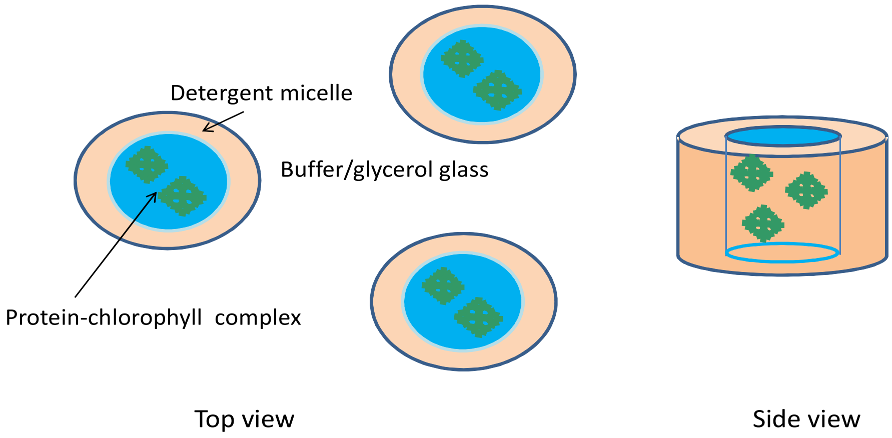

Figure 4.2. A cartoon of locations of PS complexes with respect to each other in a buffer/glycerol glass.

A cartoon of PS complexes located in buffer/glycerol matrix used in our measurements is shown in Fig 4.2. As photosynthetic protein-chlorophyll complexes are trans-membrane proteins, they have hydrophobic surface facing the membrane, so to solubilize them one has to use detergent, that forms micelles around the protein. However, the micelles are not spherical as the top and bottom of protein are hydrophillic. The interaction between complexes does not need to be considered since protein complexes have of the order of 10-15 chlorophylls per complex (or ~50 for LHCII trimer), and thus the protein concentration is of the order of 10^{-6} M or less (taking into account that the absorption peak in all complexes is about 0.5-1.3 and using peak *Chl a* extinction coefficient of 80000 M^{-1} cm^{-1}, one gets chlorophyll concentration of the order 10^{-5} M.). Thus, complexes are well separated and interaction between them can be neglected[1].

The absorption spectra were measured with a Varian Cary 5000 spectrophotometer at a resolution of 0.25 nm and the fluorescence spectra were measured using a Jobin-Yvon HR640 spectrograph with a Princeton Instruments Pixis CCD detector. The fluorescence spectra were corrected for the system sensitivity curve. The (low) extent of aggregation in the case of LHCII was also confirmed by measuring their absorption and fluorescence spectra.

High-resolution SHB experiments were performed with a Spectra-Physics/Sirah Matisse-DS tunable dye laser (DCM dye) pumped with a 6W 532 nm Spectra-Physics Millennia solid-state laser. The Matisse-DS is actively stabilized to <1 MHz bandwidth and is capable of seamless ~45 GHz scans even with passive frequency stabilization. The counterdrift function of the laser control electronics, including a HighFinesse WS-U30 wavemeter, allows for long-term (hours) stabilization of the laser frequency to <30 MHz for HGK measurements. (This precision is sufficient because homogeneous line widths in PS complexes at 5 K are on the order of one GHz due to pure dephasing [93], [94])

High-resolution spectra and HGK curves were detected in fluorescence excitation mode with a Hamamatsu PMT/photon counting module (with an AELP-730 interference long-pass filter, Omega, and some neutral-density and conventional long-pass filters,

---

[1] LHCII among all complexes has some tendency to aggregate. Aggregation is known to shift emission to the red, however, and we did not see such a shift our samples

LOMO, Russia), positioned at 90° with respect to the excitation beam. A Fresnel rhomb-based broadband polarization plane rotator (ThorLabs) was used to rotate horizontally polarized light emitted by the Matisse by 90° to achieve a situation where, given the geometry of the experiment, fluorescence from preferentially excited molecules was most effectively detected. Alternatively, the experiments were performed with a setup where optical setup around the cryostat and detectors was connected to the laser's table with a polarization-maintaining optical fiber (ThorLabs). Low (tens of $\mu W/cm^2$) intensities and long burn times were used to avoid local heating of the sample.

Contributions to the measured signal of the reflected excitation light or of cuvette material fluorescence were measured using a control sample containing a buffer/glycerol mixture only (no chromo-protein) for all filter combinations used in HGK measurements and subtracted from the respective HGK curves before fitting. It was also confirmed that the birefringence of the Uvette material was negligible [77]. The excitation intensity was stabilized by a power stabilizer (BEOC) and adjusted with neutral density filters (ThorLabs).

In thermocycling experiments, the temperature was controlled and stabilized using an UTREX temperature controller associated with the cryostat. The procedure for exploring HR and thermocycling was as follows: After burning a hole, the hole was first allowed to recover at a fixed (burn) temperature (5 K). The hole spectrum was scanned from time to time during this recovery phase. Alternatively, the signal at a fixed burn wavelength was monitored with low (read) intensity. Although the latter approach provided information only on the depth of the hole, it eliminated light-induced hole filling (LIHF, see details below) [95]. A couple of hours after burning, the thermocycling experiments were started. In these experiments, the temperature was raised to the desired level and then lowered back to the burn temperature of 5 K. The hole spectrum was always measured at 5 K. Then, the cycles were repeated with increasing maximal temperatures.

4.3. SHB Modeling

In the absence of energy transfer (this assumption is valid in our experiments since the lowest-energy state of each complex is being studied) the burning time dependent absorption spectrum can be calculated by eq. 3.16. This equation does not include the NPHB anti hole; however, it is valid for a wide range of irradiation doses. Two different approaches to including the NPHB antihole into consideration have been proposed. In [73], it was assumed that the chromophore interacts with one and only one TLS of the amorphous solid; therefore, the system has perfect spectral memory. (Upon light- or thermally induced hole filling, a chromophore always returns to the original preburn absorption frequency.)

Recent single complex spectroscopy results [81], [83], [96] suggest that a protein containing chromophore can assume more than two different conformations (different wells on the protein energy landscape [6], [41], [97]). The NPHB modeling procedure has been modified accordingly in [77], and the same procedure will be employed here as well. Namely, it was assumed that molecules starting at ω_{init} before burning are redistributed around ω_{init} according to a certain distribution, called an antihole function, as a result of burning. Unlike in refs [76] and [49], there was no spectral memory (i.e., it was assumed, based on SPCS results for LH2 [81], [83], [96] and LHCII, [98], [99] that the single molecule line can be found at significantly more than two frequencies), and no correlation was implied between the shifts of the absorption of a molecule in consecutive steps. (This distribution should agree with the distribution of line shifts observed in SPCS experiments, as was the case for LH2, except for the smallest-shift tier of the energy landscape [77]) The following sequence has been repeated in a loop: After a shallow burn, the SDF of the burnt molecules (i.e., $G(\omega)\left(1-e^{-Pt\sigma\phi(\lambda)L(\omega-\omega_B)\cos^2\alpha}\right)$; One starts with *G(ω)* being Gaussian.) was convoluted with the properly normalized antihole function and then added to the burnt SDF (i.e., $G(\omega)e^{-Pt\sigma\phi(\lambda)L(\omega-\omega_B)\cos^2\alpha}$). This results in a modified shape of the SDF *G(ω)*, without change in its normalization; the modified SDF is used at the next step of the burn sequence. The probability of burning at each step of the sequence was still determined by the standard SHB yield formula (eq. 3.17). (The SHB yield can be independently estimated from photon budgets and shift rates of the SPCS experiments [77]). The software was extensively tested with various parameters, and it has been confirmed that in the case when the antihole was shifted far away to the blue from the burn wavelength (and thus multiple acts of burning per single molecule were excluded), both programs (employed in this work and that of [76] and [49] with perfect spectral memory) yielded identical results. Because of large number of parameters in eqs 3.16 and 3.17, the simulations described below involved fixing most of these parameters to values independently available from the literature while we were fitting our HGK curves for the best barrier distribution parameters. Only when it proved impossible to obtain reasonable fits using parameters previously reported did we engage in varying other parameters, for example electron-phonon coupling strength in the case of LHCII.

4.4. Experimental Results

4.4.1. Sample Quality Test by Absorption Spectrum

The first step of our analysis is measuring the absorption spectrum of a sample to make sure that it has acceptable quality for our experiment (by looking at different features of this spectrum and comparing it with literature data) and storage did not affect the spectral properties. The absorption spectra of CP29, CP43, monomeric and trimeric LHCII are shown in Fig. 4.3. As an example of checking the quality of a sample based on its absorption spectrum, the well resolved absorption peak of CP43 in Fig. 4.3.B at ~683 nm indicates that this sample is intact. Losing this peak is the first sign of damage [72], [100].

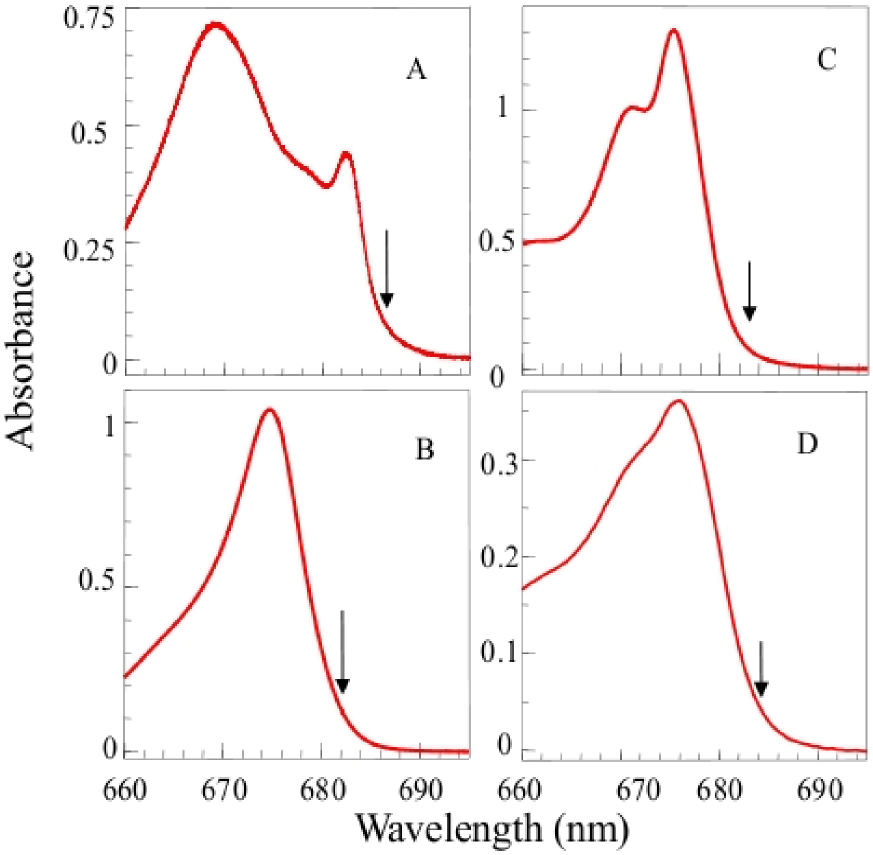

Figure 4.3. The absorption spectra of (A) CP43, (B) CP29, (C) trimeric LHCII, and (D) monomeric LHCII at 5 K. Arrows indicate the wavelengths where HGK experiments were performed.

4.4.2. Hole Growth Kinetics Curves

The next step in our analysis is measuring the HGK at 5 K. HGK curves of CP43 (A), CP29 (B), monomeric LHCII (C), trimeric LHCII (D) and the results of simulation are depicted in Fig. 4.4. The inserts are the high resolution scan of holes at the depth shown by arrows for corresponding complexes.

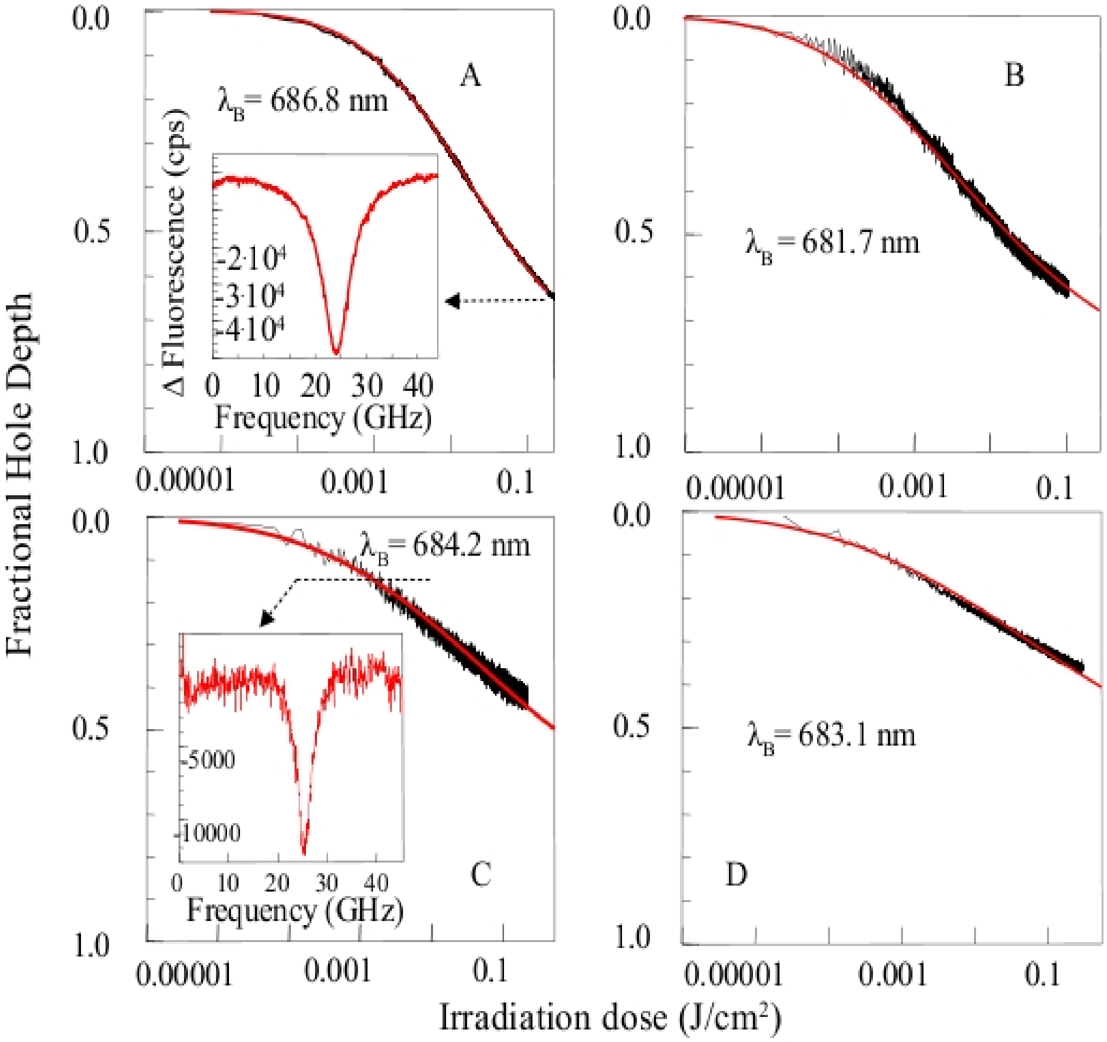

Figure 4.4. HGK curves of, (A) CP43, (B) CP29, (C) monomeric LHCII, and (D) trimeric LHCII at 5 K. Insets are the high resolution hole spectra at the indicated depth by arrow. The burning wavelength (λ_B) is mentioned for each complex.

The results of fitting experimental data for finding the barrier distribution parameters (mean and standard deviation values of tunneling parameter distribution which is related to barrier height through eq. 3.20) in the excited state are summarized in Table 4.1. The results for LH2 [80] are also presented for comparison.

From this table it is clear that all complexes exhibit similar tunneling distribution parameters, possibly indicating the similarity of structural elements involved in small conformational changes / NPHB.

Among these available proteins (in our group), CP43 is the best choice for detailed protein dynamics study for the following reasons: LHCII electron-phonon coupling is too strong (*S* is about 0.8 and 1.3 for monomeric and trimeric LHCII respectively) and ZPL contribute relatively little at any burn wavelength (see Fig. 4.4). Additionally, it is possible that the lowest-energy state of LHCII is delocalized over several pigments [78, and references therein including 101 and 102]. The B800 pigments of LH2 exhibit energy transfer with rates subject to broad distribution [77] [61], [69], making the burning process more complicated. CP29 is to some extent capricious in terms of preparation, also the number of chlorophylls present in that complex is debatable [24], [101]. On the other hand, CP43 has been extensively explored [42], [70], [72], [78], [94], [102] and its electron-phonon coupling parameters are well known. Thus, all other experiments are done on CP43 for the rest of this thesis.

Complex	λ_0	σ_λ	**S**
CP43, A-state [42]	10.2 ± 0.1	1.1 ± 0.1	0.35 ± 0.05
CP29 [78]	10.2 ± 0.2	1.4 ± 0.2	0.65±0.05
LHCII monomer [78]	11.3 ± 0.4	2.0 ± 0.4	0.8±0.05
LHCII trimer [78]	11.2 ± 0.4	2.3 ± 0.4	1.3±0.1
LH2 [77]	10.3 ± 0.2	0.7 ± 0.2	0.45±0.05

Table 4.1. Summary of mean and deviation values of tunneling parameter for different pigment-protein complexes.

4.4.3. Tunneling versus Barrier Hopping

To address the nature of the hole burning process, the dependency of HGK on temperature (form 5 K to 13 K) has been explored for the A-state of CP43. Fig 4.5 depicts the HGK curves (noisy curves) obtained at a burn wavelength of 686.1 ± 0.1 nm (the absorption at 686 nm is dominated by the so-called A-state of the CP43 complex [16], [71]–[73], [79], [102]; at this wavelength, the respective pigment is the lowest-energy one and no downhill excitation energy transfer is expected, see insert in Fig. 4.5) at different temperatures with burn intensities of ~2−12 μW/cm^2. The maximal temperature of this experiment was 13 K, as above 13 K the thermocycling-related recovery clearly becomes important (see below) and straightforward interpretation of the results becomes difficult. The burning process exhibits a slowdown with increasing temperature.

The parameters of the Gaussian λ-distribution obtained from the 5 K curve (λ_0 = 10.2 ± 0.1, σ_λ = 1.1 ± 0.1, with S = 0.35 ± 0.05) are somewhat in disagreement with the results of [78], where we reported a larger value of the tunneling parameter (λ_0 = 11.0). Careful analysis of the details of the experiments in this study and in [78] suggests that too large a reading intensity was employed for CP43 in [78] (but only for CP43, not for CP29 or LHCII, for which a somewhat different setup was used), which could result in a fraction of molecules with the smallest λ being burnt even before the start of the HGK measurement and an increase of λ_0 and decrease of σ_λ obtained from the HGK curve.

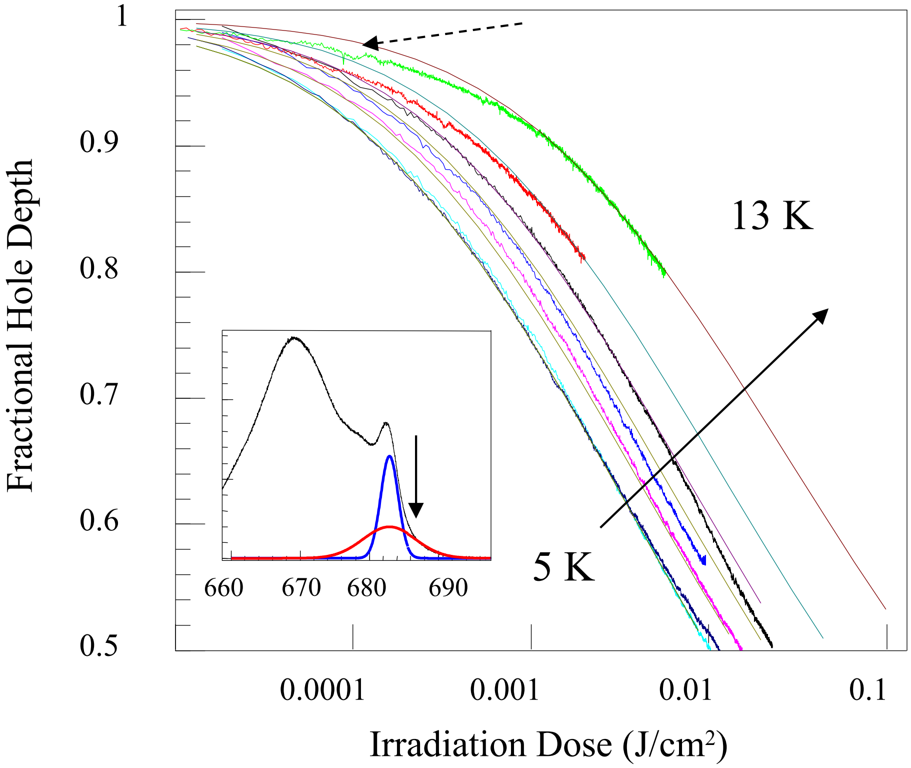

Figure 4.5. HGK curves of CP43 burned at 686.1 nm for 5, 6, 7, 8, 10, and 13 K with fits produced assuming no temperature dependence of the HB yield, and temperature dependence of only the homogeneous line width and S. The dashed arrow indicates the discrepancy between the fit and the 13 K HGK curve at low burning doses. The inset depicts the absorption spectrum of CP43 (black) with the site distribution function of the A- state (red) and the B-state (blue). The down arrow indicates the burn wavelength.

Note that Table 4.1 above contains the corrected value. We have confirmed that burning of ~67% deep zero-phonon holes (ZPH) is possible (i.e., the ZPH is almost at 100% of its theoretically possible depth, given S(T=0) ~ 0.3 and assuming downhill tunneling in the excited state [103]). Fig. 4.5 also contains the results of HGK modeling (smooth curves), which was performed assuming that temperature influences the HGK only via the homogeneous line width [94] and a weak temperature dependence of the Huang−Rhys factor S[1]. The modeling was based on the SHB master equation (eq. 3.16), implying that SHB is due to tunneling (involving the higher-barrier tier, Fig. 3.11.a) .

Homogeneous line widths for several temperatures up to 13 K were measured in this study, most data points are adopted from [94], see Fig. 4.6.

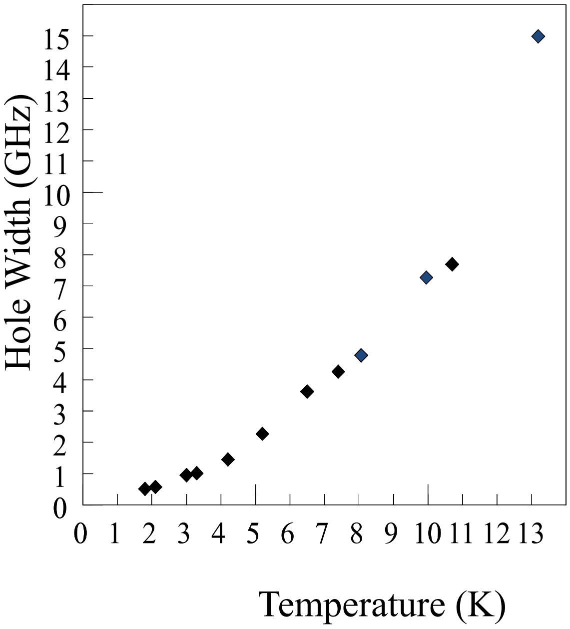

Figure 4.6. The hole width dependence on temperature (remember that the hole width and the homogenous line width are related to each other through eq. 3.25)

---

[1] $S(T) = S(0) \coth(\hbar\omega/2k_BT)$ where $S(0)$ is Huang-Rhys factor at absolute zero and ω is the peak frequency of PSB [27].

The lower-temperature widths were in good agreement with the data from [94] which was limited to below 10 K. The agreement between experimental and modeling results was fairly good (except for the latest stages of the burning process, where the equilibration between HR and HB led to an apparent slowdown of burning), indicating no or very weak temperature dependence of the SHB yield between 5 and 13 K. The dashed arrow indicates that at increased temperatures some small fraction of the systems exhibited somewhat accelerated burning.

The tunneling rate depends on λ as $exp(-2\lambda)$. The hopping rate depends on the barrier height, V, as $exp(-V/kBT)$, and thus, it depends on $\lambda = d(2mV)^{1/2}/\hbar$ as $exp(-\lambda^2\hbar^2/2md^2k_BT)$. The omitted prefactor in both rates is the same attempt frequency Ω_0 on the order of 10^{12} Hz. From this rate representation, one can obtain the upper limit of md^2 for which the initial assumption of our HB model (tunneling in the excited state being the dominant process responsible for NPHB) is still valid. Namely, this is true if

$$2\lambda \ll \lambda^2 \hbar^2 / 2\mathrm{md}^2 k_B T \tag{4.1}$$

or $\lambda^2 \hbar^2 / md^2 k_B T \gg 4$. At T = 5 K, $md^2 < \lambda\hbar / 4k_BT = \lambda \cdot 4.0 \times 10^{-47}$ kg·m^2. At T = 13 K, $md^2 < \lambda \cdot 1.5 \times 10^{-47}$ $kg \cdot m^2$. Fig. 4.7 depicts the dependence of the ratio of the tunneling rate to the hopping rate on λ for $md^2 = 1.0 \times 10^{-46}$ kg·m^2 at 13 K (red solid curve, note the logarithmic vertical scale). Tunneling strongly dominates at all λ, except for the smallest ones, $\lambda < 6.5$. The increase of temperature or of md^2 would shift the curve toward larger λ, meaning that barrier hopping would be dominant for a larger range of λ. The dashed curve in Fig. 4.7 is a Gaussian λ-distribution resulting from the fit to the 5 K HGK data in

Fig. 4.5. Fig. 4.7 demonstrates that, in order for NPHB to be dominated by tunneling, weakly dependent on temperature, for any useful λ ($\lambda \geq 6$), Gaussian λ-distribution, and temperatures up to 13 K, the md^2 has to be less than 1.0×10^{-46} kg·m^2. [Somewhat larger md^2 can be in agreement with tunneling in the case of uniform λ-distribution (dotted lines in Fig. 4.7), but see the discussion on distribution shapes below.] It is clear that, for the situation depicted in Fig. 4.5 at 13 K, a small fraction of systems with excited state $\lambda \leq 6.5$ will experience additional HB via barrier hopping, somewhat accelerating the initial stages of the HB process (which is indeed observed, see dashed arrow in Fig. 4.5) and somewhat decelerating the HR observed with weak light on the sample (indeed observed, see the 13 K curve in Fig. 4.8). Thus, our data can be interpreted as $md^2 = 1.0 \times 10^{-46}$ kg·m^2 being the true value of md^2, rather than its upper limit, although the evidence might be somewhat weak to claim that with full certainty. If the displacement along the generalized coordinate, d, is ~1 Å, the mass of the tunneling entity should be ~1.0×10^{-26} kg, which is significantly smaller than the mass of one carbon atom. Thus, for tunneling to be the dominant HB mechanism with conformational changes involving structural elements as large as protein side groups, displacements along the generalized coordinate should be significantly smaller than 1 Å. A plausible alternative would be proton tunneling. An extended discussion of the structural implications will be provided at the end of Section 4.5.1 [91].

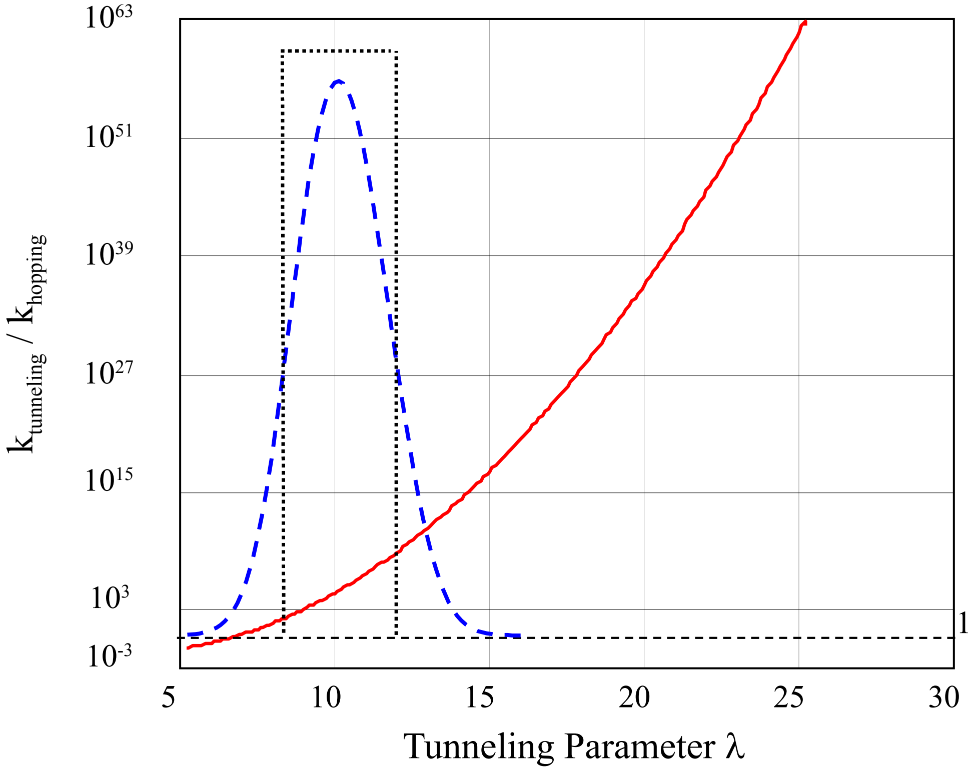

Figure 4.7. Dependence of the ratio of tunneling rate to hopping rate on tunneling parameter λ for $md^2 = 1.0 \times 10^{-46}$ kg·m^2 and T = 13 K, red solid curve. The horizontal dashed line corresponds to ratio = 1; the ratio is ~3 for $\lambda = 7.0$. The full excited state λ-distributions (Gaussian, blue dashed line; uniform, black dotted line) are added for comparison.

4.4.4. Hole Recovery

Recovery of a hole at the burn temperature yields the tunneling distribution parameters in the ground state. Spontaneous recovery has been observed either by performing high resolution scan of a hole and calculating its area or by continuously measuring the hole depth. The latter is done by decreasing the burn intensity to reading intensity at the same wavelength (the increase in fluorescence signal means hole recovery)[1].

Fig. 4.8.A depicts the 5 K recovery of the holes (relative area vs. time) of different initial fractional depths burned at 686.1 ± 0.1 nm. It is clear that the rate of recovery is dependent on the fractional depth of the hole originally burned. A larger fraction of the shallower holes is recovered within the same time interval than for the more saturated holes. The holes also experience weak broadening. Note that performing the laser scan takes some time, and therefore, the first hole in the series was measured approximately three minutes after the end of burning. Nevertheless, the fractional depths obtained from the first post-burn spectra and from the HGK curves were fairly consistent, within ~1%.

---

[1] This technique is more reliable specially in the very beginning of recovery where hole recovers quickly. In practice switching between burn intensity and reading intensity is done using a motorized filter flipper.

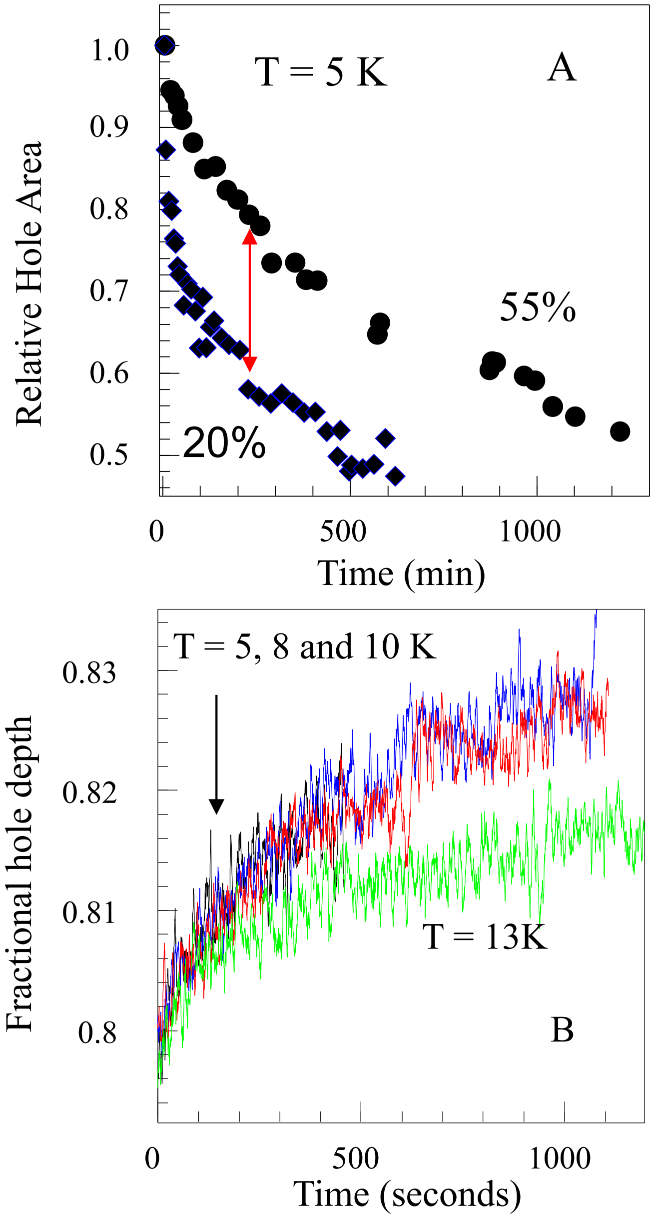

Figure 4.8. (A) Recovery of the holes (λ_B = 686 nm) at 5 K. Circles, originally a 55% deep hole; diamonds, originally a 21% deep hole. The data was obtained by measuring the hole spectra and determining the hole areas via a fit. The red arrow corresponds to an 18% difference in the recovery data sets, and this difference was achieved in about the first 3 h, while the holes were still at 78 and 60% of their original areas, respectively. See Fig. 4.11 for more details. (B) Recovery of 20% holes at ~686.1 nm, monitored as the hole depth (fluorescence signal) versus time. Both burning and recovery for each hole were measured at the same temperature. These recovery curves belong to the respective holes found in Fig. 4.5.

Fig. 4.8.B contains hole-recovery data obtained by monitoring the fluorescence signal (i.e., hole depth rather than area) at fixed λ_B ~ 686 nm, and utilizing the same light intensity as was employed while measuring the hole spectra (~40 nW/cm^2), at several temperatures. The data for the ~20%-deep holes was collected immediately after measuring the respective HGK (a motorized filter flipper was employed, see Fig. 4.10).

The holes experienced relatively slow recovery, with 1.4% (of the preburn absorption; 7% of the original 20% hole) recovering in the first 180 s (solid arrow, the approximate time between the end of the HGK measurement and the hole spectrum measured for the first time in other experiments).

After the initial phase of measurements depicted in Fig. 4.8.B, the sample was left in the dark for several minutes. Subsequent segments of the recovery curves as shown in Fig. 4.10 were located on the smooth line defined as a further-extrapolated fit to initial recovery, which indicated that periodically monitoring the recovery with the reading intensity has a small, if any, effect on the recovery rate. Interestingly, the recovery of the hole observed in this mode did not depend on the temperature up to 10 K but did become slower at 13 K. The latter effect may be due to the increase of the efficiency of HB by reading-intensity light (competing with recovery). This increase in HB yield may be attributed to the onset of excited-state barrier hopping (for the smallest-λ systems in the ensemble) in addition to tunneling. (See Section 4.4.3 and Fig. 4.7 for additional details.) We also noticed that performing SHB experiments in the neighboring wavelength ranges resulted in somewhat faster recovery of a given hole. Qualitatively, this indicates that a fraction of NPHB photoproduct (antihole) was redistributed within several cm^{-1} from the original hole, and that a low-λ fraction of this antihole could be returned to the original wavelength via light-induced hole filling (LIHF). Although this is not immediately obvious from Fig. 4.8. A and B, as one of them depicts evolution of hole area while the other depicts evolution of hole depth, the data in frames A and B are in disagreement. Namely, when monitored at a fixed (burn) wavelength, the 20% hole recovered significantly slower than suggested by the data shown in Fig. 4.8.A (see blue diamonds). The most likely reason for this disagreement is, again, LIHF, caused by the measurement (i.e., scanning of the HB spectra). In this scenario, the shallower (20%) hole would be more affected by LIHF, since its antihole would be dominated by lower values of λ (or barrier height).

Fig. 4.9 compares the hole-depth dependence on the recovery time for holes monitored at a fixed burn wavelength (black curve a, hole 55% deep right after burning; blue curve b, 20%), and holes monitored via scanning whole spectra (green (c), red (d); same holes as in Fig. 4.8.A). Note that, in the fixed-wavelength experiments, the sample was not exposed to light continuously but just for short periods of time (except for the very beginnings of the curves). Thus, possible prevention of HR by the measuring light has been minimized. It is clear that the differences between the hole-depth data obtained in the two types of recovery experiments are significant, and one must conclude that the data in Fig. 4.8.A is significantly affected by LIHF. Therefore, the data obtained via direct hole depth monitoring, as shown in Fig. 4.9 (black, blue), rather than data on hole areas (see Fig 4.9; red, green and Fig. 4.8.A), will be modeled to obtain distribution shapes and parameters, as discussed below. It should be mentioned that the beginning of recovery (the first ~200 seconds) has been reported without any averaging, except it was normalized, however, for subsequent points (see the insert in Fig. 4.10.A), the averages over multiple (~40) raw data points (i.e. Fig. 4.10.B) have been calculated. This explains the noisier graph in the beginning and smother one for the rest.

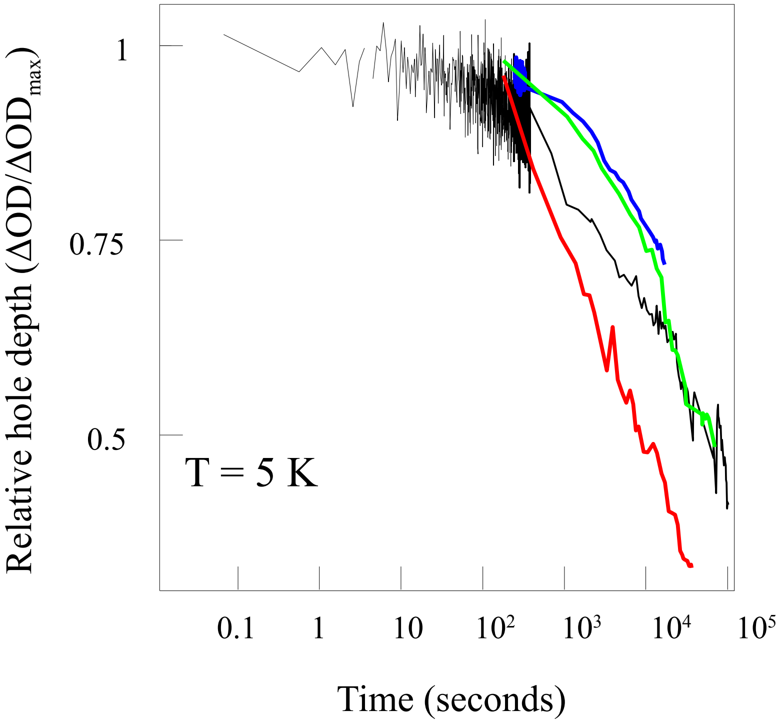

Figure 4.9. Recovery of the holes of different initial fractional depths measured either while keeping the laser at a fixed burn wavelength (using read intensity) or by scanning the hole spectra. Black dots (a): initially 55% hole, recovery monitored at fixed (burn) wavelength; blue dots (b): initially 20% hole, fixed wavelength; green dots (c): initially 55% hole, scanning; red dots (d): initially 20% hole, scanning.

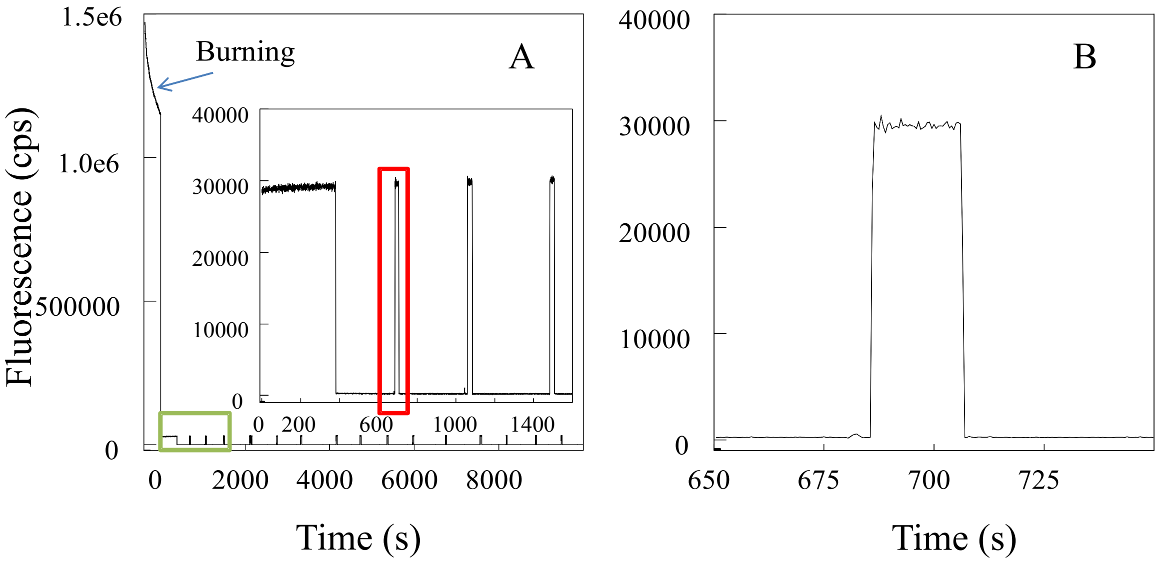

Figure 4.10. (A) Recovery of a 21% deep hole right after burning. Three segments after burning and initial immediate recovery are shown in the insert. (B) The segment highlighted in red in frame A is enlarged to demonstrate the noise level and to prove that reading intensity does not obvious effect in recovery.

To address the error in the subsequent Figure 4.12, it should be noted that in the Figure 4.10 the background signal was ~250 and zero time is placed at the end of burn / beginning of recovery. The fractional hole depth has been estimated based on HGK: ~21%. Then the signal which would be present in the absence of hole was determined (36300) from the above percentage and the signal in the very beginning of recovery (28500 ± 100).The beginning of recovery has been reported without any averaging, except it was normalized as (36300-signal(t))/(36300-28500), so the result starts from one and decreases in the following figures, Figs 4.9 and 4.11. Since 36300 and 28500 are not independent, we estimate error of the final result based on the formula for the error of the ratio of two independent variables. Everything else will contribute to systematic error, not to the error bars. Then δ recovery/recovery=0.01 for 68% confidence interval. Or, if we choose better confidence interval, δ recovery/recovery=0.02. As recovery curve is normalized in the 1 to 0 range, the error is of the order of 2%, meaning that datapoints in Figure 4.10 are of the size appropriate for error bars. The main source of errors is slow drift of the sample with respect to the probing beam.

As mentioned in the Introduction to this section, the shape of the barrier height or λ-distribution is a subject of debate. In order to resolve this issue, we will attempt to model our data within both Gaussian (characterized by mean λ_0 and STD σ_λ) and uniform (or, more precisely, rectangular; constant probability between λ_{min} and λ_{max} [38], [80]) λ-distribution frameworks, assuming the existence of a correlation between the shapes of the protein energy landscapes (magnitudes of the relevant energy barriers) in the ground and excited states of the CP43 pigment−protein system. We will also make the assumption that the mass of the tunneling entity, *m*, and the displacement along the generalized coordinate, *d*, are the same in both the ground and excited states, and that the only difference between the ground and excited state barriers is in the magnitudes of the barrier heights. This is equivalent to requiring that, as depicted in Fig. 3.10, the minima of the ground-state landscape are located below the minima of the excited-state landscape.

It is important to recognize that the HGK experiments, with the irradiation dose (P·t in eq. 3.16) changing over several orders of magnitude, and with the holes eventually reaching saturation, yield the whole distribution of barriers (more precisely, the tunneling parameter, λ) in the excited state. Holes of various non-saturated depths, however, represent only a fraction of the original λ- (or barrier) distribution. Obviously, the subset of pigments experiencing the smallest barriers (smallest λ) undergoes NPHB first, while, for shallow enough holes, the pigments with large λ remain mostly unaffected and do not contribute to the hole spectra.

The HB simulation software previously used in [77] and [78] as well as for modeling the HGK curves in Fig. 4.5 has been modified to save and automatically analyze separate contributions to the spectral hole obtained for different values of λ. Contributions to the hole spectrum described in full by eq. 3.16 were calculated separately for every λ for several fractional depths of the (total) hole, and respective contributions to the total resonant hole (ZPH) area and depth were determined. Fig. 4.11 depicts partial excited-state λ-distributions, which actually contribute to the holes of the fractional depths of 20 and 55% for the Gaussian and uniform λ-distributions. The areas under the curves, which are proportional to the hole areas, were renormalized to 1 for clarity. The modeling parameters correspond to burning at 686 nm into the (lowest-energy) A-state of CP43 (with the SDF peaking at 683 nm and an inhomogeneous width of 180 cm^{-1} [71], [72], [94]).

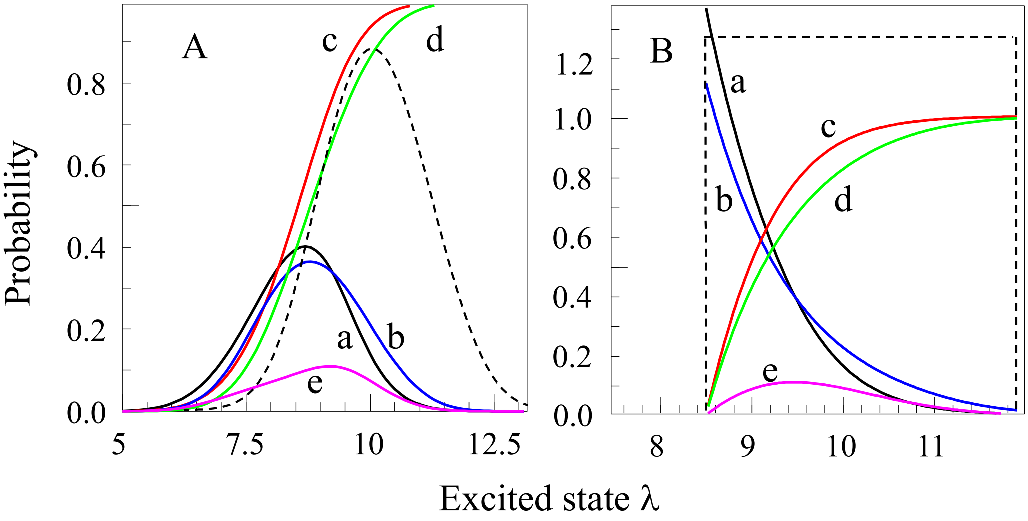

Figure 4.11. (A) Calculated excited-state partial λ-distributions for Gaussian true full λ-distributions (black: 20% deep hole, a; blue: 55% deep hole, b). Areas under curves are normalized to 1. The red (c) and green (d) curves are integrals of the black and blue curves, respectively. The magenta curve (e) is the difference between these integrals. It reaches a maximum of ~12% when the holes are ~70% recovered. The dashed curve is the true full λ-distribution. (B) Same starting from the uniform λ-distribution. Again, the maximal discrepancy between the expected 20 and 55% HR curves is 12%, which is reached gradually by the time holes are 70% recovered.

The full λ-distribution parameters for both shapes of the distribution were obtained from the best fit to the saturated 5 K HGK curve reported in Fig. 4.5. For a full, true Gaussian λ-distribution, λ_0 is 10.2 ± 0.1 and σ_λ is 1.1 ± 0.1, with $S = 0.35 \pm 0.05$. The latter value is in agreement with the earlier SHB data, [70]–[72], [78], [94], [102] including the fitting of the whole SHB spectra [73], [102], not just the HGK. For a uniform λ-distribution, a quite satisfactory fit to the HGK curve can be obtained for $\lambda_{min} = 8.5 \pm 0.1$ and $\lambda_{max} = 11.9 \pm 0.1$.

In the case that we start from the Gaussian λ-distribution, the partial distributions actually contributing to the holes resemble Gaussian curves (frame A of Fig. 4.11), although the agreement is not perfect (low-λ tail somewhat extended; high-λ tail a bit steeper than for a Gaussian). $\lambda_0' = 8.60$ and $\sigma_\lambda' = 0.99$ were obtained for a 20% hole, and $\lambda_0' = 8.84$ and $\sigma_\lambda' = 1.08$ were obtained for a 55% hole via Gaussian fits. However, the shape of the partial λ-distribution in the case where the full λ-distribution is uniform (between λ_{min} and λ_{max}) is highly asymmetrical (see frame B of Fig. 4.11). The partial distributions for holes of 20 and 55% initial fractional depths are shown as solid black (a) and blue (b) curves, respectively; full distributions are shown with dashed lines. Also presented in Fig. 4.11 are the respective cumulative distributions (red and green curves c and d, i.e., integrals of the partial distribution curves) and their differences (e, magenta curves). For both types of distributions, the difference reaches a maximum value of about 12% by the time the holes are roughly 70% recovered. This is in clear disagreement with the results in Fig. 4.8, where an 18% difference between the recovery curves for 20 and 55% holes was achieved early in the process of recovery. The disagreement is attributed to LIHF.

The smallest-barrier fraction of the excited-state λ-distribution (see Fig. 4.11) corresponds to the smallest barrier fraction of the ground-state distribution. It is clear that, if tunneling is the dominant process behind NPHB at 5 K, it also would be an overwhelmingly dominant process behind HR in the ground state, where λ and V are larger (see Fig. 4.7). The modified expression of Love et al. [63] for the fraction of systems not recovered after time τ, which includes both tunneling and barrier hopping rates, was given as eq. 3.31. One can easily calculate numerically the λ-(sub)distributions, areas, and depths of the holes remaining after any time interval at any temperature by multiplying the postburn fractional λ-distributions by the $q(\lambda,\tau,T)$ curves (eq. 3.31). As described above, we have reasons to believe that the area recovery data presented in Fig. 4.8.A is affected by LIHF. Thus, parameters of the ground state λ sub-distributions determining the 5 K HR could be more reliably obtained from an analysis of the hole depths, rather than the hole areas. Note that our model does not take into account spectral-diffusion broadening [61], [65]. Therefore, the actual decrease of the hole depth, not affected by LIHF, should be equal to or slightly faster than the depth decrease following from our model.

Fig. 4.12 depicts results of hole-depth recovery modeling based on a Gaussian (solid red curve) or a uniform (dashed blue curve) original full λ-distribution[1]. It is immediately clear that, due to highly asymmetrical partial-distribution shapes (see Fig. 4.11.B), the uniform λ -distribution model predicts HR behavior, which is qualitatively different from that observed in the experiment. On the other hand, in the Gaussian λ-distribution model, one can successfully fit recovery of shallow holes, starting with the same set of parameters. For deeper holes the experimental results are between the two theoretical curves (not shown) which may or may not be related to the fact that Gaussian distribution of V does not give exactly Gaussian distribution of λ, and vice versa. The excited-state partial distributions depicted in Fig. 4.11.A have been stretched/ rescaled by the same factor $k = \lambda_{ground} / \lambda_{excited} = 2.25$ to yield the respective ground-state λ-distributions. This

---

[1] The experimental data of this figure is the same as black curve in Fig. 4.9.

factor is in reasonable agreement with the results obtained by Reinot et al. for glasses [49], [76].

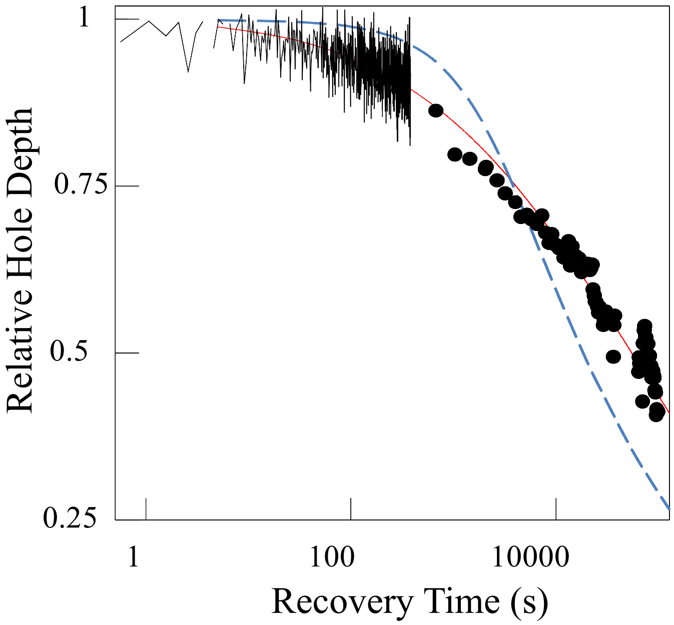

Figure. 4.12. Comparing the results of fitting hole-depth recovery data using Gaussian (solid red curve) or a uniform (dashed blue curve) original full λ-distribution. The discrepancy of the latter model is obvious in this 21% hole.

Another interesting conclusion of the partial distribution model presented here is that in the absence of small-tier spectral diffusion, the holes should narrow upon recovery. The smallest-lambda contributions to the holes are a) most saturation-broadened and b) recover first. An example (the result of simulation) is presented in Fig. 4.13. Thus, the effect is quite significant and should be taken into account when performing hole broadening (with time) experiments.

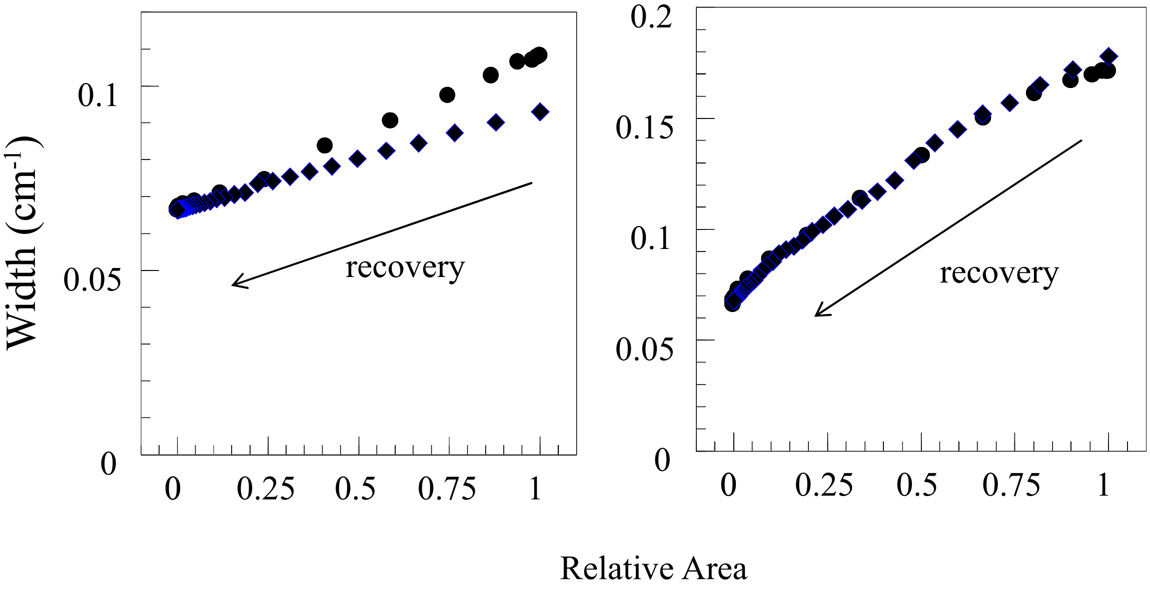

Figure. 4.13. Recovery simulation of a 50% hole by considering the partial λ-distribution model which shows hole narrowing upon recovery. black: Gaussian lambda distribution, blue: uniform lambda distribution

The recovery of an initially 37% hole is investigated in Fig. 4.14, both at burn temperature and upon thermocycling. First the sample was given ~3 h to be recovered at 5 K before the thermocycling was started. This ensured that the smallest barrier fraction of the hole had recovered, either spontaneously or via LIHF, and one could meaningfully follow the recovery upon thermocycling by monitoring the hole area rather than the depth. The latter would not be very informative here, since spectral holes are known to broaden rapidly upon thermocycling [60], [65], [104]. That said, one can note that, for the first 3 h, recovery of the 37% hole lays between the 20 and 55% depth data sets of Fig. 4.8.A. The hole broadened quickly upon thermocycling, which resulted in large uncertainties in the area of the hole for cycling temperatures over 40 K. The triangles in

Fig. 4.14. indicate the expected HR at 5 K, based on respective partial λ-distributions, similar to that in Fig. 4.11.A, for 37% deep hole and $md^2 = 1.0 \times 10^{-46}$ kg·m².

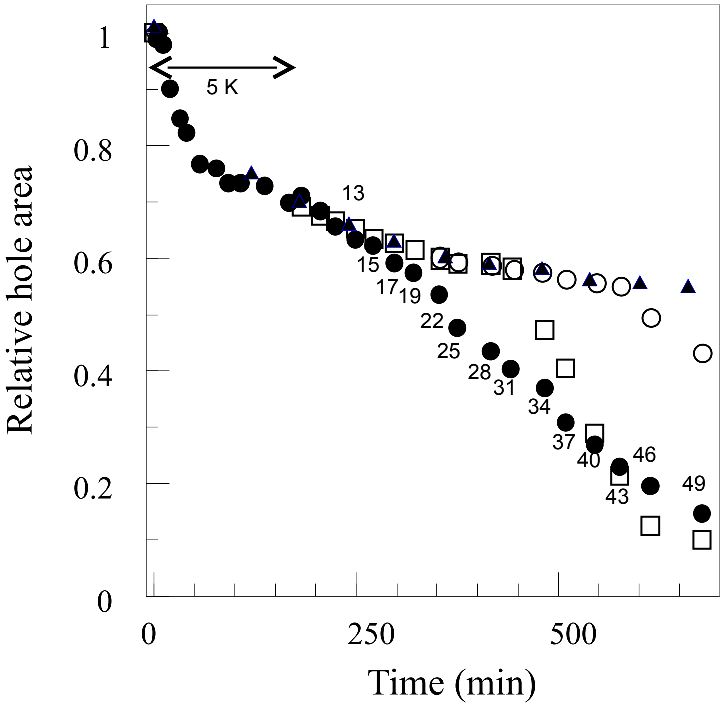

Figure. 4.14. Recovery of the 37% hole at 5 K (first 3 hours) and then as a result of thermocycling (circles). Numbers next to the data points denote maximal cycle temperature in K. Closed triangles represent the recovery expected at 5 K. Open circles represent the recovery expected upon thermocycling for $md^2 = 1.0 \times 10^{-46}$ kg·m² and downhill tunneling only. Open squares represent the recovery expected upon thermocycling for $md^2 = 1.4 \times 10^{-46}$ kg·m².

It can be seen that, up to about 13 K, the actual recovery of the hole was determined by the elapsed time, and not the cycling temperature.

The expected hole filling is calculated based on the partial ground state *λ* distribution[1], black curve in Fig. 4.15, encoded into a hole with 37% fractional depth[2].

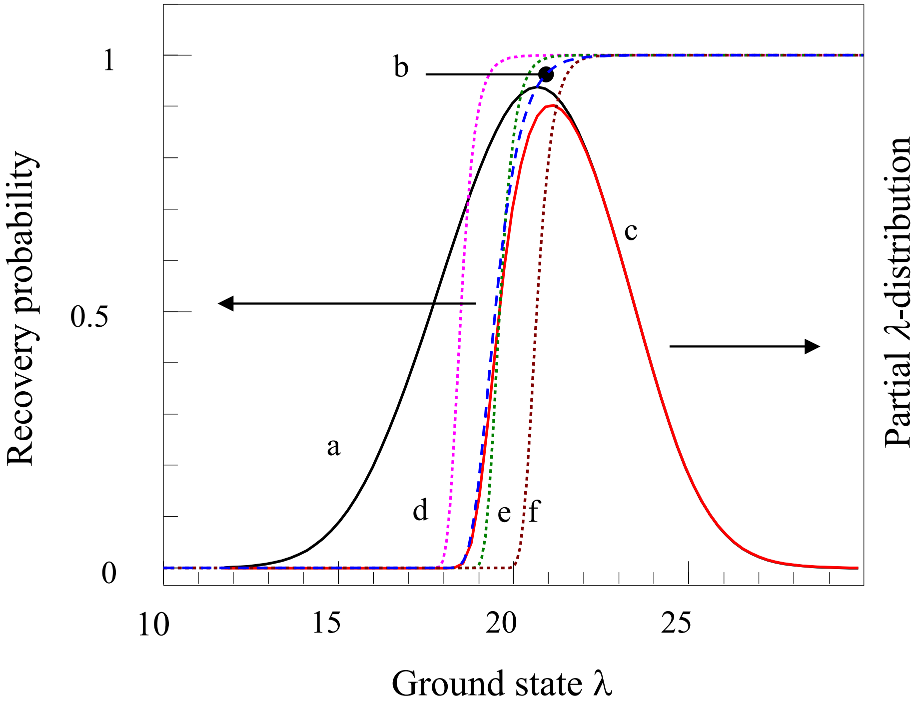

Figure. 4.15. Black (curve a): partial ground-state λ-distribution corresponding to the hole of 37% initial fractional depth, obtained with the same parameters as the curves in Figs. 2.5.A and 4.14. Dashed blue (curve b): the q-curve obtained with eq. 4.2 which corresponds to 35% recovery of the initial hole. Red curve (c): illustration of the partial distribution remaining after the hole is 35% recovered; it is a product of the black and blue curves. Magenta (curve d): q-curve (eq. 3.31) for thermocycling to any temperature up to 40 K, t = 60 s, $md^2 = 1.0 \times 10^{-46}$ kg·m^2. Green (e): thermocycling up to 45 K. Brown (f): thermocycling up to 50 K.

The q-curve based on eq. 3.31 is shown in blue (curve b), and it was produced assuming that T is the same as burn temperature (~5 K) and t is the time which sample is

---

[1] This is partial since the hole is not saturated.

[2] This curve is obtained from HGK experiment which gives partial λ distribution in the excited state and then proportionally adopted for the ground state (by considering the fact that $\lambda_{ground}/\lambda_{exc} = 2.35$)

left at burn temperature (i.e. ~3 hours). Multiplying q-curve with post-burn partial λ distribution gives the red solid curve (c), representing the partial distribution remaining after that initial recovery, i.e., present at the beginning of thermocycling. The area under the red curve is 65% of the area under the black curve. One can follow the same logic using ever-increasing recovery times at fixed temperature, and simulate further hole recovery at 5 K, solid triangles in Fig. 4.14. After the first three hours the recovery becomes very slow and one may need couple of days to see the measurable recovery, so we started thermocycling. To model the thermocycling new q-curves should be produced according to temperature change profile and they are consecutively multiplied by previous λ distribution as follows:

$$g(\lambda)_{new}=g(\lambda)_{previous}\prod_{T,t(T)} q(\lambda, T, t(T)) \tag{4.2}$$

where t (T) is waiting time at temperature T. The dotted magenta curve (d) in Fig. 4.15 is obtained for τ = 60 s, $md^2 = 1.0 \times 10^{-46}$ kg·m^2, and T = 40 K. It is still located at significantly smaller λ values than the red curve (c). Thus, for $md^2 = 1.0 \times 10^{-46}$ kg·m^2, the recovery upon thermocycling should be indistinguishable from the recovery at 5 K for cycling temperatures up to about 40 K (see open circles in Fig. 4.14). On the other hand, the dotted green (e) and brown (f) q-curves correspond to cycling to 45 and 50 K, respectively. Since these curves intersect the red curve (c) or are located to the right of it, significant recovery is expected upon cycling to these temperatures.

The calculated data points in Fig. 4.14 were obtained taking into account the entire actual temperature change profile. The difference between experimental and modeling results indicates the presence of an additional recovery mechanism, with respect to burnt molecules returning to their original frequencies. More details will be provided in Section 4.5. Interestingly, the above analysis of the thermocycling results provides the same upper limit of $md^2 = 1.4 \times 10^{-46}$ kg·m^2, as suggested based on HB behavior. Consider instead, for example, the recovery expected upon thermocycling for $md^2 = 1.0 \times 10^{-46}$ kg·m^2 (open squares). The situation when experimental data and the results of simulations first diverge and then converge (at around 40 K) is unphysical. This scenario would imply that the recovery due to the additional mechanism mentioned above has been reversed. In other words, the derivative of the difference between experimental results and those of simulations would not yield a meaningful barrier distribution.

The difference between the hole area as a result of thermocycling (closed circles in Fig. 4.14) and the hole area based on modeling for 5 K (triangles) is presented in Fig. 4.16. Up to 40 K the system with $md^2<1.0\text{x}10^{-46}$ kg·m^2 will behave in the same way anyway. Although the derivative of the fit to the data in Fig 4.14 (dashed red line) is not perfectly Gaussian, it is clearly far from $1/\sqrt{V}$. The midpoint of the dependence of the hole area on the cycling temperature is located at approximately 36 K, which with typical $ln(\Omega_0\tau_T)$ ~ 30 [59], [63] (where a τ_T value of ~60 s is time spent at the highest temperature of the cycle) corresponds to an average ground-state barrier height of $k_BT\cdot ln(\Omega_0\tau_T)$ ~ 920 cm^{-1}. With a ground-state λ_0 of >20, this would result in a $md^2 > 1.5 \times 10^{-46}$ kg·m^2. This is larger than the upper limit determined above, indicating likely involvement of another landscape tier.

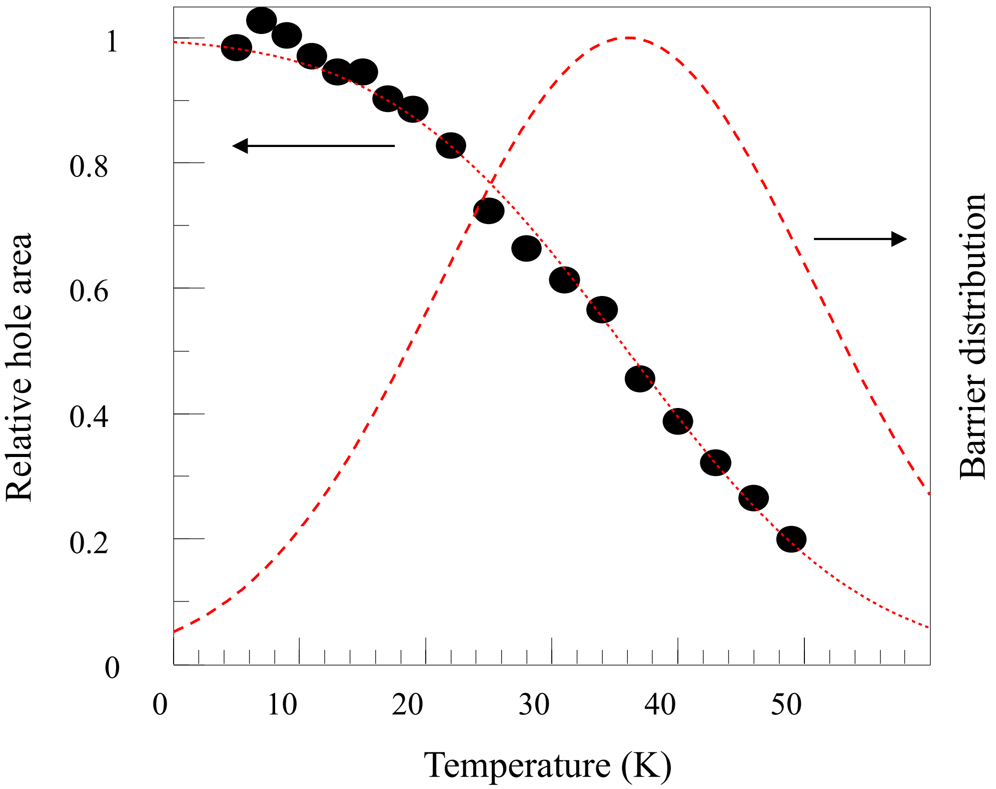

Figure. 4.16. Relative hole area versus cycle maximal temperature. The area of the hole after the first ~3 h of recovery at 5 K is taken as 100%. The data has been corrected for recovery, which would occur anyway at 5 K (triangles in Fig. 4.14). The data set yields a Gaussian barrier distribution with a mean of 36 K and a fwhm of 35 K (dashed line).

4.5. Discussion

4.5.1. HB Mechanism: Tunneling versus Barrier Hopping

As stated in the Introduction, according to refs [44] and [45], the NPHB mechanism is based on tunneling in the excited state of the pigment/protein system (see Fig. 3.12). In Section 4.4.3, we obtained the upper limit of 1.0 × 10^{-46} kg·m^2 for md^2, assuming that weakly temperature dependent tunneling [49] is indeed the dominant HB mechanism up to 13 K. A significantly larger value of md^2 was reported in [104] for phycobiliprotein, which would require barrier hopping to dominate at much lower temperature (see Fig. 4.7). To confirm the dominance of tunneling as the HB mechanism in our experiments, we must consider if excited-state barrier hopping could be an alternative mechanism behind the HB process. If excited-state barrier hopping were the dominant NPHB mechanism, the HB yield in eq. 3.17 would have to be modified[1]:

$$\phi(V, T_1) = \frac{\Omega_0 \exp(-V/K_B T)}{\Omega_0 \exp(-V/K_B T) + \tau_1^{-1}} \tag{4.3}$$

Obviously, in the case of a Gaussian barrier height V distribution, the resulting HGK curves and partial barrier distributions will qualitatively resemble those obtained for the Gaussian λ-distribution. The main problem with allowing barrier hopping to dominate in the excited state is that the HB yield would be much more strongly dependent on temperature than in the case of tunneling. With $\lambda \sim 10$ and $md^2 \sim 10^{-46}$ kg·m^2, the excited state barrier heights would have to be of the order of 100-200 cm^{-1}. However, changing the burn temperature, T, from 5.0 to 13.0 K, as in Fig. 4.5, would result in a drastic (several orders of magnitude) increase of the HB yield, which is clearly not observed experimentally. Furthermore, the temperature-dependent HGK in Fig. 4.5 exhibits deceleration of HB rather than acceleration with increasing temperature. These results can be quantitatively explained by just increasing the homogeneous line width [94] and phonon Huang−Rhys factor, S, with temperature without any change in the HB yield, in

---

[1] τ_1 is the fluorescence life time.

agreement with the tunneling hypothesis, with the respective rate being only very weakly dependent on temperature [76].

One could still point out that the HR starts right after the start of burning (this could be the most likely reason for the small discrepancies between experimental and theoretical curves in Fig. 4.5) and ask if, in the case of barrier hopping in the excited state, the HB and recovery rates could be changing with temperature in a concerted fashion, still yielding the results depicted in Fig. 4.5. Given that the barriers in the ground state have to be significantly higher than in the excited state, and taking into account the exponential dependence of the hopping rate on barrier height, V, near-perfect mutual compensation of changes in the burning and recovery yields in the 5−13 K range is obviously impossible; the recovery rate, while smaller than the burn rate, will change with temperature orders of magnitude faster than the burning rate. A scenario in which barrier hopping is the dominant process in the excited state while tunneling is the dominant process in the ground state (md^2 only slightly larger than the upper limit derived in Section 4.4.3) is also not feasible. In this case, the recovery rate would change too little with temperature, compared to the burning rate. Summarizing, barrier hopping is unlikely to contribute to SHB up to 12 K in CP43.

We also note that the Bogner−Schwartz NPHB mechanism [105] involving ground-state barrier hopping utilizing energy locally dissipated in the electronic transition via phonons and vibrations, is quite unlikely, since it would lead to independence of the NPHB yield on the excited state lifetime. This would contradict the observed dependence of the NPHB yield on wavelength within the B800 band in the LH2 complex [77]. Additionally, positive correlation between the NPHB yield and electron phonon coupling, *S* (i.e., negative correlation between λ_0 and *S*), would be expected for the Bogner−Schwartz NPHB mechanism. However, this contradicts the results presented in [78] and Section 4.4 above, where the LHCII trimer exhibited both the highest *S* and highest λ_0 among the complexes studied. Additionally, the LHCII monomer exhibited the same λ_0 as the LHCII trimer but a significantly lower *S*.

The nature of the tunneling entities could be suggested on the basis of the md^2 value. Above, we presented some evidence that 1.0×10^{-46} kg·m^2 is the true value of the md^2 rather than just its upper limit. In this case, if the tunneling involved a proton, the respective distance, *d*, would be 2.45 Å, which is a typical hydrogen bond length. On the other hand, it is known that in the scenarios involving tunneling within a sufficiently long hydrogen bond yielding double-well potentials, the value of *d* is several times smaller than the hydrogen bond length [106] and [107]. Here it is worth mentioning that tunneling involving significant rearrangement of the C═O···H hydrogen bonds between protein and chlorophyll has been proposed as a “photoconversion-HB” mechanism in CP43 [72], [102] (but mainly for the B- state) to explain changes in the absorption spectrum occurring very far away from the original hole. However, it was recently demonstrated that this apparent large shift of antihole absorption can be explained with small site energy shifts, resulting in changes in the whole picture of excitonic interactions and redistribution of oscillator strengths [71]. Moreover, the presence of significant LIHF in our experiments, involving a relatively narrow scanning range, speaks against too large a shift in pigment site energies upon HB. If spectral shifts were large, illuminating the sample just a few cm^{-1} from the original hole would not cause any hole filling.

For a methyl group, $md^2 = 1.0 \times 10^{-46}$ kg·m^2 would result in $d = 0.37$ Å. With respect to the latter possibility, we need to stress that we did not observe any evidence of "population hole burning" related to rotational tunneling of the methyl groups [108]–[110]. There were no sharp anti-holes appearing or disappearing within the 45 GHz scan range centered on the original hole (or within ~120 GHz for broader, more saturated holes). Note that the sharp anti-hole effect has been observed for small chromophores, e.g., dimethyl-s-tetrazine and p-chlorotoluene, with the methyl group directly attached to the ring. The reduced coupling of the relevant methyl group to the chlorophyll π-electrons expected in our system must result in poorly resolved hole and anti-holes nearly canceling each other in the case where HB is limited to rotational tunneling. On the other hand, a 120° rotation of a C_3-symmetrical methyl group is not expected to cause large shifts in absorption frequency of nearby pigments by purely electrostatic effects. Thus, although rotational tunneling of methyl groups may occur in CP43, the HB mechanism must be based on a different effect. Other interesting alternatives, especially in the case where the true md^2 is less than 1.0×10^{-46} kg·m^2, include hindered rotation of a hydroxyl group (the mass of the hydroxyl group is close to that of the methyl group) and tunneling within a hydrogen bond. However, it is not clear which particular hydrogen bonds might be involved in the latter process. One cannot also exclude concerted small motions of several groups of atoms.

4.5.2. Barrier and/or λ-Distribution Shapes

First, we must point out that the existence of dependence of the hole recovery on the fractional depth of the original hole in Figs. 4.8.A and 4.9 is a clear indication that CP43 manifests a significant degree of spectral memory [49]. This means that holes recover mostly as a result of the previously burnt molecules returning to ω_B. This assumption was implicitly behind the idea that the recovery is governed by the hole-depth-dependent partial λ-distributions (Fig. 4.11); here, we provide justification. In the case of no spectral memory whatsoever, any molecule would be as likely to participate in the recovery of the hole as the molecules initially absorbing at ω_B and burnt away in the process of HB. This, however, would mean that a hole of any depth would recover according to the same full ground state barrier height or λ-distribution, and there would be no difference in the recovery of shallow and nearly saturated holes. The high degree of spectral memory should not be understood as literally as in [49] and [76], where each pigment could assume only two spectral positions. Notably, modeling of HB and HR on a 20- well energy landscape (Najafi et al., in preparation, Chapter 5) yields results similar to those in Figs. 4.8 and 4.9. This can be understood if one notices that, as long as the number of available conformational substates is limited, many individual pigment/protein systems will not possess a well which is resonant with ω_B. Thus, memory-less recovery (as proposed to explain part of the thermocycling results below) can contribute to only a fraction of the hole recovery. The limited (but exceeding two) number of available conformational substates in CP43 is in qualitative agreement with the SPCS results on the LH2 complex [81], [83].

It is obvious that, for a uniform full λ-distribution with highly asymmetrical partial λ-distributions (Fig. 4.11.B), the partial distributions of the ground state barrier heights, V, are expected to be even more asymmetrical, and deviate significantly (i.e., decrease much more steeply with increasing V) from $\sim 1/\sqrt{V}$. We note that, in many papers devoted to hole thermocycling studies of the barrier distributions in proteins, the fractional depth or the degree of saturation of the holes being thermocycled was not specified. Therefore, it is hard to tell how far the partial distributions probed by the authors of these works were from true full barrier distributions. More importantly, the holes were often thermocycled right after burning, sometimes without proper correction for spontaneous recovery. (Love et al. in their work on $Ba_{1-x-y}La_xTb_yF_{2+x+y}$ recognized the importance of disentangling the recovery at a fixed-burn temperature from recovery resulting from thermocycling [66], but in protein studies the issue was not always addressed sufficiently.) It may well be that thermocycling without correction yielded results which were a superposition of the dependencies presented in Figs. 4.8 and 4.14 and that could be reasonably well fitted to a superposition of a Gaussian and $\sim 1/\sqrt{V}$ distributions just by coincidence. A crucially important point here is that the line of reasoning yielding partial distribution shapes is not protein-specific, and it applies to NPHB in any kind of amorphous material, including glasses and polymers. In fact, we derived them from the model which is still to a large extent TLS-based, apart from the anti-hole treatment. Thus, fitting any HR or thermocycling results, including those obtained in glasses, with $\sim 1/\sqrt{V}$ does not appear to be sufficiently justified from a theoretical standpoint. As stated above, introduction of partial barrier- or λ-distributions is justified by the presence of spectral memory. In polymer ([111] and [112]) and *p*-terphenyl ([88]) glasses, single molecule spectral lines exhibited jumps between a small number of wavelengths, consistent with the model where the pigment is interacting with a small number of TLS (see Fig. 3.12). In such cases, a burnt molecule is likely to return to its original wavelength as a result of HR, i.e. there is nearly perfect spectral memory. Interestingly, in toluene glass, additional slow drifts and unreproducible jumps were observed [112]. However, slow drifts would contribute mainly to hole broadening in HR experiments, and therefore for the purpose of our discussion centered on hole area or depth variations, toluene glass still would be a system with a fair degree of spectral memory. HB and HR experiments on glasses, analogous to those described here for CP43, need to be performed to further test these ideas.

One could also note that, with $V \sim \lambda^2$, the Gaussian distribution of the tunneling parameter does not translate into a Gaussian distribution of barrier heights. Roughly, the Gaussian distribution of λ results in an asymmetrical, noncentral, chi-square distribution for V. Conversely, the Gaussian distribution of V translates into an asymmetrical distribution of λ, which is the product of a Gaussian and a term linear in λ. (One can arrive at these results using the Leibnitz integral rule.) However, for the parameters reported here (i.e., for relatively small σ_λ), the difference between the latter distribution of λ and the Gaussian λ-distribution is small, and these two types of distributions may not be distinguished, given a realistic amount of noise in the experimental data.

Finally, we comment on a disagreement between the parameters of the Gaussian distributions resulting from the analysis of the HB and fixed-temperature HR on one hand and the recovery upon thermocycling on the other hand. The most likely explanation is that thermocycling probes certain features of the protein barrier distribution not probed by burning, and that the hole is filled not only by the molecules previously burnt out in the process of producing a hole but by random molecules several cm^{-1} away from the hole as well. (This situation is different from spectral diffusion causing hole broadening, where single spectral shifts are much smaller than the hole width or a single-scan range; Fig. 3.12) The distribution involved in this process will be the full ground-state barrier distribution for the respective protein landscape tier, not just the partial distribution corresponding to the hole. The excited-state barriers of that tier are characterized by higher λ than for the tier probed by burning, in agreement with the higher md^2 estimates above. Note that, for this scenario to contribute to our observations, it is not necessary for the respective tier of the protein energy landscape to be out of thermodynamic equilibrium. As long as there is lack of molecules absorbing in the spectral segment with the hole, there will be some net flux of molecules into this segment. (The tendency to increase the entropy may override the tendency to minimize the energy, and the hole represents "order".) However, as we will see in Chapter 5, our samples are away from thermodynamic equilibrium after realistic cooling.

The recovery upon thermocycling depicted in Fig. 4.16 is in reasonable agreement with the Gaussian barrier height distribution for this additional spectral-diffusion tier. Therefore, there is no evidence for ~ $1/\sqrt{V}$ barrier distributions in CP43. On the other hand, in light of the above arguments, the previously reported observations of ~ $1/\sqrt{V}$ barrier distributions [59], [60], [62] just might be misinterpretations, even in glasses. Consequently, one of the two energy-landscape tiers observed in this work and characterized by Gaussian distributions may reflect the dynamics of the amorphous host surrounding the protein (i.e., the frozen buffer/glycerol glass), rather than of the protein itself. It has been argued that some features of the spectral diffusion observed in single LH2 complex experiments could be assigned to the dynamics of the amorphous solid outside of the protein [83] or to protein-host surface TLS [5], [113]. More experiments, in particular with complexes where the lowest-energy state (the state being burnt and possessing narrow ZPL) is better screened by the protein from the surrounding buffer/glycerol glass, are necessary to clarify the origins of various tiers of the spectral diffusion dynamics in protein−chlorophyll complexes. This may not be an easy task, since in antenna complexes the lowest energy pigment is likely located on the periphery of the complex, at the side facing the next complex in the energy transfer chain (e.g., the reaction center). We note that hole broadening was extremely slow for the CP47−RC complex of PS II compared to isolated CP47 and PS II RC [114]. Another possible avenue of study involves exploring whether changes in the amorphous host (e.g., deuteration of buffer and/or glycerol) surrounding CP43 or other simple antenna complexes affect the parameters of HB and HR. A similar approach has been applied in [115] to single-complex PS I studies.

4.6. Conclusion

The dispersive character of NPHB and presence of some spectral memory result in the barrier height *V* (or tunneling parameter λ-) distributions actually contributing to the holes that are significantly different with respect to true, full distributions. This becomes particularly important in the case of a uniform λ-distribution, corresponding to the ~ $1/\sqrt{V}$ barrier height distribution, widely employed in theories explaining low-temperature properties of amorphous solids. Partial λ-distributions in this case are highly asymmetrical and result in predictions concerning HR that are incompatible with experimental results. We demonstrated that tunneling is responsible for both NPHB and HR below 12 K in the CP43 antenna protein complex. NPHB involves tunneling in the excited state (Fig. 3.12), while HR at least below 12 K involves tunneling in the ground state of the system. A simple experiment involving the measurement of HGK curves (i.e., of HB yield) at different temperatures can be performed in a variety of amorphous systems, to further confirm that tunneling is the dominant NPHB mechanism in a given temperature range and to determine the upper limit of md^2 in these systems. In the case of the CP43 protein complex, the upper limit of md^2 appears to be ~1.0×10^{-46} kg·m^2. Interestingly, the same upper limit can be obtained from thermocycling results (Fig.

4.14). However, the acceleration of the initial stage of burning (Fig. 4.8.B) and slowdown of recovery observed at 13 K (possibly additional SHB induced by the measurement light; see Fig. 4.8.B) suggest that barrier hopping in the excited state may become important for the smallest λ at this temperature. If this is indeed the case, 1.0×10^{-46} kg·m^2 is the true md^2 rather than its upper limit. Thus, the structural elements involved in tunneling in the CP43 protein are most likely the protein side chains (e.g., small amino acid ligands), although proton tunneling cannot be excluded at this point. It also appears that thermocycling in CP43 SHB experiments probes some barrier distribution features incompatible with the 5 K HB and HR data, (i.e., a distribution other than the sub-distributions directly created and probed by SHB). We suggest that HR at higher temperatures is partially due to spectral diffusion on the higher-barrier tier of the protein-energy landscape, with the respective generalized coordinate being different from that involved in the SHB process.

The CP43 parameters were chosen for further modeling studies in Chapter 5.

Chapter 5

5. Multi Level System Model

In this chapter an extended hole burning model (including light-induced spectral jumps, or NPHB on the single molecule level) based on MLS is introduced and the results of simulations based on this model are discussed. The results of our simulations are compared with experimental results on CP43 for which detailed HB and recovery data were presented in Chapter 4 (as mentioned earlier, see the end of Section 4.4.2).

This chapter is based on our paper in preparation as:

Mehdi Najafi, Valter Zazubovich, “Monte-Carlo Modeling of Spectral Diffusion Employing Multi-well Protein Energy Landscapes: Application to Photosynthetic Complexes” and several conference presentations.

5.1. Introduction

Spectral diffusion and underlying features of the protein energy landscapes have been a subject of numerous studies, employing single (protein) molecule spectroscopy, as well as sub-ensemble techniques such as spectral hole burning (SHB) [3], [58], [116], [117, p. 261], [118]–[121]. Pigment-protein complexes involved in photosynthesis are the class of protein systems probably most thoroughly studied by optical methods. In these complexes, pigments are built into the protein by Nature, in a broad variety of local environments, without chemical manipulations or genetic engineering. Although significant progress has been achieved, full understanding of spectral diffusion phenomena is elusive. Multiple pieces of the puzzle are available, but the whole picture is yet to emerge. For instance, it is a matter of debate if tunneling or barrier-hopping are behind the single photosynthetic complex spectroscopy (SPCS) observations in LH2 [42], [92]. It was implicitly assumed in many SPCS papers, as evidenced by reporting the jump rates in s^{-1}, without any reference to photon flux, that the observed spectral diffusion is thermally induced (i.e. occurs anyway, whether one observes it by SPCS or not), while comparison between SHB yields and photon budgets of SPCS experiments indicates that most shifts have to be light-induced, i.e. represent non-photochemical hole burning (NPHB) on a single-molecule level [77]. SPCS and SHB give contradictory information on spectral line shift distributions for the same system [77 and references therein].

Here we are going to explore, by means of computer modeling, how certain simple and realistic protein energy landscapes are expected to affect SHB and some SPCS observations. We are extending the two-level system (TLS)-based NPHB model to multi-well systems. In general, NPHB involves local rearrangement of the pigment molecule environment triggered by optical excitation. The original NPHB model [49], [76], [122] assumes that the pigment is in interaction with just one structural element of protein (amorphous solid) capable of conformational changes between two nearly identical sub-states (a TLS, see Section 3.4.). The pigment transition energy changes as a result of the conformational change by several wavenumbers to several tens of wavenumbers, which, given that electronic transition frequencies are in the range between 12,000 and 20,000 wavenumbers, constitutes shifts of the order of 0.1% and less. As long as one is dealing with just one TLS per pigment (the absorption of the burnt molecules is eventually returning to pre-burn wavelength), keeping track of spectral shifts is possible even with relatively limited computational resources using models based on the HB master equation [49], [76]. However, SPCS results clearly demonstrate that the number of available conformational sub-states is much larger than two per pigment molecule. Recently we introduced a modified HB model, still based on the HB master equation, which allows pigment molecules experiencing NPHB to assume essentially any number of spectral positions, with no memory of the preceding spectral shifts. This, however, is still an oversimplification, and just the opposite limiting case with respect to the "perfect spectral memory" case of [76]. There are multiple indications that the number of available conformational substates is limited. The evidence comes not only from SPCS, but also from the analysis of the hole recovery [42]. Dependence of the hole recovery rate on the depth of the originally burnt hole is a clear signature of a significant degree of spectral memory (see Section 4.4.4.). Introducing MLS with competing transitions to more than one other substate into the HB model [76] results in a significant decrease in computational complexity. The functions describing the distributions of spectral shifts ("anti-hole" or "photoproduct" functions) in both [76] and [42] are phenomenological and not straightforwardly related to the features of the energy landscape. (Anti-hole distributions could be compared to the shapes of the first cumulant distributions in SPCS experiments [81], [83].) Finally, any HB model based on the master equation (eq. 3.15) is applicable only to ensembles, and cannot be easily adapted to interpretation of the SPCS results, beyond offering independent benchmarks for (sub)-ensemble averages.

Here we introduce a model capable of keeping track of individual pigment-protein systems. Averaging the results for a large number of systems allows for modeling the evolution of the resonant spectral hole area and anti-hole shape (but, at this stage, not the hole width) upon burning, and in both fixed-temperature recovery and thermocycling experiments. A related issue, which will be addressed as well, is how close the systems explored in low-temperature optical experiments are to thermodynamic equilibrium prior to hole burning or prior to the beginning of a typical SPCS experiment.

5.2. Model

As stated above, each pigment-protein system is characterized by correlated energy landscapes for the ground and excited electronic states of the pigment molecule. In the most general case this correlation means that the distance between neighboring wells (*d*) and the mass of the tunneling entity (*m*) in both states are the same[1]. The landscapes for each of *N* systems are randomly generated, drawing barrier heights and well depths from two different (Gaussian [42]) distributions.

Two types of the energy landscapes with 22 wells[2] were considered. At this point we did not attempt to model multi-dimensional energy landscapes and therefore only

---

[1] However, there could be other levels of correlations such as excited state barrier set being a down-scaled copy of the ground state barrier set, as opposed to producing each state barrier set by independent random number generation (still with the same d and m).

[2] The number of well is chosen in such a way that there are identical number of wells with respect to the bottom of parabola in the case of parabolic landscape. Bigger number does not change the results.

transitions between two adjacent wells were permitted. In the first model, both ground and excited state landscapes are composed of a parabola (representing the bottom of the well on a higher-order tier of the protein energy landscape, see Fig. 3.11) modulated by a collection of barriers (in the following - “parabolic energy landscape”). In the second model, there is no parabola in the background, and barrier heights and depths of wells are both subject to two different Gaussian distributions (in the following - “flat energy landscape”).

The parameters of the barrier distributions are chosen to match those obtained for CP43 in [42] (Table 4.1). Note that the latter were obtained by fitting CP43 results to a TLS-based SHB master equation and matching equations governing recovery. Thus, differences in hole burning and recovery behavior potentially following from this model will be attributable strictly to multi-well character of the landscape. Similar parameters, at least for the excited state barriers, have been obtained for other PS complexes as well in [77] and [78] (Section 4.4.2.). Barriers are on average 5 times higher in the ground state than in the excited state. The Gaussian distribution of the ground state barriers is peaked at 1187 and has the width 283 cm^{-1}. The bottom of the well distribution is a Gaussian peaked at 20 cm^{-1} and with a width of 10 cm^{-1}. This barrier distribution approximately[1] corresponds to λ distribution peaked at 24.6 and with a width of 2.9. The coefficient of the parabola is also assumed to be smaller in the excited state, based on the argument that barriers have to be lower in the excited state also on the next tier of the energy landscape.

---

[1] It is approximately since choosing Gaussian distribution for barrier height does not mathematically result in Gaussian λ distribution (see Chapter 4.).

The ground state parabola coefficient k_g can be estimated based on the average anti-hole shift with respect to the hole, which in turn is close to ground state asymmetry, i.e. Δ~10 cm^{-1}. $2\Delta/d^2=k_g$.

These two energy landscapes are shown in Fig. 5.1.

The results of our simulations are shown for an ensemble consisting of 5000 systems in the following sections. It should be stressed that the real number of pigments in a typical bulk sample is on the order of 10^{15} in approximately 40 mm^3 cuvette volume (much larger than 5000)[1]. However, since for each system we are considering evolutions of probability distributions rather than discrete jumps, one could argue that each of the 5000 systems in turn represents a whole sub-class of the real single-pigment-in-the-protein systems. Since the results of our simulation are mostly in agreement with experimental results (and disagreements are not related to the number of systems), we believe that 5000 systems is sufficient.

---

1 This estimate is based on laser beam diameter of about 0.5 cm on a several mm thick sample, sample peak optical density of ~0.6-0.7 and chlorophyll extinction coefficient.

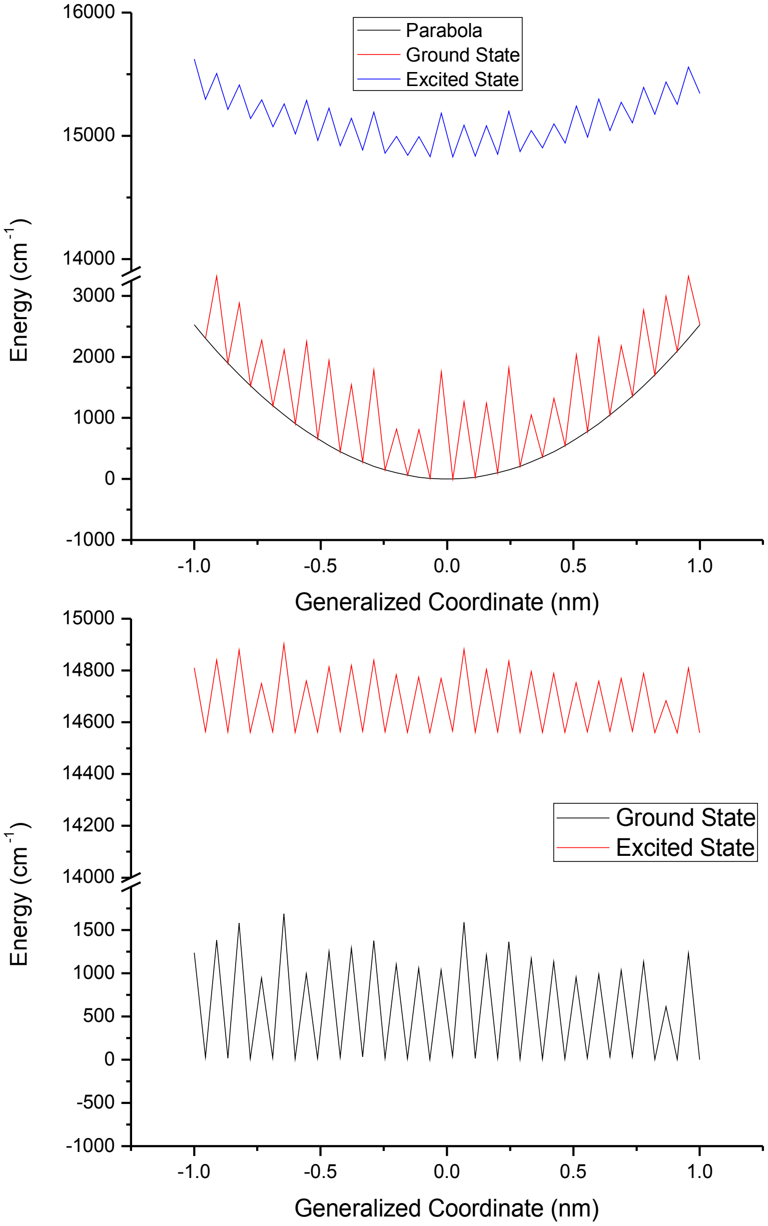

Figure. 5.1. The parabolic and flat energy landscapes . The only difference between these two models is that the barrier heights drawing from a Gaussian random generator are added to a parabola in the former model. However in the second model the bottom of wells are situated randomly based on different distributions of parameters than the barrier heights. Please notice that excited state energy is almost two orders of magnitude higher than the ground state one.

5.2.1. Rate Equation

At any step in the pigment+protein system evolution, its state of the system is described by a set of probabilities to be found in a given well, $P_{i,a}$ where $a = e$ or g for ground and excited states, respectively, and $i = 0...N\text{-}1$, where N is the total number of wells in the (excited or ground) state of the system and $\sum_{i=0}^{i=N-1} P_{i,a} = 1$. The energy difference between the baselines for the ground and excited states is subject to a separate Gaussian distribution, with the width equal to typical inhomogeneous bandwidth (the width of the site distribution functionb) in photosynthetic complexes, ~100-200 cm^{-1}. Hole burning and subsequent recovery involve changes to the set of probabilities $P_{i,a}$. The evolution of this set of probabilities is determined by solving the rate matrix, containing the rates of transitions (including both tunneling and barrier-hopping rates: eqs. 3.22, 3.23 and 3.28) between different wells of the protein energy landscape as follows:

The basic equation which should be solved here is a set of coupled differential equations with some initial conditions. In a simple case, as an example, there could be three wells (A, B, C) with initial condition that the probability of finding a particle in one of them is one and in others are zero. In case that only the neighboring wells can interact with each other, there are only 4 rates[1] (α, β, γ, δ) which connect these three wells together [123]:

---

[1] In our simulation these are sum over tunneling and hopping rates for neighboring wells.

$$A \underset{\beta}{\overset{\alpha}{\rightleftharpoons}} B \underset{\delta}{\overset{\gamma}{\rightleftharpoons}} C$$

The probability in each well changes through the following equations:

$$\begin{aligned}
\frac{dP_A}{dt} &= -\alpha P_A + \beta P_B \\
\frac{dP_B}{dt} &= \alpha P_A - (\beta+\gamma) P_B + \delta P_C \\
\frac{dP_C}{dt} &= \gamma P_B - (\delta P_C)
\end{aligned}$$

or in terms of matrix algebra:

$$\frac{d\boldsymbol{P}}{dt} = \boldsymbol{R} \cdot \boldsymbol{P}$$

where ***P*** and ***R*** are probability and rate matrix as follows:

$$P = \begin{pmatrix} P_A \\ P_B \\ P_C \end{pmatrix}$$

and

$$R = \begin{pmatrix} -\alpha & \beta & 0 \\ \alpha & -(\beta+\gamma) & \delta \\ 0 & \gamma & -\delta \end{pmatrix}$$

One way to solve these equations simultaneously is using matrix algebra which is explained in most of the standard differential equation books. Briefly, a guessed answer, which is an exponential function, should be substituted instead of ***P*** (e.g. $\boldsymbol{P} = \boldsymbol{U} e^{\lambda t}$ where ***U*** is a matrix that each column equals to one of eigenvectors of ***R***, t is time, and λ is eigenvalues of rate matrix, ***R***). By knowing the initial condition ($\boldsymbol{P_0}$) the answer would be:

$$P_i = \sum_{k=1}^{3} \left(U^{-1} \cdot P_0\right)_k U_k e^{(\lambda_k t)}$$

where i = 1-3 means the probability in wells A, B, and C respectively. In practice, we used GSL - GNU Scientific Library to solve the eigensystem problem by applying Schur decomposition [124].

It should be mentioned that the elements of the rate matrix could differ one from another by several orders of magnitude, which may result in a huge errors in eigensystem calculation using numerical methods. Therefore, prior to computing the eigensystem, the rate matrix should be balanced. This means that through some similarity transformations the rate matrix will be changed to another matrix with the same eigenvalues but all columns and rows of this matrix having comparable norms. The eigenvectors of the balanced matrix will be converted to the original matrix eigenvectors by a back transformation. However, there is always some chance that the eigensystem calculation is not performed correctly through matrix algebra. To make sure that eigenvalues and eigenvectors are correct there are two tests which are done after each calculation. a) the trace of rate matrix should be equal to the sum over eigenvalues and b) $\boldsymbol{P} \cdot U_k$ should be equal to $\lambda_k U_k$.

If the problem for a particular system could not be meaningfully solved by the eigensystem approach or the solution did not pass the tests, then we used more time- and computational resources-consuming differential equation solving by other method(s) such as: Runge-Kutta, Implicit Bulirsch-Stoer, or backward differentiation formula (BDF) method in Nordsieck form. The latter one from GSL library is applied in our program [124].

5.2.2. Multistep Burning

The probability distribution at the start of the low-temperature optical experiment is a result of the cooling process. The system is slowly cooled down from RT to 5 K in the dark (so that any evolution occurs only in the ground state of pigment-protein system). We start with the Boltzmann distribution for 300 K ($P_{i,g} \sim exp(-E_{i,g}/k_B T)$, where $E_{i,g}$ is the bottom of the well *i* and $\Delta E_{i,g}$ is barrier height between adjacent wells in the ground state, V in Fig. 3.9 for a TLS), with probabilities determined by the ground state landscape. The $P_{i,g}$ at 5 K is found via a multi-step procedure imitating gradual cooling.

Once the pre-burn distribution $P_{i,g}$ is established, we start simulating the hole burning. For every system, a well is chosen so that the energy difference between the ground and excited state for this well matches the fixed burn frequency (same for all systems). This well may be different (i.e. have different index *i*) for different systems. Let's say in a particular system the resonant well is well number *j*, and the respective probability is $P_{j,g,before}$. This is the probability that a given system will be in resonance with the narrow-band laser excitation to begin with. As a result of the absorption of a photon, the system finds itself in the excited electronic state. The evolution in the excited state is started with $P_{j,e} = 1$, and all other $P_{i \neq j,e} = 0$. The system is given several nanoseconds (excited state lifetime) to evolve in the excited state. Rate equations are used to determine the respective excited state probabilities $P_{i,e,after}$. The system then returns to the ground state. All evolved $P_{i.e}$ are multiplied by $P_{j,g,before}$ (see above) and results are added to $P_{i,g}$ for all i, with one exception: the $P_{j.e,after}$ is multiplied by pre-burn $P_{j.g,before}$ and placed instead of the pre-burn $P_{j.g,before}$. This procedure results in a distribution of $P_{i,g}$ still normalized to 1, but with the shape changed compared to the pre-burn distribution. The probability to find the system in resonance with the laser (in well *j*) has been reduced, and the probability to find the system in other wells has increased somewhat. This modified ground-state probability distribution can be used for different purposes:

- It can be used as initial state to model subsequent acts of burning
- It can be used as a starting point of modeling recovery, at various temperatures.
- It can be used to calculate the hole spectra.

Additional hole burning involves repeating the single burning step described above, but with the initial ground-state distribution being the result of a previous burning step. The $P_{j,g}$ after the previous step becomes the new $P_{j,g,before}$. It should be noted that in practice, the probability of a photon being absorbed is determined by the absorption cross section and the actual photon flux, which is usually too small to supply the photons to every system every few nanoseconds. Thus, in reality, there is a delay between two consecutive acts of burning. During this delay, the system can experience some recovery.

The time interval between each action of burn can be calculated by knowing the absorption cross section and other physical parameters of the sample and the laser such as laser wavelength, power, beam diameter, concentration of sample, etc.

The absorption cross section characterizes the ability of a pigment to absorb a photon and is related to the molar extinction coefficient as $\sigma = 3.82\times 10^{-21}\,\varepsilon$ [125] where ε is the molar extinction coefficient in $L.mol^{-1}cm^{-1}$. This parameter is measured for Chl a in two different media, methanol and diethyl ether in [12] (see Fig. 2.4). Then the peak[1] of the absorption cross section (σ) of Chl a in methanol and diethyl ether (in the range of 500-700 nm) can be found as $1.26\times10^{-16}cm^2$ and $3.24\times10^{-16}cm^2$ respectively. This results in an average peak of σ at room temperature (RT) as $\bar{\sigma}_{peak,RT}=2.26\times10^{-16}cm^2$. To find this value at low temperature, (LT) it should be multiplied by the ratio of homogeneous bandwidth at RT (200 cm^{-1}) over LT (0.03 cm^{-1}, at 5 K):

$$\bar{\sigma}_{peak,LT}=\bar{\sigma}_{peak,RT}\times\frac{\Gamma_{RT}}{\Gamma_{LT}}=1.05\times10^{-12}\,cm^2$$

To calculate the time interval between two consecutive absorptions, this probability should be multiplied by photon flux which is

$$Photon\ flux=\frac{number\ of\ photon}{time(second)\times illuminated\ area(cm^2)}=\frac{Laser\ Power(W)}{\frac{hc}{\lambda}}\times A(cm^2)$$

where h, c, λ are Plank's constant, the speed of light, and the laser wavelength and A is the illuminated area which is related to the beam diameter. Thus the probability of photon absorption is $\bar{\sigma}_{peak,LT}\times Photonflux$, and the time interval between two photons to be absorbed in a row (Δt) is the inverse of this value. By converting all values to proper units which are used in our experimental setup and substituting all constants we have:

---

[1] The maximum value of σ is used to find the minimum required time interval between two acts of burning as an estimation.

$$\Delta t = \frac{1}{\bar{\sigma}_{peak,LT} \times Photonflux} = \frac{d^2(cm^2)}{\bar{\sigma}_{peak,LT}(cm^2) \times P(mW) \times \lambda(nm) \times 1.56 \times 10^{-13}(mJ.nm)}$$

P and *d* are beam diameter and laser power respectively. The typical value of Δt is about 53 ms corresponding to laser intensity in the sample of 5 µW/cm^2. This is orders of magnitude larger interval than fluorescence lifetime, and, therefore, any saturation effects can be ignored.

As mentioned above, during this time interval the system can recover to some extent. If one disregards this correction (recovery between the consecutive acts of burning) the burn process treatment can be simplified in the following way. For instance, the burning process for only two wells is modeled as follows. We assume that in the excited state ($P_{i,e,\ after}$), the probability of the system to be in the resonant well (*RW*) after each act of burn reduces from 1 to 0.9 and the probability to end up in the non-resonant (*n-RW*) well will increase from 0 to 0.1. Let us assume that in the ground state ($P_{i,g,\ before}$), the probability of resonant well is 0.7 and in the other well is 0.3. The schematic of multi-step burning (three steps) is shown in below:

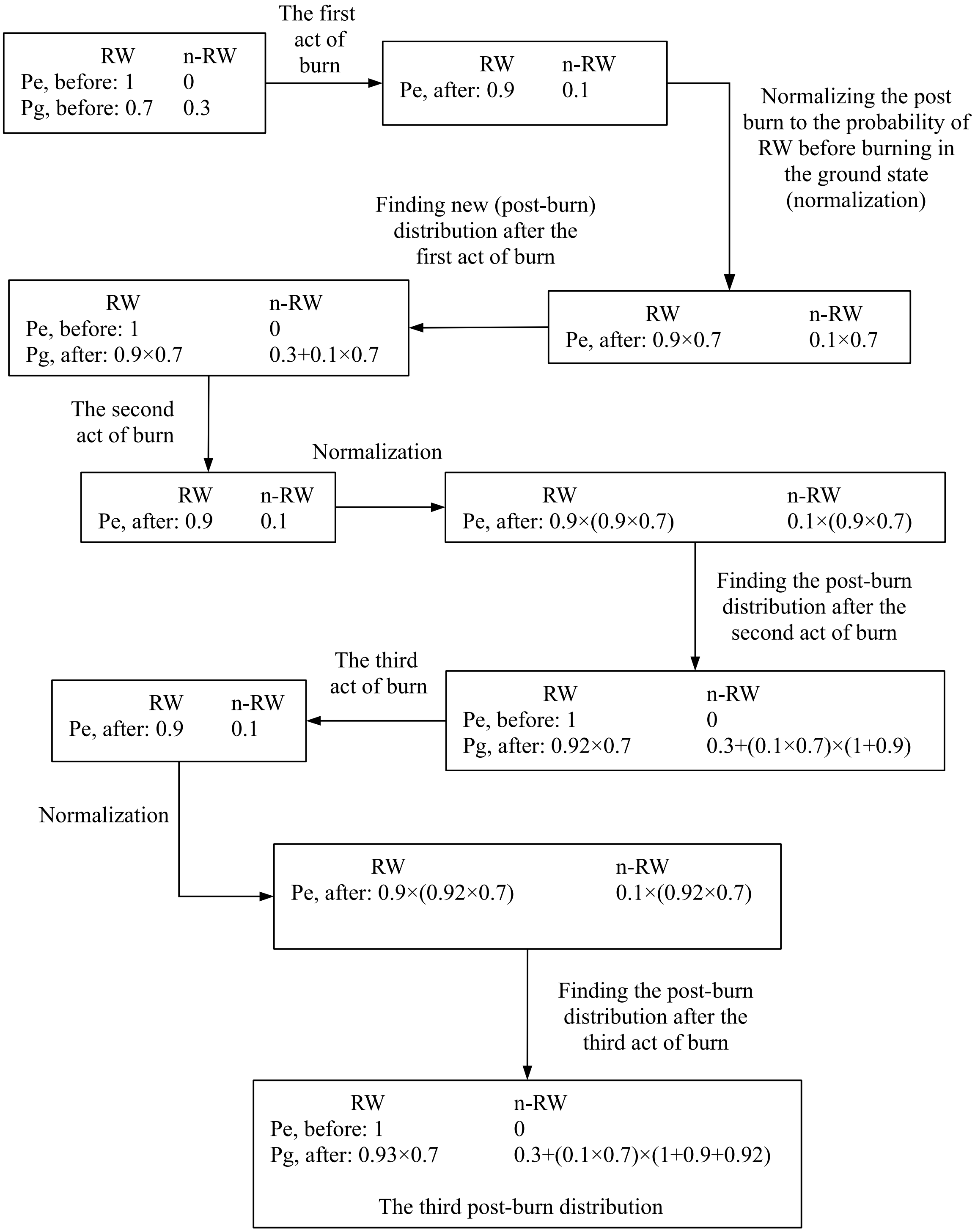
RW n-RW
Pe, before: 1 0
Pg, before: 0.7 0.3
The first act of burn
RW n-RW
Pe, after: 0.9 0.1
Normalizing the post burn to the probability of RW before burning in the ground state (normalization)
RW n-RW
Pe, after: 0.9×0.7 0.1×0.7
Finding new (post-burn) distribution after the first act of burn
RW n-RW
Pe, before: 1 0
Pg, after: 0.9×0.7 0.3+0.1×0.7
The second act of burn
RW n-RW
Pe, after: 0.9 0.1
Normalization
RW n-RW
Pe, after: 0.9×(0.9×0.7) 0.1×(0.9×0.7)
Finding the post-burn distribution after the second act of burn
RW n-RW
Pe, before: 1 0
Pg, after: 0.92×0.7 0.3+(0.1×0.7)×(1+0.9)
The third act of burn
RW n-RW
Pe, after: 0.9 0.1
Normalization
RW n-RW
Pe, after: 0.9×(0.92×0.7) 0.1×(0.92×0.7)
Finding the post-burn distribution after the third act of burn
RW n-RW
Pe, before: 1 0
Pg, after: 0.93×0.7 0.3+(0.1×0.7)×(1+0.9+0.92)
The third post-burn distribution

By the same analogy we could conclude that the probabilities of post burn in the ground state after *n* acts of burn in resonant ($P_{j,\, g,\, resonant,\, after}$) and non resonant ($P_{j,\, g,\, non\text{-}resonant,\, after}$) wells are:

$$P_{j,g,resonant,after} = P_{j,g,resonant,before} \times \left(P_{j,e,resonant,after}\right)^n$$

and

$$\begin{aligned} P_{j,g,non\text{-}resonant,after} &= P_{j,g,non\text{-}resonant,before} + \left(P_{j,g,resonant,before} \times P_{j,e,non\text{-}resonant,after}\right) \times \\ &\quad \left\{1 + \left(P_{j,e,resonant,after}\right)^1 + \left(P_{j,e,resonant,after}\right)^2 + \ldots + \right. \\ &\quad \left. \left(P_{j,e,resonant,after}\right)^n \right\} \\ &= P_{j,g,non\text{-}resonant,before} + \left(P_{j,g,resonant,before} \times P_{j,e,non\text{-}resonant,after}\right) \times \\ &\quad \sum_{k=0}^{n-1} \left(P_{j,e,resonant,after}\right)^k \end{aligned}$$

by considering the fact that $\sum_{k=0}^{n-1} z^k = \frac{-1+z^n}{-1+z},\ z \in \mathbb{R}$, $P_{j,\, g,\, non\text{-}resonant,\, after}$ is:

$$P_{j,g,non\text{-}resonant,after} = P_{j,g,non\text{-}resonant,before} + \left(P_{j,g,resonant,before} \times P_{j,e,non\text{-}resonant,after}\right) \times \frac{-1 + \left(P_{j,e,resonant,after}\right)^n}{-1 + P_{j,e,resonant,after}}$$

In these equations, $P_{j,\, g,\, resonant,\, before}$ and $P_{j,\, g,\, non\text{-}resonant,\, before}$ are probabilities in the jth resonant and non-resonant wells in the ground state before burning (0.7 and 0.3 in above example) respectively. Similarly, $P_{j,\, e,\, resonant,\, after}$ and $P_{j,\, e,\, non\text{-}resonant,\, after}$ are probabilities in the jth resonant and non-resonant wells in the excited state after burning (0.9 and 0.1 in above example) respectively.

Therefore by calculating the burning process once only (to find $P_{j,\, e,\, resonant,\, after}$ and $P_{j,\, e,\, non\text{-}resonant,\, after}$), one can calculate the post burn probability in well number *j* after several acts of burning through those analytical equations. It works much faster than calculating the post burn sequentially. The disadvantage of this technique is its inability to consider recovery correction during the burning process. Since this effect is not significant, we neglect it for the time being.

5.2.3. Recovery Simulation

After the burning process is completed, we study the recovery of the hole either at a fixed temperature or upon thermocycling. Hole recovery at fixed temperature starts with post-burn $P_{i,g,after}$, $i=0...N-1$, and the system is allowed to evolve for some time, in ground state (in the dark) and with respective ground-state rates. In the case of thermocycling, one has to simulate multiple relatively short recovery steps sequentially, according to the temperature change profile resembling those in experiment, with $P_{i,g,\ after}$, $i=0...N-1$ after one step serving as initial conditions for the next step. Intermediate calculation of spectra at every temperature or after every small time step is not necessary, only at T_{burn} after each temperature cycle.

The hole spectrum is calculated in the following way: For every system separately, the difference between the pre-burn and post-burn ground state distributions is converted into the difference in absorption spectra. For resonant well j (j may differ from system to system), the $P_{j,g,\ after} - P_{j,g,before}$ is negative, which corresponds to the resonant hole. For all other wells $P_{i,g,\ after} - P_{i,g,before}$ is positive (or zero far enough away from the hole), which corresponds to the anti-hole. When the results for all systems are being summarized and binned, they should be added with the weight equal to pre-burn $P_{j,g,before}$ (before any burning) for this particular system. As one may guess from the above description, the model does not simulate the hole broadening, and the width of the hole stays equal to the chosen width of the frequency interval of the binning process. Within this framework, hole depth is proportional to hole area, and either parameter can be used in the same way when describing hole recovery.

5.2.4. Quasi-Single Protein Complex Spectroscopy Simulation

The advantage of our approach is in keeping track of all changes in well probabilities that makes the SPCS simulation possible too. This means that the change in probability distribution in one system can be compared with the results of SPCS, and that taking the average over many systems gives the result of SHB (as discussed above).

In SPCS experiments, the absorption band of the protein complex (or molecule) is scanned with relatively high intensity light (~10 W/cm^2) several (~1000) times with a speed of ~40 cm^{-1} / s (these typical values are taken from [81]).

This process can be modeled as follows: While the wavelength of laser is changing during scanning over the absorption band, different resonant wells are chosen accordingly. These wells are not necessarily in the same order as well numbers. Since the wells are generated randomly, the energy difference between the ground and excited states in the first well (as an example) can be greater than that of fifth one and so on. Then the average value over post burn probability after each act of burning in this well is considered as final post burn probability for the purpose of calculating the observable (optical signal at given wavelength). The average value is chosen because in practice, the signal at each wavelength is measured during the scan process and not in the end. Here it is important to distinguish between probability distributions and observed spectra. The probabilities P should always add up to 1, but the spectra do not have to be normalized. Because we may chase one and the same system through many wells and excite it several times within one and the same laser scan (the post burn probability is probability after all burns, the observable, i.e. spectrum, is proportional to average probability.) Following the change in the wavelength, if the next well is in resonance with the laser, it will be chosen and the burning process will be calculated; otherwise, the system has some time to be recovered. This process continues until all wells are chosen once. It should be noted that while the band is scanned there is a chance that the probability distribution among wells redistributes several times (since different wells are randomly in resonance with the laser). In the end, all well numbers are converted to wavenumber accordingly.

It should be pointed out that the real SPCS experiment is a discrete process, meaning that the molecule is in one well at a time, and while it is in that one well, it does not absorb at other wavelengths. However in the present approach (burning in the single molecule level) there is always a probability for molecule/complex to be found in a conformational sub-state upon photon absorption rather than observable ones in experiments (corresponding to those discrete jumps in SPCS). For that reason this approach is called Quasi SPCS. The goal of this approach is to arrive at distributions of shifts in the single molecule case, as opposed to the discrete step-by-step evolution which is actually observed in experiment and which people then attempt to observe for a very long time and arrive to shift distributions. Distributions of shifts and of first cumulants have been reported in [83] so experimental data for comparison is available.

5.3. Results

The results of different steps explained so far are given in subsequent sections:

5.3.1. Cooling step (Equilibrium versus Non-equilibrium?)

The pre-burn state of a system directly affects the burning process which in turn results in finding different parameters for protein energy landscape. The first question which we want to address is - Is the typical sample in equilibrium prior to a typical SHB or SPCS experiment? And if not - how far is a system from the equilibrium after cooling down?

To answer this question the cooling process is simulated by first assigning to each system in the ensemble a Boltzmann distribution at room temperature (RT). It appears, however, that the initial distribution is not very important, as above ~100 K the system evolves fast enough and at >100 K the probabilities obey Boltzmann distribution regardless of the choice of the initial RT distribution. However, for realistic cooling speeds (~300 K / 2 h), the whole ensemble and individual systems end up very far away from equilibrium at low temperatures (roughly below 50 K) due to the fast decrease of the hopping rate (eq. 3.28). In Fig. 5.2, the results of cooling of a single system in four

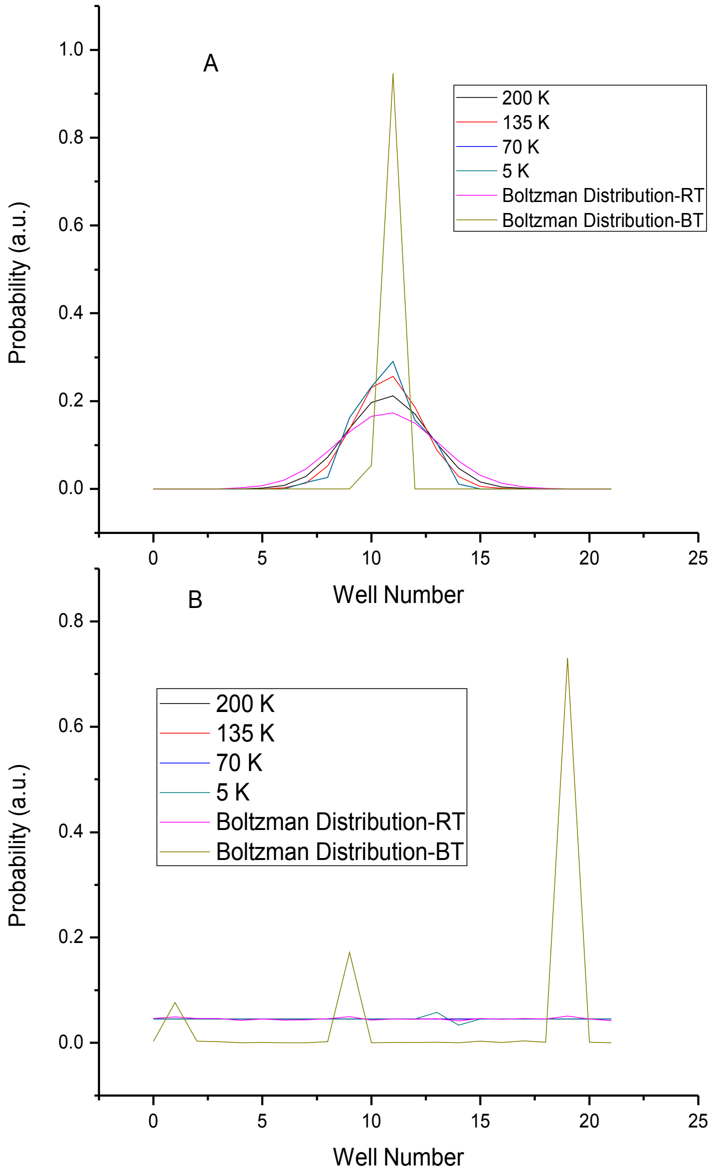

Figure. 5.2. The occupation probability distributions over 22 wells upon cooling the ensemble down from room temperature (RT) to burn temperature (BT) compared to equilibrium situation (Boltzman distribution) at corresponding temperatures. The calculation is done in an iterative fashion, however, the change between each step is not pronounced.

consecutive steps (interestingly enough there is not much dependency on number of step larger than four) within two hours for both types of energy landscapes are compared with Boltzmann distributions at RT and 5 K - burn temperature (BT).

In case of a parabolic energy landscape, most of the probability is distributed within just several wells at the bottom of the parabola. By cooling down the sample, the probability to find the system in the deepest well will be increased. However the probability distribution in the flat energy landscape case at higher temperatures is almost uniform since the relaxation rates at high temperatures are so fast (especially hopping). Because the relaxation rates become much smaller as the system cools down, the probability distribution stays more or less uniform (deeper wells become more probable to some extent). It can be understood in the following way: Equilibrium implies that deeper wells are occupied with greater probability. The deepest well could be located anywhere in the flat landscape model while in the parabolic model, the wells at the bottom of parabola always have the greatest population probability.

It should be noted that a system in either energy landscape model is far away from equilibrium after a reasonable cooling time (which is about two hours). Also, even allowing an ensemble a long time (couple of years) to relax still does not result in perfect equilibrium (not shown). This means that below a certain temperature, the system will be frozen in a situation far from equilibrium.

5.3.2. Burning Process

The next step after cooling the ensemble down is burning a hole. To compare the result of burning with the experiment, one can normalize the sum of the probabilities of finding each system in a resonant well (quantity proportional to pre-burn absorption) to one. Subsequent development will result in a hole growth kinetics (HGK) curve. The comparison between the results of our CP43 experiments [42], [78] and simulation (based on the flat landscape model[1]) is shown in Fig. 5.3.

The beginning of the HGK curve is reasonably matched with experiment, with discrepancy gradually increasing for fractional depths larger than 45%. The simulation predicts faster burning than observed in reality. This can be explained by taking into account that our model does not include electron-phonon coupling (only the zero-phonon line is included, but not phonon sidebands). It is well known that, all other parameters being the same, larger values of the Huang-Rhys factor S result in slower burning. On the other hand, our model, in effect, is a S=0 model. Taking into account the recovery already occurring at the time of burning reduces the apparent rate of the burning process by about 10%. Since taking the recovery during burning into account makes the program tremendously slow for deep holes (even for a small number of systems), it is not included in most calculations.

---

1 The parabolic one gives more or less the same result.

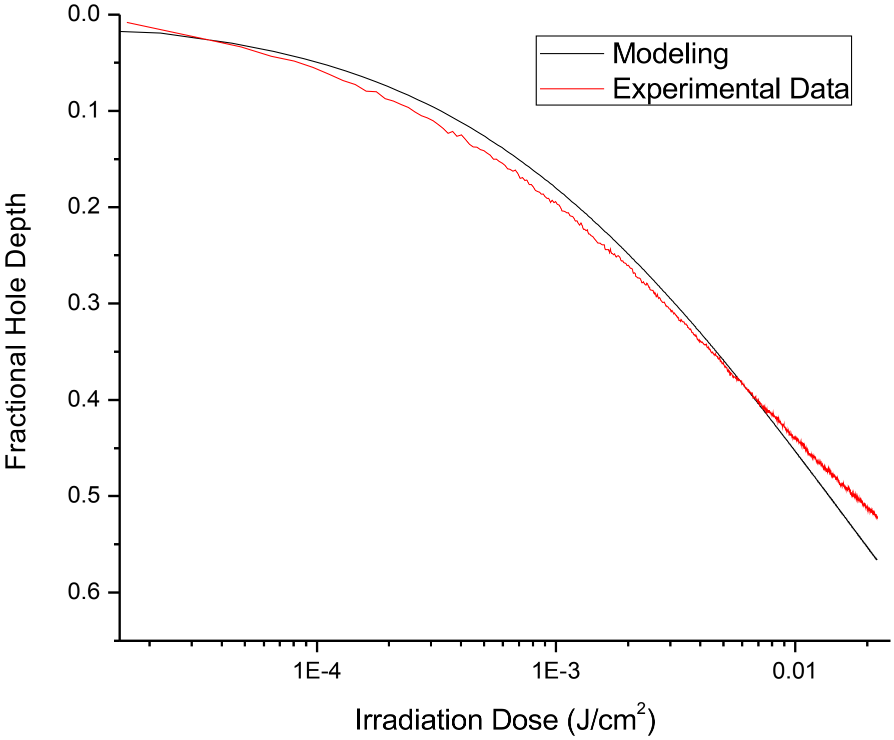

Figure. 5.3. Comparison between the experimental (black) and simulation (red) results of HGK of CP43. The difference between two models of energy landscape is negligible.

The hole/anti-hole spectrum shape in case of the flat energy landscape is approximately symmetrical with respect to the burn wavelength. However, for the parabolic energy landscape, most of the anti-hole is red shifted, which is expected since in most of the systems $P_{i,g}$ is largest at the bottom of the parabola and the energy difference between the ground and excited states is also the largest at the bottom of the parabola, as the curvature of the excited state parabola is lower. Thus, when the resonant well is at the bottom of the parabola, burning results in lower-energy (red) anti-hole, in disagreement with the experiment. The higher-energy part of the anti-hole results from exciting the systems occupying wells other than the most-likely bottom well. The calculated hole spectra for both models are depicted in Fig. 5.4. The results indicate that randomness, rather than the features of the next hierarchical tiers of the energy landscape (folding funnel), dominates the protein energy landscape.

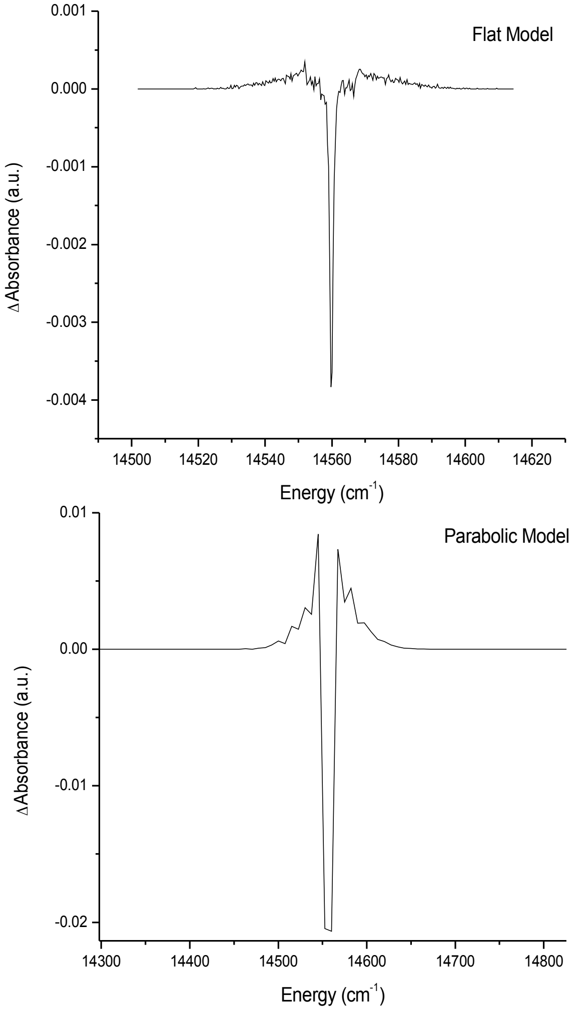

Figure. 5.4. Simulated hole spectrum (burned at 686.8 nm) based on two energy landscape models. Red shifted anti-hole in parabolic model does not match with experiment.

5.3.3. Recovery

To study the parameters of the energy landscape in the ground state, one should study hole recovery at fixed temperature (5 K) and upon thermocycling. The recovery of a hole depends on the conditions under which the hole was burned. Namely, the recovery process depends on how far the system was from equilibrium at the time of burning. The hole recovery dependence on the closeness of the initial conditions to equilibrium is depicted in Fig. 5.5. The hole which was burned while the ensemble was closer to the equilibrium recovered faster than the hole produced right after a realistic cooling time. This can be explained by considering the fact that the system always evolves towards equilibrium. Therefore if the equilibrium and starting condition are the same, upon burning, the system just recovers towards the equilibrium while in the system that is far away from equilibrium to begin with, hole recovery and evolution towards equilibrium may partially compete.

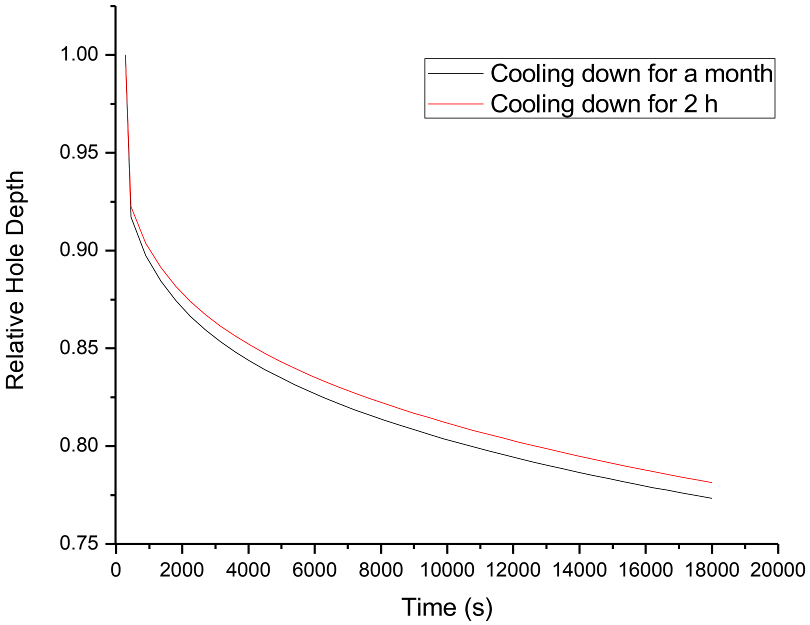

Figure. 5.5. Comparison between the recovery of two holes with different pre burn conditions. It shows that burning a hole in an equilibrium conditions results in faster recovery.

Also, the speed of the recovery process depends on the initial hole depth. Deeper holes recover more slowly than the shallower ones. That is illustrated in Fig. 5.6, which is in agreement with our experiments (see Fig. 4.9.A). As stated in the introduction, this effect is a manifestation of “spectral memory”. It should be mentioned that, qualitatively, the recovery behaviour is independent on the type of the energy landscape. The general tendencies in the recovery process described above were present for both types of energy landscape.

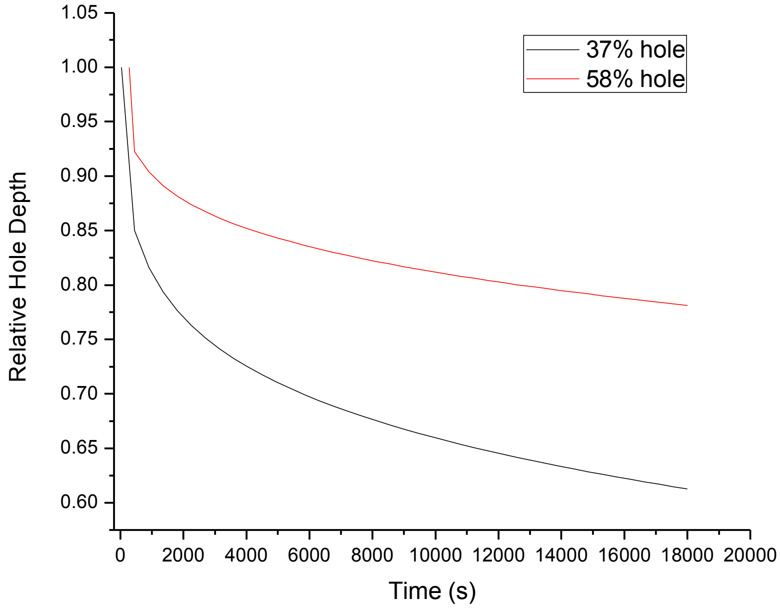

Figure. 5.6. Dependence of recovery on the hole depth. Shallower hole recovers faster.

In Fig. 5.7, the result of simulation for recovering of a 55% hole (sample cooled down within two hours before burning, HGK was shown in Fig. 5.3) is compared with the experimental result.

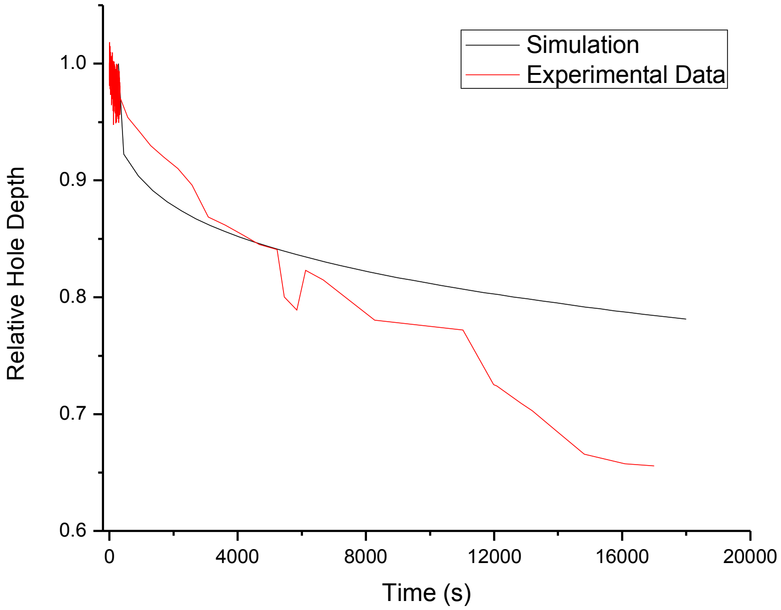

Figure. 5.7. Recovery of a simulated 55% hole is compared with the experimental data

5.3.4. Quasi-SPCS

Here the results of calculations of Quasi-SPCS are shown for CP43 according to Section 5.2.4. The scanned band is located between 14505.5 cm^{-1} and 14621.7 cm^{-1} (corresponding to 689.4 nm and 683.9 nm, respectively). The laser intensity and scan rate are borrowed from [81] as 5 W/cm^{2} and 44 cm^{-1}/s. The flat energy landscape is considered here with CP43 barrier distribution parameters (see Table 4.1).

Fig. 5.8 compares probability distributions before the beginning of the optical experiment after realistic cooling and those for the case when the SPCS experiment is started at thermodynamic equilibrium. It again proves that the equilibrium situation is not reachable within a reasonable time.

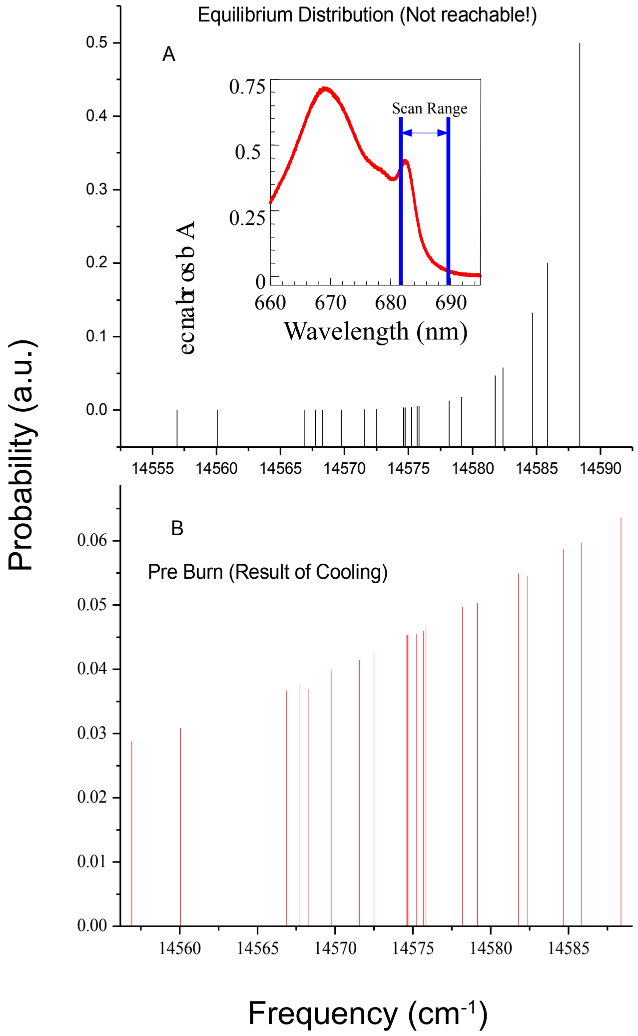

Figure. 5.8. Probability distribution in different wells in (A) equilibrium and (B) pre burn state as a result of cooling. Insert is the absorption spectrum of CP43 and above scanned range is shown.

The results of redistribution of probabilities in the energy landscape, starting from distribution corresponding to realistic cooling time after the 1st and 2000th scans are shown in Fig. 5.9. The comparison between the results of distribution after 2000 scans and equilibrium reveals that scanning helps the system to reach its equilibrium state.

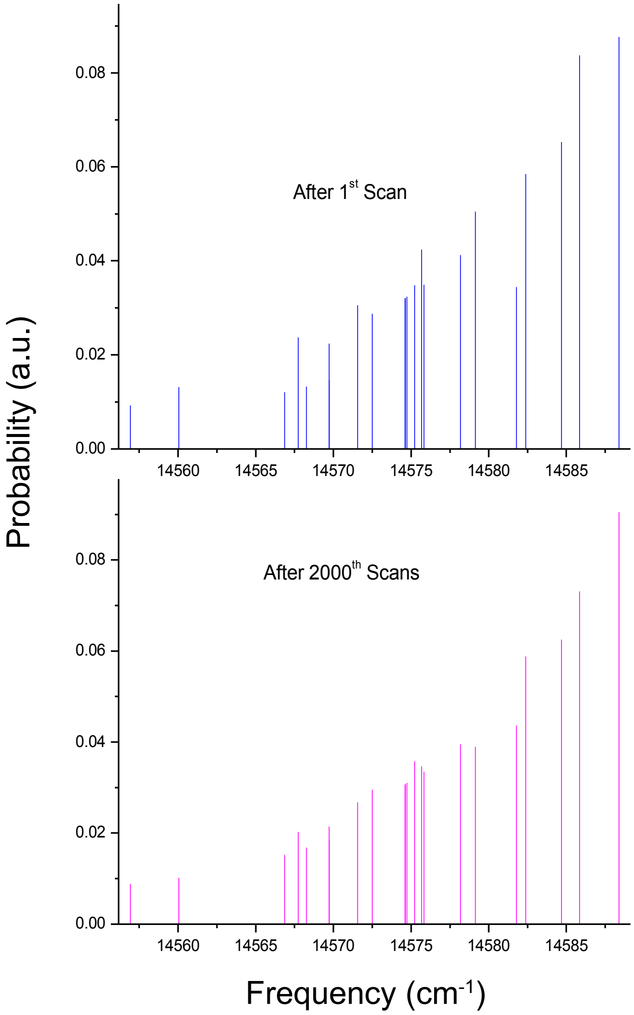

Figure. 5.9. Upon scanning the band of CP43 the distribution between wells is changing in such away that the system goes towards equilibrium.

5.4. Conclusion

We have reported the development and applications of spectral diffusion modeling software (covering hole burning, hole recovery and partially also single-molecule spectroscopy) involving random generation of multi-well protein energy landscapes and including both tunneling and barrier-hopping in both the ground and excited states of a protein/chromophore system. Evolution of such systems was determined by solving the rate equations. Using realistic parameters of photosynthetic (PS) proteins as initial guesses, we a) showed that initial cooling of the sample results in proteins quite far from thermodynamic equilibrium (for the landscape tier involved in hole burning), b) demonstrated the hole area evolution matching the experimental results in the case of both burning and fixed-temperature recovery (meaning that there is no qualitative difference between the SHB process involving TLS and MLS) and c) determined the effects of different protein energy landscapes on the anti-hole shape. The latter is especially important for determining how light-induced site energy shifts (hole burning) alter the picture of excitonic interactions in PS complexes, and for modeling their various resonant and non-resonant hole spectra.

Initial (quasi) single-complex simulations suggest that in typical single complex optical experiment the molecule experiences frequent light-induced spectral shifts, and has a finite probability to be observed in all available wells. Thus, single molecule/complex experiments likely yield the approximate number of available conformational sub-states, that is relatively small (but larger than two). Our calculations show that in SPCS experiment involving scanning the whole spectrum with the laser drives system towards thermodynamic equilibrium.

Chapter 6

6. Conclusions and Future Work

6.1. Conclusions

Despite much progress, some details of the functioning of the photosynthesis apparatus are a mystery, and many relevant parameters are unknown. In this study, we discussed several improvements to techniques for measuring the parameters of proteins' energy landscapes (which are crucial to understand their roles in photosynthesis, as well as in protein folding in general), and obtained the following key results: First, we presented evidence that the distributions of barrier heights on the energy landscape obey Gaussian distribution and not $1/\sqrt{V}$ distribution. The latter follows from models describing anomalous properties of amorphous solids at low temperatures, such as heat capacity, heat conductivity, etc., and was employed in explaining optical experiments in glasses.) Second, although the hole burning community generally believes that non-photochemical spectral hole burning is due to tunneling, this idea is not so well accepted in the single molecule/complex spectroscopy community. There have been debates about the nature of the process underlying spectral line jumps (manifesting as spectral hole burning in ensemble experiments) in single complex experiments, i.e., whether it is tunneling through barriers or hopping over barriers. Our results showed that independence of the hole burning yield on temperature implies that line jumps / SHB are tunneling based processes at temperatures below 12 K in protein-chlorophyll complexes. However the essence of the tunneling entity has not been fully determined yet. We are one step closer to identifying the tunneling entity by finding the higher limit of the characteristic md^2 parameter ($md^2 = 1.0 \times 10^{-46}$ kg•m^2). This indicates that tunneling in question involves either the lighter ones of the protein side chains or, somewhat less likely, protons.

We also introduced a new approach to modeling of both spectral hole burning and single-molecule spectroscopy data based on multi-level systems (MLS) and rate equations, rather than the so–called hole burning master equation used so far. MLS is by far more realistic representation of protein energy landscapes than TLS. Our simulation results showed an acceptable match with the experiments, considering that at this stage we have included only burning via ZPL and not through PSB. Interestingly, the results of our simulation proved that in practice we (and everyone else performing hole burning and single molecule spectroscopy measurements) are dealing with burning a sample which is far away from thermodynamic equilibrium. This is important, since starting from a non-equilibrium state affects the rates of burning and recovery, which in turn can affect the values of barrier height distribution parameters found in experiments.

6.2. Future Work

The arguments presented in this work in favor of a Gaussian barrier distribution were actually not protein-specific. Thus, it is questionable if $1/\sqrt{V}$ barrier distributions are present in any system, or if observing them was a result of insufficiently sophisticated experimental procedures and/or analysis. Thus, for the experimental part, one can continue the same approach mentioned in Chapter 4 for simpler systems such as chlorophyll-doped organic glasses or Cytochrome b_6f (Cyt b_6f) protein, that contain only one chlorophyll molecule per protein monomer. Applying similar experimental procedures to two simple representatives of two different classes of amorphous systems will allow for unambiguously determining the landscape's barrier distribution shapes and quantitative parameters. This allows one to better understand, predict and model the effects of small light-induced conformational changes on the primary processes of photosynthesis, to identify the origins of spectral diffusion behavior in other proteins and amorphous systems, etc. It hopefully eliminates any possibility of excitonic effects and accesses as "pure" optical manifestations of protein dynamics as possible. Additionally, the influence of external environment (frozen buffer/glycerol glass) on the observed protein dynamics will be explored employing deuterated buffer and glycerol.

In the modeling part, including the PSB in the model will make it more realistic and produce a better fit to our experimental results. For single-molecule behavior modeling, it is easy to make the transition from a probability distributions evolution approach employed so far to discrete spectral jumps by utilizing the usual procedure of picking some random number between 1 and 0 and comparing it to the probability to find the system in each non-resonant well in the excited state after appropriate time interval (i.e. fluorescence lifetime). In the unlikely event that the random number is smaller than this (small) tunneling probability, this would be interpreted as discrete line jump. Further developments will include introduction of multi-dimensional and truly hierarchical energy landscapes.

References

[1] F. G. Parak, *“Physical aspects of protein dynamics,” Reports Prog. Phys.*, vol. 66, no. 2, pp. 103–129, Feb. 2003.

[2] K. Wüthrich, “Six years of protein structure determination by NMR spectroscopy: what have we learned?,” *Ciba Found. Symp.*, vol. 161, pp. 136–145; discussion 145–149, 1991.

[3] D. Thorn Leeson, D. A. Wiersma, K. Fritsch, and J. Friedrich, “The Energy Landscape of Myoglobin: An Optical Study,” *J. Phys. Chem. B*, vol. 101, no. 33, pp. 6331–6340, Aug. 1997.

[4] S. E. Dobbins, V. I. Lesk, and M. J. E. Sternberg, “Insights into protein flexibility: The relationship between normal modes and conformational change upon protein–protein docking,” *Proc. Natl. Acad. Sci.*, vol. 105, no. 30, pp. 10390–10395, Jul. 2008.

[5] Y. Berlin, A. Burin, J. Friedrich, and J. Köhler, “Spectroscopy of proteins at low temperature. Part I: Experiments with molecular ensembles,” *Phys. Life Rev.*, vol. 3, no. 4, pp. 262–292, Dec. 2006.

[6] H. Frauenfelder, S. G. Sligar, and P. G. Wolynes, “The energy landscapes and motions of proteins,” *Science*, vol. 254, no. 5038, pp. 1598–1603, Dec. 1991.

[7] Valter Zazubovich, “Optical Spectroscopy of Photosynthetic Pigment-Protein Complexes: Low-Temperature Protein Dynamics and Inter-Pigment Energy Transfer.” NSERC PIN:303884.

[8] J.-P. Galaup, “SPECTRAL SELECTIVE STUDIES OF MOLECULAR DOPED SOLIDS AND APPLICATIONS,” in *Advances In Multi-Photon Processes And Spectroscopy*, vol. 16, WORLD SCIENTIFIC, 2004, pp. 73–248.

[9] J. F. Allen and W. Martin, “Evolutionary biology: Out of thin air,” *Nature*, vol. 445, no. 7128, pp. 610–612, Feb. 2007.

[10] N. Nelson and A. Ben-Shem, “The complex architecture of oxygenic

photosynthesis," *Nat. Rev. Mol. Cell Biol.*, vol. 5, no. 12, pp. 971–982, Dec. 2004.

[11] J. W. MacAdam, *Structure and Function of Plants*. John Wiley & Sons, 2013.

[12] "PhotochemCAD Chemicals." [Online]. Available: http://omlc.ogi.edu/spectra/PhotochemCAD/index.html. [Accessed: 04-Jun-2013].

[13] Valter Zazubovich and Ryszard Jankowiak, "Biophotonics of Photosynthesis." [Online]. Available: http://scholar.googleusercontent.com/scholar?q=cache:B2LyEnT_R6EJ:scholar.google.com/&hl=en&as_sdt=0,5&sciodt=0,5. [Accessed: 05-Jun-2013].

[14] P. Fromme, Ed., *Photosynthetic Protein Complexes: A Structural Approach*. 2008.

[15] Lynn Yarris, "Research News: Berkeley Researchers Identify Photosynthetic Dimmer Switch." [Online]. Available: http://www.lbl.gov/Science-Articles/Archive/PBD-CP29.html. [Accessed: 13-May-2013].

[16] B. Loll, J. Kern, W. Saenger, A. Zouni, and J. Biesiadka, "Towards complete cofactor arrangement in the 3.0Å resolution structure of photosystem II," *Nature*, vol. 438, no. 7070, pp. 1040–1044, Dec. 2005.

[17] A. Zouni, "Crystal structure of photosystem II from Synechococcus elongatus at 3.8 A resolution," *Nature*, vol. 409, no. 6821, p. 739, Feb. 2001.

[18] R. Harrer, R. Bassi, M. G. Testi, and C. Schäfer, "Nearest-neighbor analysis of a Photosystem II complex from Marchantia polymorpha L. (liverwort), which contains reaction center and antenna proteins," *Eur. J. Biochem.*, vol. 255, no. 1, pp. 196–205, Jul. 1998.

[19] E. J. Boekema, H. van Roon, J. F. L. van Breemen, and J. P. Dekker, "Supramolecular organization of photosystem II and its light-harvesting antenna in partially solubilized photosystem II membranes," *Eur. J. Biochem.*, vol. 266, no. 2, p. 444, Dec. 1999.

[20] T. Wydrzynski and K. Satoh, Eds., *Photosystem II: The Light-Driven Water--Plastoquinone Oxidoreductase (Advances in Photosynthesis and Respiration)*, 2005th ed. Springer, 2005.

[21] “Photosystem II Introduction,” in *Photosynthesis Photobiochemistry and Photobiophysics (Advances in Photosynthesis and Respiration)*, Springer Netherlands, 2003, pp. 199–214.

[22] A. Pagano, G. Cinque, and R. Bassi, “In Vitro Reconstitution of the Recombinant Photosystem II Light-harvesting Complex CP24 and Its Spectroscopic Characterization,” *J. Biol. Chem.*, vol. 273, no. 27, pp. 17154–17165, Jul. 1998.

[23] H. van Amerongen, B. M. van Bolhuis, S. Betts, R. Mei, R. van Grondelle, C. F. Yocum, and J. P. Dekker, “Spectroscopic characterization of CP26, a chlorophyll ab binding protein of the higher plant Photosystem II complex,” *Biochim. Biophys. Acta BBA - Bioenerg.*, vol. 1188, no. 3, pp. 227–234, Dec. 1994.

[24] X. Pan, M. Li, T. Wan, L. Wang, C. Jia, Z. Hou, X. Zhao, J. Zhang, and W. Chang, “Structural insights into energy regulation of light-harvesting complex CP29 from spinach,” *Nat. Struct. Mol. Biol.*, vol. 18, no. 3, pp. 309–315, Mar. 2011.

[25] J. Pieper, K.-D. Irrgang, M. Rätsep, J. Voigt, G. Renger, and G. J. Small, “Assignment of the Lowest QY-state and Spectral Dynamics of the CP29 Chlorophyll a/b Antenna Complex of Green Plants: A Hole-burning Study ‡,” *Photochem. Photobiol.*, vol. 71, no. 5, pp. 574–581, 2000.

[26] C. Ilioaia, C. D. P. Duffy, M. P. Johnson, and A. V. Ruban, “Changes in the Energy Transfer Pathways within Photosystem II Antenna Induced by Xanthophyll Cycle Activity,” *J. Phys. Chem. B*, vol. 117, no. 19, pp. 5841–5847, May 2013.

[27] K. K. Rebane and L. A. Rebane, “Basic Principles and Methods of Persistent Spectral Hole-Burning,” in *Persistent Spectral Hole-Burning: Science and Applications*, D. W. E. Moerner, Ed. Springer Berlin Heidelberg, 1988, pp. 17–77.

[28] S. Adachi, *Optical Properties of Crystalline and Amorphous Semiconductors: Materials and Fundamental Principles*. Springer London, Limited, 2012.

[20] William W. Parson, “Electronic Absorption,” in *Modern Optical Spectroscopy*, Springer Berlin Heidelberg, 2007, pp. 109–188.

[30] N. W. Ashcroft and N. D. Mermin, *Solid State Physics*. Cengage Learning India

Private Limited, 2011.

[31] C. Kittel, *Introduction to solid state physics*. Wiley, 1971.

[32] P. W. Phillips, *Advanced Solid State Physics*. Westview Press, 2003.

[33] J. Friedrich, "[10] Hole burning spectroscopy and physics of proteins," in *Methods in Enzymology*, vol. Volume 246, Kenneth Sauer, Ed. Academic Press, 1995, pp. 226–259.

[34] K. K. Rebane and I. Rebane, "Peak value of the cross-section of zero-phonon line's absorption," *J. Lumin.*, vol. 56, no. 1–6, pp. 39–45, Oct. 1993.

[35] Valter Zazubovich, "Course Notes of Optical Spectroscopy," Concordia University, Montreal, Quebec, Canada, Fall-2009.

[36] T. Reinot and G. J. Small, "Modeling of dispersive nonphotochemical hole growth kinetics data: Al-phthalocyanine tetrasulphonate in hyperquenched glassy water," *J. Chem. Phys.*, vol. 113, no. 22, pp. 10207–10214, Dec. 2000.

[37] P. C. Whitford, "Disorder guides protein function," *Proc. Natl. Acad. Sci.*, vol. 110, no. 18, pp. 7114–7115, Apr. 2013.

[38] P. w. Anderson, B. I. Halperin, and c. M. Varma, "Anomalous low-temperature thermal properties of glasses and spin glasses," *Philos. Mag.*, vol. 25, no. 1, pp. 1–9, 1972.

[39] "Hole Burning Spectroscopy -Glass properties." [Online]. Available: http://www.isan.troitsk.ru/dms/les_lab/activity/holeburn/sd/intro.htm. [Accessed: 13-May-2013].

[40] T. Reinot, V. Zazubovich, J. M. Hayes, and G. J. Small, "New Insights on Persistent Nonphotochemical Hole Burning and Its Application to Photosynthetic Complexes," *J. Phys. Chem. B*, vol. 105, no. 22, pp. 5083–5098, Jun. 2001.

[41] C. Hofmann, T. J. Aartsma, H. Michel, and J. Kohler, "Direct observation of tiers in the energy landscape of a chromoprotein: A single-molecule study," *Proc. Natl. Acad. Sci. U. S. A.*, vol. 100, no. 26, pp. 15534–15538, Dec. 2003.

[42] M. Najafi, N. Herascu, M. Seibert, R. Picorel, R. Jankowiak, and V. Zazubovich,

"Spectral Hole Burning, Recovery, and Thermocycling in Chlorophyll–Protein Complexes: Distributions of Barriers on the Protein Energy Landscape," *J. Phys. Chem. B*, vol. 116, no. 38, pp. 11780–11790, Sep. 2012.

[43] W. E. Moerner, "Single-Molecule Optical Spectroscopy and Imaging: From Early Steps to Recent Advances," in *Single Molecule Spectroscopy in Chemistry, Physics and Biology*, A. Gräslund, R. Rigler, and J. Widengren, Eds. Springer Berlin Heidelberg, 2010, pp. 25–60.

[44] R. Jankowiak and G. J. Small, "Hole-Burning Spectroscopy and Relaxation Dynamics of Amorphous Solids at Low Temperatures," *Science*, vol. 237, no. 4815, pp. 618–625, Aug. 1987.

[45] J. M. Hayes and G. J. Small, "Photochemical hole burning and strong electron-phonon coupling: primary donor states of reaction centers of photosynthetic bacteria," *J. Phys. Chem.*, vol. 90, no. 21, pp. 4928–4931, Oct. 1986.

[46] J. M. Hayes, R. Jankowiak, and G. J. Small, "Two-Level-System Relaxation in Amorphous Solids as Probed by Nonphotochemical Hole-Burning in Electronic Transitions," in *Persistent Spectral Hole-Burning: Science and Applications*, D. W. E. Moerner, Ed. Springer Berlin Heidelberg, 1988, pp. 153–202.

[47] J. Jäckle, L. Piché, W. Arnold, and S. Hunklinger, "Elastic effects of structural relaxation in glasses at low temperatures," *J. Non-Cryst. Solids*, vol. 20, no. 3, pp. 365–391, May 1976.

[48] W. A. Phillips, *Amorphous solids: low-temperature properties*. Springer-Verlag, 1981.

[49] N. C. Dang, T. Reinot, M. Reppert, and R. Jankowiak, "Temperature Dependence of Hole Growth Kinetics in Aluminum−Phthalocyanine−Tetrasulfonate in Hyperquenched Glassy Water," *J. Phys. Chem. B*, vol. 111, no. 7, pp. 1582–1589, Feb. 2007.

[50] P. Reichert and R. Schilling, "Glasslike properties of a chain of particles with anharmonic and competing interactions," *Phys. Rev. B*, vol. 32, no. 9, pp. 5731–

5746, Nov. 1985.

[51] P. J. Price, “Attempt frequency in tunneling,” *Am. J. Phys.*, vol. 66, no. 12, p. 1119, 1998.

[52] P. Esquinazi, *Tunneling Systems in Amorphous and Crystalline Solids*. Springer, 1998.

[53] N. Herascu, S. Ahmouda, R. Picorel, M. Seibert, R. Jankowiak, and V. Zazubovich, “Effects of the Distributions of Energy or Charge Transfer Rates on Spectral Hole Burning in Pigment–Protein Complexes at Low Temperatures,” *J. Phys. Chem. B*, vol. 115, no. 50, pp. 15098–15109, Dec. 2011.

[54] R. Jankowiak, R. Richert, and H. Baessler, “Nonexponential hole burning kinetics in organic glasses,” *J. Phys. Chem.*, vol. 89, no. 21, pp. 4569–4574, Oct. 1985.

[55] R. Jankowiak, L. Shu, M. J. Kenney, and G. J. Small, “Dispersive kinetic processes, optical linewidths and dephasing in amorphous solids,” *J. Lumin.*, vol. 36, no. 4–5, pp. 293–305, Jan. 1987.

[56] S. P. Love and A. J. Sievers, “Persistent infrared spectral hole burning of the sulfur —hydrogen vibrational mode in hydrogenated As2S3 glass,” *Chem. Phys. Lett.*, vol. 153, no. 5, pp. 379–384, Dec. 1988.

[57] R. Jankowiak, J. M. Hayes, and G. J. Small, “Spectral hole-burning spectroscopy in amorphous molecular solids and proteins,” *Chem. Rev.*, vol. 93, no. 4, pp. 1471–1502, Jun. 1993.

[58] R. Jankowiak and G. J. Small, “Disorder-Induced Relaxation Processes in Amorphous Solids at Low Temperatures,” in *Disorder Effects on Relaxational Processes*, D. R. Richert and P. D. A. Blumen, Eds. Springer Berlin Heidelberg, 1994, pp. 425–448.

[59] W. Köhler and J. Friedrich, “Distribution of barrier heights in amorphous organic materials,” *Phys. Rev. Lett.*, vol. 59, no. 19, pp. 2199–2202, Nov. 1987.

[60] W. Köhler, J. Zollfrank, and J. Friedrich, “Thermal irreversibility in optically labeled low-temperature glasses,” *Phys. Rev. B*, vol. 39, no. 8, pp. 5414–5424, Mar.

1989.

[61] R. J. Silbey, J. M. A. Koedijk, and S. Völker, "Time and temperature dependence of optical linewidths in glasses at low temperature: Spectral diffusion," *J. Chem. Phys.*, vol. 105, no. 3, p. 901, Jul. 1996.

[62] B. Sauter and C. Bräuchle, "Structural relaxation in dye-surface systems: spectral diffusion and thermal recovery of spectral holes burnt into chemi- and physisorbed dye molecules," *J. Lumin.*, vol. 56, no. 1–6, pp. 117–124, Oct. 1993.

[63] S. P. Love, C. E. Mungan, A. J. Sievers, and J. A. Campbell, "Persistent infrared spectral hole burning of Tb3+ in the glasslike mixed crystal Ba1?X? YLaxTbyF2+x+y," *J. Opt. Soc. Am. B*, vol. 9, no. 5, pp. 794–799, May 1992.

[64] R. Purchase and S. Völker, "Spectral hole burning: examples from photosynthesis," *Photosynth. Res.*, vol. 101, no. 2–3, pp. 245–266, Sep. 2009.

[65] J. Zollfrank, J. Friedrich, J. M. Vanderkooi, and J. Fidy, "Conformational relaxation of a low-temperature protein as probed by photochemical hole burning. Horseradish peroxidase," *Biophys. J.*, vol. 59, no. 2, pp. 305–312, Feb. 1991.

[66] J. Eccles and B. Honig, "Charged amino acids as spectroscopic determinants for chlorophyll in vivo," *Proc. Natl. Acad. Sci.*, vol. 80, no. 16, pp. 4959–4962, Aug. 1983.

[67] T. Morosinotto, J. Breton, R. Bassi, and R. Croce, "The Nature of a Chlorophyll Ligand in Lhca Proteins Determines the Far Red Fluorescence Emission Typical of Photosystem I," *J. Biol. Chem.*, vol. 278, no. 49, pp. 49223–49229, Dec. 2003.

[68] J. Adolphs and T. Renger, "How Proteins Trigger Excitation Energy Transfer in the FMO Complex of Green Sulfur Bacteria," *Biophys. J.*, vol. 91, no. 8, pp. 2778–2797, Oct. 2006.

[69] A. Damjanović, H. M. Vaswani, P. Fromme, and G. R. Fleming, "Chlorophyll Excitations in Photosystem I of Synechococcus elongatus," *J. Phys. Chem. B*, vol. 106, no. 39, pp. 10251–10262, Oct. 2002.

[70] N. C. Dang, V. Zazubovich, M. Reppert, B. Neupane, R. Picorel, M. Seibert, and R.

Jankowiak, “The CP43 Proximal Antenna Complex of Higher Plant Photosystem II Revisited: Modeling and Hole Burning Study. I,” *J. Phys. Chem. B*, vol. 112, no. 32, pp. 9921–9933, Aug. 2008.

[71] M. Reppert, V. Zazubovich, N. C. Dang, M. Seibert, and R. Jankowiak, “Low-Energy Chlorophyll States in the CP43 Antenna Protein Complex: Simulation of Various Optical Spectra. II,” *J. Phys. Chem. B*, vol. 112, no. 32, pp. 9934–9947, Aug. 2008.

[72] J. L. Hughes, R. Picorel, M. Seibert, and E. Krausz, “Photophysical Behavior and Assignment of the Low-Energy Chlorophyll States in the CP43 Proximal Antenna Protein of Higher Plant Photosystem II†,” *Biochemistry (Mosc.)*, vol. 45, no. 40, pp. 12345–12357, Oct. 2006.

[73] M. Brecht, V. Radics, J. B. Nieder, and R. Bittl, “Protein dynamics-induced variation of excitation energy transfer pathways,” *Proc. Natl. Acad. Sci.*, vol. 106, no. 29, pp. 11857–11861, Jul. 2009.

[74] T. Reinot, N. . Dang, and G. . Small, “Non-photochemical versus photochemical hole burning in hyperquenched glassy water and cubic ice,” *J. Lumin.*, vol. 98, no. 1–4, pp. 183–188, Jul. 2002.

[75] T. Reinot and G. J. Small, “Non-Lorentzian zero-phonon holes and new insights on nonphotochemical hole burning: Al-phthalocyanine in hyperquenched glassy water,” *J. Chem. Phys.*, vol. 114, no. 20, pp. 9105–9114, May 2001.

[76] T. Reinot, N. C. Dang, and G. J. Small, “A model for persistent hole burned spectra and hole growth kinetics that includes photoproduct absorption: Application to free base phthalocyanine in hyperquenched glassy ortho-dichlorobenzene at 5 K,” *J. Chem. Phys.*, vol. 119, no. 19, pp. 10404–10414, Nov. 2003.

[77] D. Grozdanov, N. Herascu, T. Reinot, R. Jankowiak, and V. Zazubovich, “Low-Temperature Protein Dynamics of the B800 Molecules in the LH2 Light-Harvesting Complex: Spectral Hole Burning Study and Comparison with Single Photosynthetic Complex Spectroscopy,” *J. Phys. Chem. B*, vol. 114, no. 10, pp. 3426–3438, Mar.

2010.

[78] N. Herascu, M. Najafi, A. Amunts, J. Pieper, K.-D. Irrgang, R. Picorel, M. Seibert, and V. Zazubovich, "Parameters of the Protein Energy Landscapes of Several Light-Harvesting Complexes Probed via Spectral Hole Growth Kinetics Measurements," *J. Phys. Chem. B*, vol. 115, no. 12, pp. 2737–2747, Mar. 2011.

[79] W. Köhler, J. Friedrich, and H. Scheer, "Conformational barriers in low-temperature proteins and glasses," *Phys. Rev.*, vol. 37, no. 2, pp. 660–662, Jan. 1988.

[80] W. A. Phillips, "Tunneling states in amorphous solids," *J. Low Temp. Phys.*, vol. 7, no. 3–4, pp. 351–360, May 1972.

[81] J. Baier, M. F. Richter, R. J. Cogdell, S. Oellerich, and J. Köhler, "Do Proteins at Low Temperature Behave as Glasses? A Single-Molecule Study," *J. Phys. Chem. B*, vol. 111, no. 5, pp. 1135–1138, Feb. 2007.

[82] R. Jankowiak, G. J. Small, and K. B. Athreya, "Derivation of the density of states and distribution functions for two-level systems in glasses," *J. Phys. Chem.*, vol. 90, no. 17, pp. 3896–3898, Aug. 1986.

[83] J. Baier, M. F. Richter, R. J. Cogdell, S. Oellerich, and J. Köhler, "Determination of the Spectral Diffusion Kernel of a Protein by Single-Molecule Spectroscopy," *Phys. Rev. Lett.*, vol. 100, no. 1, p. 018108, Jan. 2008.

[84] R. van Grondelle, R. Monshouwer, and L. Valkunas, "Photosynthetic antennae. Photosynthetic light-harvesting," *Berichte Bunsenges. Für Phys. Chem.*, vol. 100, no. 12, pp. 1950–1957, 1996.

[85] R. J. Cogdell and J. G. Lindsay, "Tansley Review No. 109. The Structure of Photosynthetic Complexes in Bacteria and Plants: An Illustration of the Importance of Protein Structure to the Future Development of Plant Science," *New Phytol.*, vol. 145, no. 2, pp. 167–196, Feb. 2000.

[86] T. Basché and W. E. Moerner, "Optical modification of a single impurity molecule in a solid," *Nature*, vol. 355, no. 6358, pp. 335–337, Jan. 1992.

[87] P. Tchénio, A. B. Myers, and W. E. Moerner, "Optical studies of single terrylene

molecules in polyethylene," *J. Lumin.*, vol. 56, no. 1–6, pp. 1–14, Oct. 1993.

[88] F. Kulzer, S. Kummer, R. Matzke, C. Bräuchle, and T. Basche´, "Single-molecule optical switching of terrylene in p-terphenyl," *Nature*, vol. 387, no. 6634, pp. 688–691, Jun. 1997.

[89] L. Fleury, A. Zumbusch, M. Orrit, R. Brown, and J. Bernard, "Spectral diffusion and individual two-level systems probed by fluorescence of single terrylene molecules in a polyethylene matrix," *J. Lumin.*, vol. 56, no. 1–6, pp. 15–28, Oct. 1993.

[90] W. E. Moerner, T. Plakhotnik, T. Irngartinger, M. Croci, V. Palm, and U. P. Wild, "Optical Probing of Single Molecules of Terrylene in a Shpol'kii Matrix: A Two-State Single-Molecule Switch," *J. Phys. Chem.*, vol. 98, no. 30, pp. 7382–7389, Jul. 1994.

[91] M. Hussels and M. Brecht, "Effect of Glycerol and PVA on the Conformation of Photosystem I," *Biochemistry (Mosc.)*, vol. 50, no. 18, pp. 3628–3637, May 2011.

[92] H. Oikawa, S. Fujiyoshi, T. Dewa, M. Nango, and M. Matsushita, "How Deep Is the Potential Well Confining a Protein in a Specific Conformation? A Single-Molecule Study on Temperature Dependence of Conformational Change between 5 and 18 K," *J. Am. Chem. Soc.*, vol. 130, no. 14, pp. 4580–4581, Apr. 2008.

[93] J. Pieper, M. Rätsep, R. Jankowiak, K.-D. Irrgang, J. Voigt, G. Renger, and G. J. Small, "Qy-Level Structure and Dynamics of Solubilized Light-Harvesting Complex II of Green Plants: Pressure and Hole Burning Studies," *J. Phys. Chem. A*, vol. 103, no. 14, pp. 2412–2421, Apr. 1999.

[94] R. Jankowiak, V. Zazubovich, M. Rätsep, S. Matsuzaki, M. Alfonso, R. Picorel, M. Seibert, and G. J. Small, "The CP43 Core Antenna Complex of Photosystem II Possesses Two Quasi-Degenerate and Weakly Coupled Qy-Trap States," *J. Phys. Chem. B*, vol. 104, no. 49, pp. 11805–11815, Dec. 2000.

[95] T. Reinot, J. M. Hayes, and G. J. Small, "Laser-induced hole filling and spectral diffusion of aluminum phthalocyanine tetrasulfonate in hyperquenched glassy

films," *J. Chem. Phys.*, vol. 110, no. 10, pp. 4820–4827, Mar. 1999.

[96] J. Baier, M. Gabrielsen, S. Oellerich, H. Michel, M. van Heel, R. J. Cogdell, and J. Köhler, "Spectral Diffusion and Electron-Phonon Coupling of the B800 BChl a Molecules in LH2 Complexes from Three Different Species of Purple Bacteria," *Biophys. J.*, vol. 97, no. 9, pp. 2604–2612, Nov. 2009.

[97] P. W. Fenimore, H. Frauenfelder, B. H. McMahon, and R. D. Young, "Proteins are paradigms of stochastic complexity," *Phys. Stat. Mech. Its Appl.*, vol. 351, no. 1, pp. 1–13, Jun. 2005.

[98] F. Jelezko, C. Tietz, U. Gerken, E. Thews, S. Schuler, A. Wechsler, and J. Wrachtrup, "Single Molecule Spectroscopy on Photosynthetic Pigment-Protein Complexes," *Opt. Spectrosc.*, vol. 91, no. 3, p. 457, Sep. 2001.

[99] C. Tietz, F. Jelezko, U. Gerken, S. Schuler, A. Schubert, H. Rogl, and J. Wrachtrup, "Single Molecule Spectroscopy on the Light-Harvesting Complex II of Higher Plants," *Biophys. J.*, vol. 81, no. 1, pp. 556–562, Jul. 2001.

[100] M. L. Groot, R. N. Frese, F. L. de Weerd, K. Bromek, A. Pettersson, E. J. Peterman, I. H. van Stokkum, R. van Grondelle, and J. P. Dekker, "Spectroscopic properties of the CP43 core antenna protein of photosystem II.," *Biophys. J.*, vol. 77, no. 6, pp. 3328–3340, Dec. 1999.

[101] X. Feng, A. Kell, J. Pieper, and R. Jankowiak, "Modeling of Optical Spectra of the Light-Harvesting CP29 Antenna Complex of Photosystem II—Part II," *J. Phys. Chem. B*, vol. 117, no. 22, pp. 6593–6602, Jun. 2013.

[102] J. L. Hughes, B. J. Prince, S. P. Årsköld, E. Krausz, R. J. Pace, R. Picorel, and M. Seibert, "Photo-conversion of chlorophylls in higher-plant CP43 characterized by persistent spectral hole burning at 1.7 K," *J. Lumin.*, vol. 108, no. 1–4, pp. 131–136, Jun. 2004.

[103] L. Shu and G. J. Small, "Mechanism of nonphotochemical hole burning: Cresyl Violet in polyvinyl alcohol films," *J. Opt. Soc. Am. B*, vol. 9, no. 5, pp. 724–732, May 1992.

[104] W. Köhler and J. Friedrich, “Probing of conformational relaxation processes of proteins by frequency labeling of optical states,” *J. Chem. Phys.*, vol. 90, no. 2, pp. 1270–1273, Jan. 1989.

[105] U. Bogner and R. Schwarz, “Laser-induced changes in the sideband shape of selectively excited dyes in noncrystalline organic solids at 1.3 K,” *Phys. Rev. B*, vol. 24, no. 5, pp. 2846–2849, Sep. 1981.

[106] R. Kiyanagi, H. Kimura, M. Watanabe, Y. Noda, T. Mochida, and T. Sugawara, “Indication of Tunneling State of Hydrogen Atom in Hydrogen-Bonded Material 5-Bromo-9-hydroxyphenalenon Studied by X-ray and Neutron Diffractions,” *J. Phys. Soc. Jpn.*, vol. 77, no. 6, p. 064602, 2008.

[107] W. C. Hamilton, *Hydrogen bonding in solids; methods of molecular structure determination*. New York: W. A. Benjamin, 1968.

[108] C. von Borczyskowski, A. Oppenländer, H. P. Trommsdorff, and J.-C. Vial, “Optical measurements of methyl-group tunneling and nuclear-spin conversion,” *Phys. Rev. Lett.*, vol. 65, no. 26, pp. 3277–3280, Dec. 1990.

[109] M. Pinsker and J. Friedrich, “Methyl group rotational tunneling splittings and spin conversion dynamics: p-chlorotoluene in cyclohexane,” *J. Chem. Phys.*, vol. 117, no. 10, pp. 4639–4642, Sep. 2002.

[110] M. M. Somoza and J. Friedrich, “The physics of rotational tunneling: hole-burning spectroscopy of methyl groups,” *Low Temp. Phys.*, vol. 32, no. 11, pp. 1020–1027, Nov. 2006.

[111] E. Barkai, A. V. Naumov, Y. G. Vainer, M. Bauer, and L. Kador, “Lévy Statistics for Random Single-Molecule Line Shapes in a Glass,” *Phys. Rev. Lett.*, vol. 91, no. 7, p. 075502, Aug. 2003.

[112] A. V. Naumov, Y. G. Vainer, and L. Kador, “Does the Standard Model of Low-Temperature Glass Dynamics Describe a Real Glass?,” *Phys. Rev. Lett.*, vol. 98, no. 14, p. 145501, Apr. 2007.

[113] A. Heuer and P. Neu, “Tunneling dynamics of side chains and defects in proteins,

polymer glasses, and OH-doped network glasses," *J. Chem. Phys.*, vol. 107, no. 20, pp. 8686–8696, Nov. 1997.

[114] F. T. H. den Hartog, C. van Papendrecht, U. Störkel, and S. Völker, "Protein Dynamics in Photosystem II Complexes of Green Plants Studied by Time-Resolved Hole-Burning," *J. Phys. Chem. B*, vol. 103, no. 8, pp. 1375–1380, Feb. 1999.

[115] M. Brecht, H. Studier, V. Radics, J. B. Nieder, and R. Bittl, "Spectral Diffusion Induced by Proton Dynamics in Pigment−Protein Complexes," *J. Am. Chem. Soc.*, vol. 130, no. 51, pp. 17487–17493, Dec. 2008.

[116] L. R. Narasimhan, K. A. Littau, D. W. Pack, Y. S. Bai, A. Elschner, and M. D. Fayer, "Probing organic glasses at low temperature with variable time scale optical dephasing measurements," *Chem. Rev.*, vol. 90, no. 3, pp. 439–457, May 1990.

[117] S. Mukamel, *Principles of Nonlinear Optical Spectroscopy*. Oxford University Press, 1999.

[118] J. M. A. Koedijk, R. Wannemacher, R. J. Silbey, and S. Völker, "Spectral Diffusion in Organic Glasses: Time Dependence of Spectral Holes," *J. Phys. Chem.*, vol. 100, no. 51, pp. 19945–19953, Jan. 1996.

[119] K. A. Littau and M. D. Fayer, "Probing low temperature glass dynamics by fast generation and detection of optical holes," *Chem. Phys. Lett.*, vol. 176, no. 6, pp. 551–558, Feb. 1991.

[120] R. Jankowiak and G. J. Small, "Spectral diffusion of molecular electronic transitions in amorphous solids: Weak and strong two-level-system phonon coupling," *Phys. Rev. B*, vol. 47, no. 22, pp. 14805–14812, Jun. 1993.

[121] H. C. Meijers and D. A. Wiersma, "Glass dynamics probed by the long-lived stimulated photon echo," *Phys. Rev. Lett.*, vol. 68, no. 3, pp. 381–384, Jan. 1992.

[122] M. J. Kenney, R. Jankowiak, and G. J. Small, "Dispersive kinetics of nonphotochemical hole growth for oxazine 720 in glycerol, polyvinyl alcohol and their deuterated analogues," *Chem. Phys.*, vol. 146, no. 1–2, pp. 47–61, Sep. 1990.

[123] M. B. Jackson, *Molecular And Cellular Biophysics*. Cambridge University Press,

2006.

[124] “gnu.org.” [Online]. Available: http://www.gnu.org/software/gsl/. [Accessed: 14-Jul-2013].

[125] J. R. Lakowicz, *Principles of Fluorescence Spectroscopy*. Springer, 2006.